MG-BASED NANO-LAYERED THIN FILMS FOR HYDROGEN STORAGE

A Dissertation

by

ANCHALEE JUNKAEW

Submitted to the Office of Graduate and Professional Studies of
Texas A&M University
in partial fulfillment of the requirements for the degree of

DOCTOR OF PHILOSOPHY

Chair of Committee,	Raymundo Arróyave
Committee Members,	Xinghang Zhang
	Perla B. Balbuena
	Choongho Yu
Head of Department,	Ibrahim Karaman

December 2013

Major Subject: Materials Science and Engineering

ABSTRACT

Magnesium (Mg) based materials are now some of the most promising materials for hydrogen storage due to their light weight and high hydrogen capacity. Their most significant limitation, however, is the high de-hydrogenation temperature and low kinetics. Niobium (Nb) has been proposed for improving the hydrogen sorption kinetics in Mg thin films. In this work, Mg/Nb multi-layered thin films were investigated by theoretical methods and compared to experimental results. Some selected properties such as structural, elastic, energetic and electronic charge properties of the bulk and thin films have been investigated.

Firstly, classical thermodynamic models and first-principles calculations based on Density Functional Theory (DFT) were used for describing the pseudomorphic growth in Mg/Nb multi-layered films observed in experiments. Calculations of the thermodynamic, electronic and structural stability of a body-centered cubic (bcc) Mg show that this structure is in fact metastable under thin film conditions, when Mg grows epitaxially on the bcc Nb, in agreement with experiments. The predicted bi-phase diagram of Mg/Nb multilayers indicated that not only the metastable bcc Mg can be stabilized, but also a hexagonal close packed (hcp) Nb can be stabilized under the specific range of the bilayer thickness and the volume fractions of the constituents.

Next, the hydrogen desorption properties of the free standing Mg films and Mg/Nb multilayers were elucidated by DFT calculations. The computational tools were used for assisting the experimental characterization. As a result, two metastable orthorhombic magnesium hydrides (O_s-MgH_2 and O_m-MgH_2) were observed in those films. Due to the influence of stress and corresponding formation of these metastable

phases, significant destabilization of MgH_2 provides ultra-low hydrogen desorption temperature in both free-standing Mg and multilayer Mg/Nb films. Formation of enthalpies (ΔH_f) and estimating desorption temperatures (T_d) were determined by DFT calculations and indicated that either tension or compression will lead to destabilization of MgH_2. Moreover the hydrogen diffusion mechanisms were studied in both bulk and thin film structures. The site preference and diffusion activation energy calculations successfully describe hydrogen sorption behavior in Mg/Nb multilayers in experiments.

It is expected that the results of this research will foster further work on the development of the solid-state hydrogen storage systems necessary to bring the hydrogen economy closer to reality.

DEDICATION

This dissertation is dedicated to my family, Doungkham Junkaew, Noi Junkaew and Sawas Junkaew, for their love and faith.

ACKNOWLEDGEMENTS

First of all, I would like to express my very great appreciation to my advisor, Dr. Raymundo Arróyave, for his advice, support and encouragement during the development of this research. Not only his suggestion on this research, Dr. Arróyave also gave me great opportunities to participate in many conferences and workshops. Those events provided me the great chance to ignite the new idea from experts and participants with diverse professional backgrounds. Additionally, I am also grateful to Byoungsoo Ham and Dr. Xinghang Zhang for the excellent experimental work. The goals of this research were achieved from the strong collaboration of experimental and computational contributions. My special thanks are extended to my committee members, Prof. Perla B. Balbuena and Dr. Choongho Yu, for their time in serving on my committee.

I would also like to extend my thanks to my funding resources. This research was supported by the National Science Foundation under NSF Grant No. CBET-0932249 and partial support from the NSF Grant No. CMMI-0953984. I also wish to acknowledge the Royal Thai Government and the National Nanotechnology Center (NANOTEC) in Thailand for providing me a full scholarship for pursuing my Ph.D. degree. Moreover, I would like to thank the computing centers. Most of the calculations were carried out on the CAT cluster of the department of Chemical Engineering of Texas AM University and the HYDRA and EOS clusters of Texas A&M Supercomputing facility. High-Performance Computing facilities from the Texas Advanced Computing Center in the University of Texas at Austin, which are the RANGER and LONESTAR clusters, were also used.

Furthermore, I wish to thank the former and current students in Dr. Arroyave's

group for their friendship and helpful discussions. Also, I extend my appreciation to my Thai friends in College Station for their friendship and encouragement. Definitely, I would like to express my deepest gratitude to my father, my mother and my brother for their unconditional love and endless support. Finally, my grateful thanks are also extended to my best friend for his encouragement and assistance in keeping me to get through my hard time completing my study.

NOMENCLATURE

BZ	Brillouin Zone
CALPHAD	CALculation of PHAse Diagram
CI-NEB	the Climbing Image Nudged Elastic Band
DFT	Density Functional Theory
DOE	the US Department of Energy
DOS	Density of State
ELF	Electron Localization Function
FFT	the Fast–Fourier Transform
IUPAC	International Union of Pure and Applied Chemistry
MEP	the Minimum Energy Path
ML	Monolayer
MC	Monte Carlo
MD	Molecular Dynamics
P	Pressure
PCI	the Pressure–Composition Isotherm
PCT	the Pressure–Composition Temperature
SGTE	Scientific Group Thermodata Europe
SSA	Specific surface area
T	Temperature
VASP	Vienna *abinitio* simulation package
ZPE	Zero point energy

TABLE OF CONTENTS

LIST OF FIGURES

FIGURE Page

LIST OF TABLES

TABLE Page

1. INTRODUCTION AND LITERATURE REVIEW

1.1 Hydrogen technology and applications

The so-called hydrogen economy is based on the use of clean, renewable hydrogen-based energy generation systems. In this technology, hydrogen gas (H_2) is not a primary energy source, but rather it is an energy carrier [1]. Fig. 1.1 shows a simple schematic of the *ideal* hydrogen cycle [2]: First, hydrogen is generated from electrolysis of water, with the energy necessary for this reaction coming from other energy sources. Once hydrogen and oxygen are separated, the former can be stored (in gas tanks or in solid-state storage systems). The store hydrogen can then be recombined with hydrogen in a fuel cell—essentially reversing the electrolysis reaction—generating electricity with water being a byproduct of the reaction. The percentage present in Fig. 1.1 is the approximated conversion efficiency of each step. This hydrogen cycle is similar to the carbon cycle. However, in this case hydrogen can be considered to be an ideal clean fuel, as the combustion reaction of hydrogen with oxygen produces water vapor without emitting toxic or greenhouse gases, such as carbon monoxide (CO) or carbon dioxide (CO_2). Moreover, the chemical energy per mass of hydrogen is greater than that of other chemical fuels. In fact, the energy content of hydrogen is three times larger than that of liquid hydrocarbons of the same mass [3].

Hydrogen-based energy generation and storage is a promising technology that could in principle at least partly alleviate some of the considerable environmental problems we currently phase. However, there are many challenges that need to be resolved in order to further develop this technology. For instance, the hydrogen production, hydrogen storage as well as combustion processes are required to be

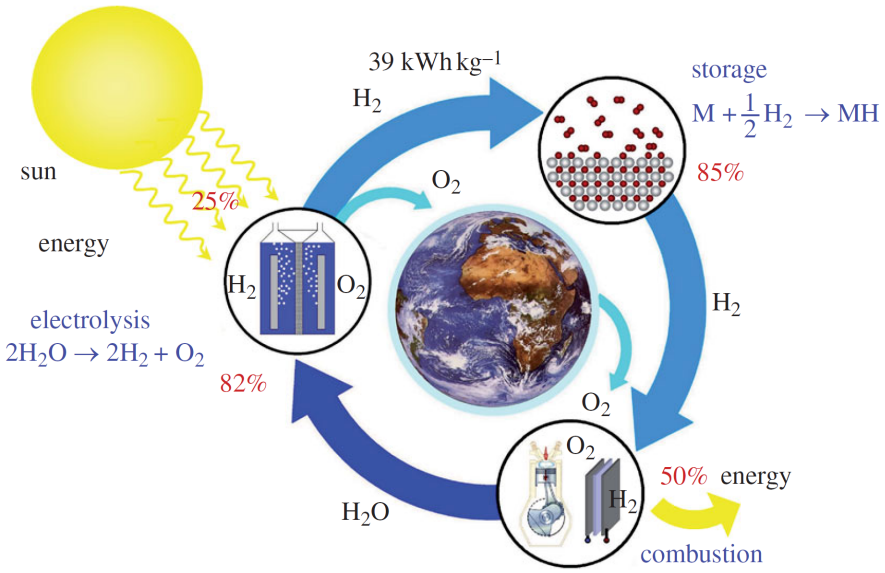

Figure 1.1: The ideal Hydrogen cycle [2]

convenient, efficient, safe and economical.

1.1.1 Hydrogen production

Hydrogen can in principle be obtained from different processes but one of the most effective approaches is through reforming of natural gas, which is produced from other fossil fuel sources or coal gasification. Unfortunately, these sources produce significant amounts of greenhouse (and other toxic) gases, negating the benefits—in terms of curtailing detrimental emissions—of hydrogen-based power generation. In the long term, the hydrogen economy cannot be realized unless renewable and sustainable sources are used for hydrogen production.

Many possible techniques have been proposed for producing hydrogen [1, 3]. The most widely used technique is electrolysis, which is a process that consists of the decomposition of water into hydrogen and oxygen using electricity. The reduction and the oxidation produce H_2 at cathode and O_2 at anode, respectively. Potential

energy sources of electrical power for electrolysis are solar power, nuclear power, hydro power, wind turbine, etc. Furthermore, hydrogen can be obtained from fermentation of biomass by using bacteria or high temperature. Another technique is based on thermochemical approaches. This technique splits water molecules by applying very high temperature. The difficulties associated with this latter approach are thermal management, heat extraction, and improvement of high temperature materials used. In addition, this method requires multistep thermochemical processes. In 2013, Munich *et al.* have developed the so-called isothermal water splitting (ITWS) technique. This technique is based on the solar thermal water-splitting (STWS), which generates hydrogen from water and sunlight [4]. Sunlight is concentrated into a tower and heat is delivered into a reactor containing a metal oxide compound. Normally, two steps of reduction and oxidation (redox) are involved in production of H_2. The ITWS technique developed by Munich and collaborators complete the two reactions at single temperature ($\sim$1350^{o}C), instead of two different temperatures for two reactions used in traditional techniques. This latter aspect increases the overall efficiency of the hydrogen production cycle. All in all, there are many more technologies for the clean production of hydrogen, and it is very likely that this progress will continue as it has for the past decades.

1.1.2 Hydrogen storage

While there are still many challenges associated to the clean and efficient production of hydrogen, one of the most critical problems that prevent a wider deployment of the so-called hydrogen economy is the lack of feasible solution for the storage of hydrogen once it has been produced. At ambient conditions, hydrogen is a gas which is non-toxic. Its combustion with oxygen produces energy and water. Although its combustion with nitrogen will produce nitric oxide, which is an air pollutant, this

product can be controllable [5]. A high volumetric density (ρ_v), which is an amount of hydrogen stored per unit volume of a material, and a high gravimetric density (ρ_m), which is an amount of hydrogen stored per mass of a material, are required for a hydrogen storage. Because hydrogen is colorless and odorless, it is difficult to detect a leakage. Therefore, not only an efficiency issue but a safety issue must be considered in practical applications. Typically, hydrogen may be stored as a pressurized gas, a cryogenic liquid, or a solid form. Hydrogen has very low density (0.089886 kg/m^3 at 0^{o}C and 1 bar) in the gaseous state. The high-pressure storage can be used for compressing volume and storing hydrogen in a gas phase. This method is restricted by the weight of the storage tank and the potential of a leakage causing safety concerns. At the present, a maximum pressure of 20 MPa is retained in a traditional high-pressure gas cylinders. The wall of a gas cylinder is capped with two hemispheres shown in Fig. 1.2. The relationship of the ratio of the wall thickness d_w to the outer diameter (d_o) of the cylinder, the overpressure ($\Delta\rho$) and the tensile strength of the material (σ_v) is given as the following equation:

$$\frac{d_w}{d_o} = \frac{\Delta p}{2\sigma_v + \Delta p} \tag{1.1}$$

Thus, the capability of storing gas at a given pressure depends on the tensile strength of the material and the thickness of a cylinder. Recently, high pressure (80 MPa) hydrogen storage has been achieved in new lightweight composite cylinders [2]. In contrast of a volumetric density, a gravimetric density decreases, when pressure is increased. Both volumetric- and gravimetric-densities need to be satisfied to get a suitable storage solution. Nowadays, a 110 kg and 70 MPa vessel, which has a gravimetric density of 6 mass% and a volumetric density of 30 kg/m^3, is a target for industry [1]. Important safety issues that pressurized cylinders need to comply

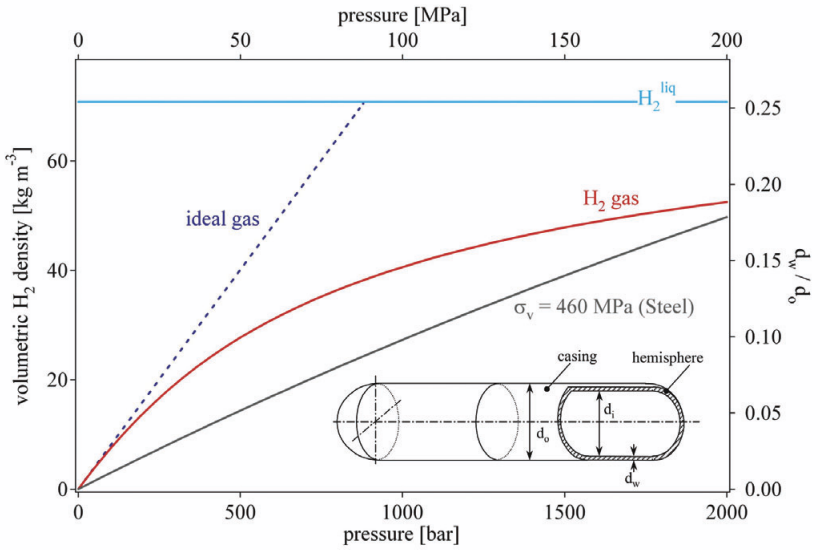

Figure 1.2: Comparison of volumetric density as a function of gas pressure of H_2 gas (a red line), ideal gas (a blue dashed line) and liquid hydrogen (H_2^{liq}, a light blue line). The d_w/d_o values of steel with a tensile strength of 460 MPa (labelled on the right vertical axis) as a function of gas pressure are represent as a black line. [7]

with are: temperature increase during high rate gas cylinder filling, hydrogen embrittlement of metals at ambient temperatures, etc. [6]. A three layered vessel, which consists of a polymer inner layer, a middle carbon-fiber composite (the stress-bearing component) layer and an outer layer constructed from an aramid-based material (for preventing mechanical and corrosion damage), has been proposed as feasible high-pressure hydrogen storage solution [1]. Unfortunately, the problems that need to be overcome are quite complex and it is very likely that they will remain unanswered over the foreseeable future.

In case of liquid hydrogen (LH_2) tanks, a refrigeration and super-insulated low temperature storage units are required, due to hydrogen's low boiling point (-252 ^{o}C) at 1 bar [8]. On the other hand, a high pressure of 104 bar must be applied to keep hydrogen as a liquid form at room temperature. A liquefaction process is

used for cooling hydrogen from room temperature to its boiling point. This process consumes large amounts of energy and is thus a highly inefficient method for the storage of a clean energy carrier. Another limitation of this approach is the fact that the storage vessel needs to be very well insulated in order to keep hydrogen in the liquid state [2].

Another method for hydrogen storage is to use solid-state approaches. One of the main advantages of this method over the two conventional methods discussed above is a significant enhancement in the volumetric hydrogen-storage capacity—hydrogen is stored in specific surface or volume lattice sites of the structure and the resulting hydrogen-hydrogen interatomic spacing is orders of magnitude smaller than what would be expected if it were to be stored in the gas phase. In addition to the improvements in volumetric capacity, storing hydrogen in the solid state results in significant improvements in safety.

In this case, hydrogen may be adsorbed (or absorbed), interact with a host media and be released from the host media for usage. Materials-based storage can be characterized by the hydrogen sorption behavior (e.g. physisorption or chemisorption) or the class of storage materials (e.g. metal hydride, carbon-based materials, metal-organic frameworks (MOFs), etc.). Typical sorption mechanisms of hydrogen in materials-based storage are represented by simple schematics shown in Fig. 1.3. Fig. 1.3(a) illustrates physisorption (or physical adsorption) of hydrogen in high porosity materials. In this case, the hydrogen atoms and the host material do not have chemical interactions with each other. In contrast, Fig. 1.3(b) to 1.3(c) represent typical chemisorption processes. Firstly, H_2 chemically interacts at a surface of material shown in Fig. 1.3(b). Fig. 1.3(c) shows the splitting of the H_2 molecule on the material surface. After the dissociation of H_2 into molecular H, H forms chemical bonding (i.e. metallic, covalent or ionic bonds) with the host atoms, forming a new

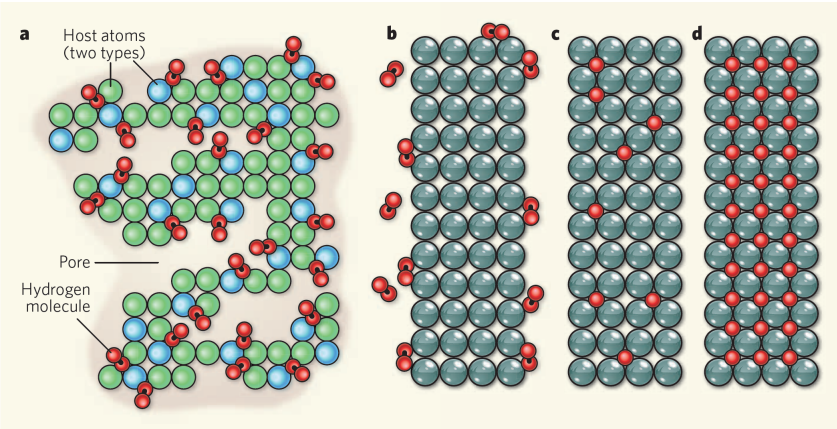

Figure 1.3: Mechanisms of storing hydrogen in solid materials (a) physisorption in a high porosity material, (b) chemisorption of H_2 on a surface of a material, (c) split H atoms have chemical interaction with host atoms, and (d) forming a hydride compound with periodic arrangement [5]

phase, as illustrated in Fig. 1.3(d).

In order for a material to be suitable for hydrogen storage applications, there are some criteria that must be met, such as large hydrogen capacity (>6 % wt.), good reversibility in the hydrogen sorption-desorption at relatively low temperatures, favorable thermodynamics, fast kinetics (required for high hydrogen sorption rate), cyclic stability, high thermal conductivity and low cost [9]. In 2009, the US Department of Energy (DOE) proposed the revised targets for hydrogen storage in light-duty vehicles shown in Table 1.1 [10]. Development of materials-based storage will be further discussed in the literature review section.

1.1.3 Hydrogen combustion: fuel cells

Fuel cells are electrochemical devices that essentially reverse the electrolysis process. H_2 and O_2 are recombined by electrochemical processes and the resulting electrons are then used to do useful work. A schematic of a typical fuel cell is shown in Fig. 1.4. H_2 is loaded to an anode, converted to protium (H_2^0), and then split into

Table 1.1: Selected hydrogen storage targets for light-duty vehicles proposed by DOE in 2009[10]

Target	2010	2015	Ultimate
Gravimetric density (%wt)	4.5	5.5	7.5
Volumetric density (g/L)	0.028	0.04	0.07
Min/max operating temperature (^{o}C)	-30/50	-40/60	-40/60
Fueling rate for 5kg H_2 (minute)	4.2	3.3	2.5

Note: 1 kg H_2 $\approx$1 gal gasoline equivalent

two protons (H^+) and two electron (e^-). At the anode (negative electrode), there is typically a Pt-based catalyst, which is used as hydrogen adsorbent that facilitates the dissociation between hydrogen diatomic molecule and molecular hydrogen. The electrons generated at the anode are then passed through an external circuit for generating a current, and they flow further to a cathode (positive electrode). Meanwhile, H^+ ions penetrate through a polymer electrolyte membrane to the cathode side. On another side of the cell, air is supplied for feeding O_2 to the cathode. A reaction of electrons, oxygen and protons form water as byproduct.

Many types of fuel cells have been developed, such as alkaline fuel cells (AFC), polymer electrolyte membrane fuel cells (PEMFC), direct methanol fuel cell (DMFC), phosphoric acid fuel cells (PAFC), molten carbonate fuel cells (MCFC) and solid-oxide fuel cell (SOFC) [1]. They are classified based on the electrolyte. The operating temperatures of those fuel cells increase in the following order: AFC (80 ^{o}C), PEMFC (<40 ^{o}C - 90 ^{o}C), DMFC(60 ^{o}C - 120 ^{o}C), PAFC (150 ^{o}C - 200 ^{o}C), MCFC (650 ^{o}C) and SOFC (>800 ^{o}C). Recently, polymer electrolyte membrane fuel cells (PEMFC) have emerged as the most appropriate type of fuel cells for hydrogen technologies due to their low operating temperature, high power density, quick startup and fast

response to load changes [11]. The most common electrolyte used in the cells is an organic polymer polyperfluorosulfonic acid (PFSA) electrolyte membrane. However, their catalysts are expensive and they are highly sensitive to fuel impurities. For other types of fuel cells, there are different pros and cons. For example, AFC consists of potassium hydroxide (KOH) as the electrolyte. The important advantages of this type of cell are its cheap component, high performance, low operating temperature. The major problem is that the electrolyte reacts with CO_2 and decrease the cell performance. Therefore, it is required to incorporate expensive CO_2 removal systems. SOFC employs ceramics materials (i.e. yttria-stabilised zirconia (YSZ)) as its electrolyte and electrodes. SOFC has high efficiency and a variety of catalysts can be used in this cell. However, its high operating temperature is the biggest drawback. The main challenge is developing of low cost materials with high durability at working temperatures [12]. Each fuel cell technology has its own advantages and disadvantages. Further development is required in this field.

1.1.4 Applications and outlook

In summary, hydrogen-based energy technologies are promising approaches towards clean, renewable, environmentally-benign energy. This technology has been proposed to be used in stationary, compact devices, mobile applications, etc. The three main aspects of hydrogen energy technologies—hydrogen production, hydrogen storage and hydrogen combustion—require the solution of significant technological challenges. For example, hydrogen production needs to be in large scale and ideally using sustainable and renewable energy resources. Hydrogen storage need to be efficient, safe and viable. Now, pressurized hydrogen tank have been used in laboratory applications. Cryogenic liquid hydrogen tank is suitable for applications with a short consuming time of gas, such as air and space applications [8, 7]. Solid-state storage

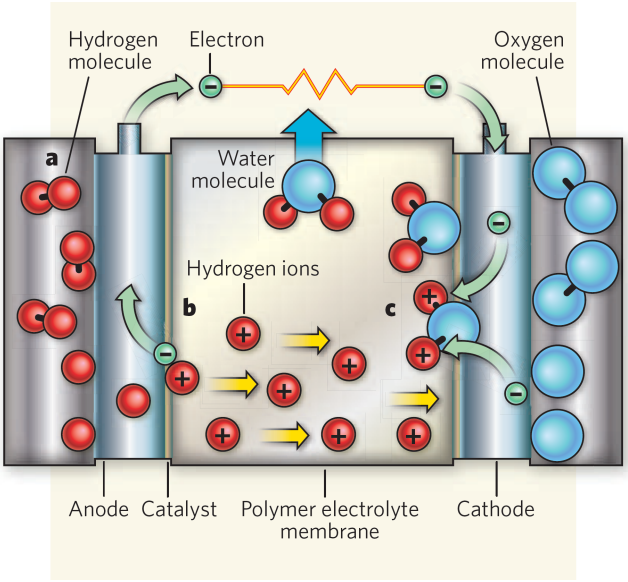

Figure 1.4: A schematic of hydrogen fuel cell: an example of the polymer electrolyte membrane fuel cells (PEMFC) [5]

systems constitute very attractive alternatives for hydrogen storage technologies due to their significant volumetric storage capacity as well as the significant improvements in safety that result from decreasing the need of using gas tank at very high pressures. Unfortunately, most of the materials that have been proposed as solid-state storage solutions have only been used at a laboratory scale. Moreover, while a lot of emphasis has been placed on improving the sorption/desoprtion characteristics of hydrogen storage, technical aspects such as the charging, discharging, charging cycle, operating conditions need to be signficantly improved. Additionally, other issues such as hydrogen delivery, refuelling station, price, etc. , need to be developed for mobile applications.

1.2 Literature review: development of materials-based hydrogen storage

For materials-based hydrogen storage, hydrogen can be stored in host materials by physisorption or chemisorption processes. This method greatly reduces storing

volume compared to the conventional methods. However a gravimetric density needs to be considered, because host materials are in some cases not very light. In this section, some important classes of materials-based hydrogen storage, which have been actively studied, are selected and reviewed.

1.2.1 Physisorption materials

The first type of materials-based hydrogen storages are physisorption materials (or adsorptive materials), which are high-surface area or porous materials. In this type of materials, molecular hydrogen (H_2) is adsorbed and adhered to a storage media by physisorption process. Van der Waal forces arise between hydrogen molecules and atoms on the surface of adsorbing materials (or adsorbents). Considering the van der Waals interaction, the energy between the sorbent and hydrogen molecule (E_{S-H_2}) relates to:

$$E_{S-H_2} \sim \frac{\alpha_{H_2}\alpha_S}{R^6} \tag{1.2}$$

where α_{H_2} and α_S is the polarizibilities of H_2 and the sorbent, respectively. R is the distance between H_2 and the sorbent. Because α_{H_2} is constant, increasing the polarizibility of the sorbent is the only method to enhance the interaction between sorbent and hydrogen[13]. Also, there are short range repulsive interactions. The Lennard-Jones equation is used to described a potential energy curve arisen by those attractive- and repulsive-interactions between H_2 and absorbent atoms. The potential energy changes as a function of a distance between H_2 and adsorbent atoms.

For porous materials, types of pores can be categorized by a size of dimension, that are micropores (<2 nm), mesopores (2 nm to 50 nm) and macropores (>50 nm), according the International Union of Pure and Applied Chemistry (IUPAC) [14]. In microporous materials, the properties of pores such as the pore dimensions, the spe-

cific surface area, the micropore volume and the pore shape affect on their hydrogen adsorption behavior. Typically, the specific surface area of adsorptive materials can be measured and calculated by two techniques, which are Brunauer-Emmett-Teller (BET) and Langmuir methods. The Langmuir equation is generally used for materials which form a monolayer adsorption with adsorbed molecules, while the BET method includes multilayer adsorption. The surface areas obtained by using the BET method are usually larger than values calculated by using the Langmuir method [15].

An adsorption process is an exothermic process which releases heat. The heat of adsorption for physisorption (1 kJ/mol - 10 kJ/mol) is about ten times smaller than that observed in storage materials in which chemisorption is the dominant mechanism for hydrogen sorption. This is because the interaction between H_2 and host materials is weak. Releasing low heat during the adsorption process and rapid kinetics of hydrogen adsorption are good for refueling in mobile applications. However, the weak interaction results in low capacity of storing hydrogen at room temperature. Hydrogen storage capacities of this type of materials increase when temperature decreases. Bhatia and Myers [16] predicted the the optimum heat of adsorption of adsorptive materials should be about 15 kJ/mol·H_2 at 298 K. These optimal values is predicted for storing a large amount of hydrogen molecules at a charging pressure ($\sim$30 bar) and for releasing most of them at a discharging pressure ($\sim$1.5 bar). None of present absorbent materials satisfy this value [17].

1.2.1.1 Carbon-based materials

Carbon-based materials are attractive candidates for a hydrogen storage applications because they reveal high specific surface area (SSA), low mass, good adsorption and micro-porosity. In pure carbon, their hydrogen binding energies are in range of 4 kJ/mol to 5 kJ/mol, which are too weak for storing hydrogen at ambient tem-

perature [13]. From Eq. 1.2, α_S can be changed by modifying polarization or curvature of a surface. Various porous carbon-based materials, such as activated carbons (ACs), single-walled carbon nanotubes (SWCNTs), multi-walled carbon nanotubes (MWNTs), graphites and expanded graphites, have been explored for hydrogen storage propose.

Selected porous carbon materials are discussed in this section. Typically, activated carbons contains high micropores with large SSA (>3000 m^2/g) and high total pore volume (>1.5 cm^3/g). They are attractive, because they can be produced in a large scale. ACs is one of commercial candidates for carbon-based hydrogen storage materials. Various organic precursors such as coconut shells, soil bean and other agricultural wastes can be used. Their highly porous characteristics can be synthesized by physical activation or chemical reaction [18]. At 77 K, their average hydrogen capacity is ∼2.5 wt% at low pressure (1-10 bar), the higher capacity of 5.5 wt% can be gained at high pressures (∼60 bar) [19, 20]. However, the low adsorption (<1 wt% was measured at room temperature and 100 bar [21].

In 1997, the hydrogen adsorption in SWCNTs was first investigated by Dillion *et al.* [22]. Carbon nanotube is a rolled graphene sheet and its two ends are closed by two fullerene-like hemispheres. The curvature in carbon nanotubes plays an important role on their hydrogen adsorption properties. Their heat of adsorption is ∼25% higher than that in the flat graphite [8]. At room temperature, hydrogen adsorption capacities of SWCNTs are in the range of 0.1wt%-0.2 wt%. For MWNTs, their hydrogen storage densities are affected by the number of shell (N_s) and the tube diameter as shown in Fig. 1.5. Other forms of carbon nanotubes, such as bundle of single-walled carbon nanotubes, decorated carbon nanotubes, etc. , have been reported [23, 24]. However, carbon nanotubes show no significant advantage over other carbon materials because of difficulties in synthesis and purification for a large

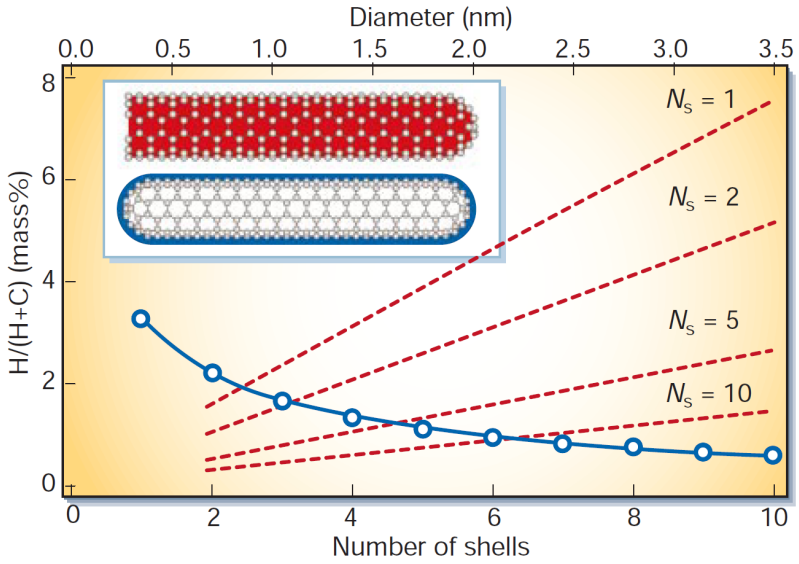

Figure 1.5: Calculated hydrogen storage density as a function of the number of shell N_s (blue) and as a function of the tube diameter (red).[8]

scale production.

There are many attempts to improve hydrogen adsorptions by other carbon based materials. Recently, new carbon materials called carbon aerogels (CAs) have been discovered for storing hydrogen [25, 26]. CAs are amorphous activated carbons which have large surface area up to 3200 m^2/g. At 77K, the maximum gravimetric density of 5.3 wt.% can be achieved under pressure of 20-30 bar. In a variety class of carbon nanomaterials, such as fullerenes, carbon nanofibers, graphite nanofibers, etc. , hydrogen uptake capacities are in range from 0.1wt% to >10 wt% [27, 28]. Nevertheless, carbon nanofibres, which have a capacity 67 wt% reported by Chembers *et al.* [29], cannot be reproduced consistently.

1.2.1.2 Metal-organic frameworks

Metal-Organic Frameworks (MOFs) are crystalline solids, which consist of metal ions (or clusters) bridged by organic ligands. The adsorption enthalpy of typical

MOFs is about 6 kJ/mol [30]. MOFs are attractive for storing hydrogen. In these materials not only is physisorption present, but H_2 can form sigma bonds with unsaturated metal centers. They have more choices for designing the structure compared with carbon materials. For instance, the choice of ligand sizes can modify the void spaces. The choice of constituent elements and structures can modify the polarization of frameworks. The choice of metals, which have different oxidation states, different electronic properties and different degrees of unsaturation, affects the number and strength of metal-hydrogen interactions [31].

Zn(II) and Cu(II) are the most common metal ions used in MOFs. Other metals such as Mn, Co, Ni, Cr, Mg, Al, alkali metals and lanthanide metals are also used for synthesis MOFs. For organic building blocks, various carboxylic acids and heterocyclic compounds with nitrogen donors can be used as linkers. Therefore, numerous MOFs can be synthesized and their hydrogen sorption capabilities have been investigated [32, 15]. For example, Rosi *et al.* reported that MOF-5 of composition $Zn_4O(BDC)_3$(BDC=1,4-benzenedicarboxylate) with a cubic three-dimensional extended porous structure can store hydrogen up to 4.5 wt% at 78 K and 20 bar, and reduce to 1 wt% at room temperature. When the organic linkers were modified from the BDC linkers of MOF-5 to cyclobutylbenzenes of isoreticular metal-organic framework-6 (IRMOF-6) and naphthalene linkers of isoreticular metal-organic framework-8 (IRMOF-8), the capacity is enhanced from $\sim$1.9 to 4.2 and 9.1 H_2 per formula unit, respectively, at room temperature and 10 bar [33]. Fig. 1.6 presents the three dimensional structures of MOF-5 , IRMOF-6, and IRMOF-8.

In the high pressure hydrogen uptake process, the quantity of adsorption can be represented by the total amount of adsorption (N_{tot}) or excess amount of adsorption (N_{ex}). The excess adsorption, known as the Gibbs excess, denotes the difference amounts of H_2 present in the same volume of adsorptive materials which

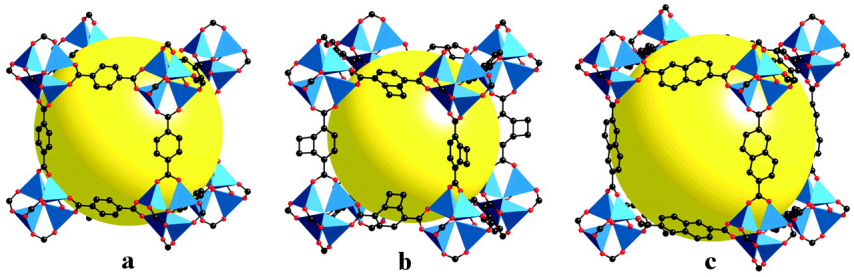

Figure 1.6: Three dimensional structures of (a) MOF-5, (b) IRMOF-6, and (c) IRMOF-8. The largest sphere which can be fit in the cavities is illustrated by the large yellow spheres that contact the van der Waals radii of the framework atoms(Zn:blue polyhedron, O:red spheres, C:black spheres). [33]

filled with hydrogen and absence of hydrogen. The relationship of N_{tot} and N_{ex} is $N_{tot} = N_{ex} + d_{gas}V_{pore}$, where d_{gas} is the compressed gas at a given temperature and pressure and V_{pore} is the pore volume [15]. The hydrogen storage capacities in MOFs increase linearly when the surface areas increase. So far, there are many efforts to enhance the adsorption interaction between H_2 and MOFs such as using functional ligands, generating open metal sites, catenation, constraining pore size, alkali metal ion inclusion, embedding of nanoparticles (i.e. Pt or Pd) [33]. For constraining pore size method, the pore size and the surface area have to be balanced since smaller pore relates to smaller surface area. Catenation is the intergrowth of two or more identical frameworks that can reduce pore size of MOFs. This method shows improvement of hydrogen adsorption in MOFs [34]. Doping MOFs with catalyst can enhance the storage capacity because catalyst hydrogen molecules are split and stored as hydrogen atoms. However, embedded nanoparticles (i.e. Pd or Pt) may block the pore and reduce pore volume of MOFs [15]. Fig. 1.7 shows the hydrogen storage capacities at 77 K as a function of the surface area of some selected MOFs.

Similar to other physisorption materials, their hydrogen uptake quantities dramatically reduces at room temperature. One important thing that should be con-

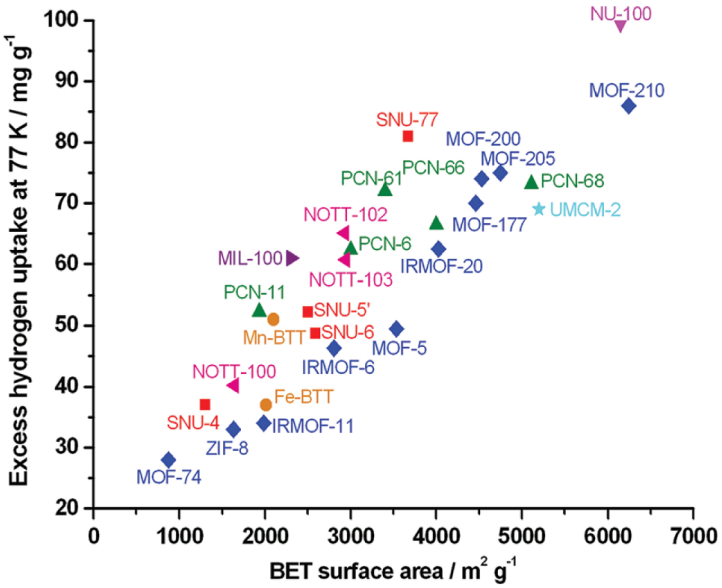

Figure 1.7: The hydrogen storage capacities at 77 K as a function of the BET surface areas for selected MOFs [15]

sidered is the stability of MOFs in operating conditions. Most MOFs are sensitive to moisture, acids or bases. Hence, designing of MOFs need be considered in aforementioned issues.

1.2.1.3 Other microporous materials

Zeolites are the three-dimensional alluminosilicates. Even though zeolites seem to be a good hydrogen capacity owing to their highly porous and high surface area. In fact, their hydrogen adsorption capacities are low due to their limited pore volume. They can store hydrogen less than 2 wt% at liquid nitorgen temperature and very low capacity (<1 wt%) at room temperature[1, 35]. They are not good candidates for hydrogen storage applications. Nevertheless, many adsorptive materials demonstrate good hydrogen storage capacities at 77 K (the liquid nitrogen temperature) and high pressures, those capacities become low at ambient conditions. These features are not

suitable for practical applications. This is the main disadvantage of these materials.

Concisely, among physisorption materials, ACs and MOFs are the most promising candidates for hydrogen storage applications.

1.2.2 Reversible metal-based hydrides

Hydrogen can be stored as hydride compounds by chemisorption processes. A good volumetric hydrogen capacity can be achieved by this procedure. Molecular H_2 are dissociated into hydrogen atoms (H), bound to host atoms and form hydride compounds. When hydrogen atoms are attached in host materials by chemical bonding, heat is required for breaking chemical interaction and releasing hydrogen in the dehydrogenation step. The desorption temperature strongly relates to the stability of the hydride structure. The stability of metal hydrides can be explained by the enthalpy of formation/the heat of formation (ΔH). Generally, the sorption properties of metal hydrides can be probed by pressure–composition temperature (PCT) study, which is also called the pressure-composition isotherm (PCI) method. This method depicts the relationship between the hydrogen pressure and hydrogen composition in films under isothermal loading and unloading conditions. An example of PCT curve is illustrated in Fig. 1.8. The corresponding transformation from solid solution (α) to hydrided phase (β) is displayed at the bottom of Fig. 1.8. The logarithm of the plateau pressure can be plotted versus 1/T. This correlation can be described by Van't Hoff's equation in Eq. 1.3.

$$ln[\frac{p_{eq(H_2)}}{p^0_{eq}}] = \frac{\Delta H}{RT} - \frac{\Delta S}{R} \tag{1.3}$$

where $p_{eq(H_2)}$ and p^0_{eq} are the plateau (equilibrium) pressure and the thermodynamic reference pressures, respectively. Typically, p^0_{eq} refers to atmospheric pressure, which is 1 bar. R and T are the gas constant and absolute temperature, respectively.

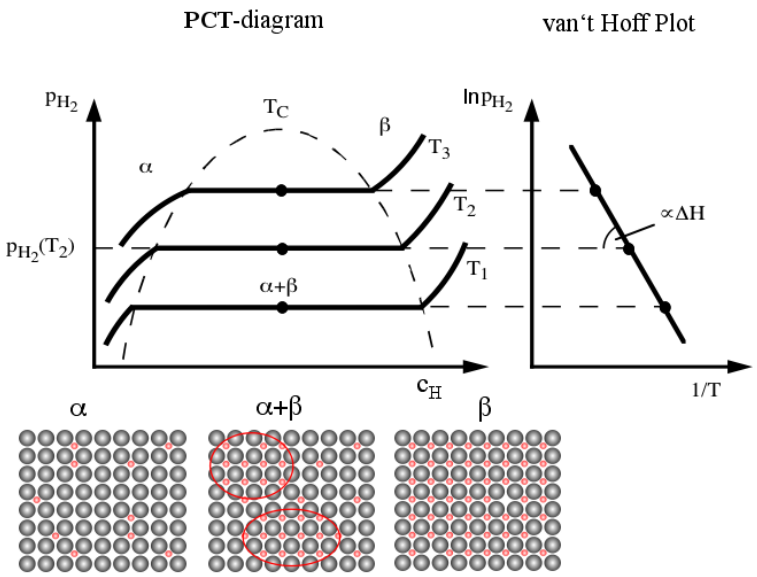

Figure 1.8: The relationship between Pressure-Concentration-Temperature (PCT) curve (left) and Van't Hoff plot (right). The simple schematic of the solid solution phase (α), the fully hydrided phase (β) and the coexisted phases (α+β) are represented at the bottom. [36]

ΔH and ΔS represent the corresponding variation of enthalpy and entropy. Van't Hoff's equation can be used to estimate the desorption temperatures of metal hydrides through their formation entropy (ΔS_f) and formation enthalpy (ΔH_f) [8, 17]

The first absorption hydrogen in metals was observed in paladium (Pd) in 1866 [37]. Although Pd provides an excellent sorption property, its cost is the main problem for usage. Other metals have been sought out to replace Pd. As mentioned before, the weight of host materials affects the gravimetric density. The light metal hydrides have been focused for satisfying the weight requirement.

1.2.2.1 Light weight binary metal hydrides

The reaction of $M + \frac{x}{2}H_2 \rightleftarrows MH_x$ describes a formation of binary metal hydride (MH_x). Following the periodic table, the various hydride forms of light elements

(i.e. lithium (Li), beryllium (Be), sodium (Na), magnesium (Mg), boron (B) and aluminium (Al), have been investigated for hydrogen storage purpose [31]. Starting from the first row of the periodic table, lithium hydride (LiH) provides 12.7 wt.%. However, it is too stable and it needs very high temperature (∼850 ^{o}C) to release hydrogen. Beryllium can store hydrogen up to 18.3 wt.% and release hydrogen at lower temperature (∼250 ^{o}C) than in LiH. However, it is toxic and expensive. Sodium hydride (NaH) has the capacity less than 5 wt.%, and its stability is as high as LiH [31]. The next candidate is Mg. Its hydride phase is MgH_2, which stores hydrogen up to ∼7.6 wt.%. It is abundant and inexpensive. Again, typical MgH_2 is very stable (ΔH_f ∼-75 kJ/molH_2), it requires >300 ^{o}C for dehydrogenation [38]. Among light binary metal hydrides, MgH_2 is the most promising candidate for storing hydrogen due to their advantages. The development of Mg-based hydrogen storage will be reviewed in a further section. For Al, aluminium hydride (AlH_3) shows 10.1 wt.% hydrogen capacity and has less stability (ΔH_f ∼-10 kJ/molH_2). However, this material stores hydrogen irreversibly [28, 39]. In summary, these binary metal hydrides are not satisfied the on-board applications. Therefore, many methods, such as adding transition metals as catalysts, forming more complex hydrides, etc. have been used for enhancing their thermodynamics.

1.2.2.2 Complex hydrides

For complex hydrides, sodium alanates ($NaAlH_4$) are now considered promising materials due to their low cost and high reversible capacities of the bulk materials. In 1997, Bogdanović first proposed that the reversible hydrogen absorption/desorption in $NaAlH_4$ can be achieved by doping transition metal catalysts (e.g. Ti) [40]

The reversible hydrogen sorption of $NaAlH_4$ have two individual steps presented

in the following reactions,

$$3NaAlH_4 \rightleftarrows Na_3AlH_6 + 3Al + 3H_2 \quad (\Delta H = 37kJ/molH_2) \tag{1.4}$$

$$Na_3AlH_6 \rightleftarrows 3NaH + Al + \frac{3}{2}H_2 \quad (\Delta H = 37kJ/molH_2) \tag{1.5}$$

The first reaction discharges 3.7wt.% of hydrogen at $\sim 190^oC$, while the second reaction releases 1.8wt.% of hydrogen at $\sim 225^oC$. NaH also releases hydrogen at above 400^oC, but this temperature is higher than the temperature of interest. Hence, their hydrogen capacity is reduced from 7.5 wt.% to 5.6 wt.%, when the high temperature is neglected.

Nevertheless, more improvements are required for realistic use. First, their hydriding and dehydriding kinetics need to be improved. Some methods have been applied for enhancing their kinetics, such as doping of catalysts (i.e. Ti, Ce-based species and Sc) and reducing their particle size [41, 42, 43]. Reducing the particle size of $NaAlH_4$ leads to lowering of their gravimetric densities. However, their kinetics remain slow for the real fuel cell vehicle [44]. Another issue is the 5.6 wt.% theoretical capacity cannot be reached, because Na_3AlH_6 is too stable in working condition. These compounds are highly sensitive with water and air, raising safety concerns during operation.

Other complex hydrides, which have an alkali cation and an anion similar to $NaAlH_4$ and have lower molecular weights, have been studied. For instant, replacing of Na by Li to form lithium aluminum hydride shows better kinetics and lower dehydrogenation temperature, but the reversible hydrogenation is difficult. Another example is substituting Al with B. Unexpectedly, sodium borohydride is decomposed to other products easily. Therefore, it is difficult to obtain reversible sorption reactions like $NaAlH_4$ does. Another well known complex hydride is Lithium borohydride

($LiBH_4$). This compound show the attractive capacity of 18.5 wt.% and less stability of its hydride form compared to others. This compound has been actively studied for the hydrogen storage applications [31].

1.2.3 Other materials

1.2.3.1 Clathrates

Another method of storing hydrogen is the encapsulation by forming clathrates. In 1999, Dyadin *et al.* firstly proposed that hydrogen can form clathrates. Hydrogen molecules (guest molecules) are trapped in hydrates/water host lattices (cage material), and form hydrogen clathrate hydrates at high pressure (up to 1.5 GPa) [45]. There are three common clathrate hydrate lattices, called sI ($Pm\bar{3}n$ lattice), sII ($Fd\bar{3}m$ lattice) and sH ($P6/mmm$ hexagonal lattice). Fig. 1.9 displays forming of each type clathrate hydrate from different types of cavities, such as 5^{12} (small cavity containing 12 pentagonal faces), $4^3 5^6 6^3$ (medium cavity containing 3 square, 6 pentagonal and 3 hexagonal faces), and so on. The second hydrate form (sII) has been widely elucidated for hydrogen storage applications.

There are many advantages of using hydrogen clathrate hydrates in the hydrogen technology. For example, the by-product of hydrates is water, which is reusable, clean and compatible with fuel cells. Their kinetics of formation and decomposition are fast. Low heat is released due to their low hydrogen binding energy. However, the main limitation of using hydrogen clathrate hydrates is they require high pressures (or very low temperature at ambient pressure) for forming and stabilizing the structures [27]. In 2004, Florusse *et al.* introduced Tetrahydrofuran (THF) as the second guest molecule (called promoter) for stabilizing the hydrogen clathrate hydrate at lower pressure. Comparing with the formation of pure hydrogen clathrate hydrates, this binary H_2-THF sII clathate is formed at much lower pressure ($\sim$5 MPa) at

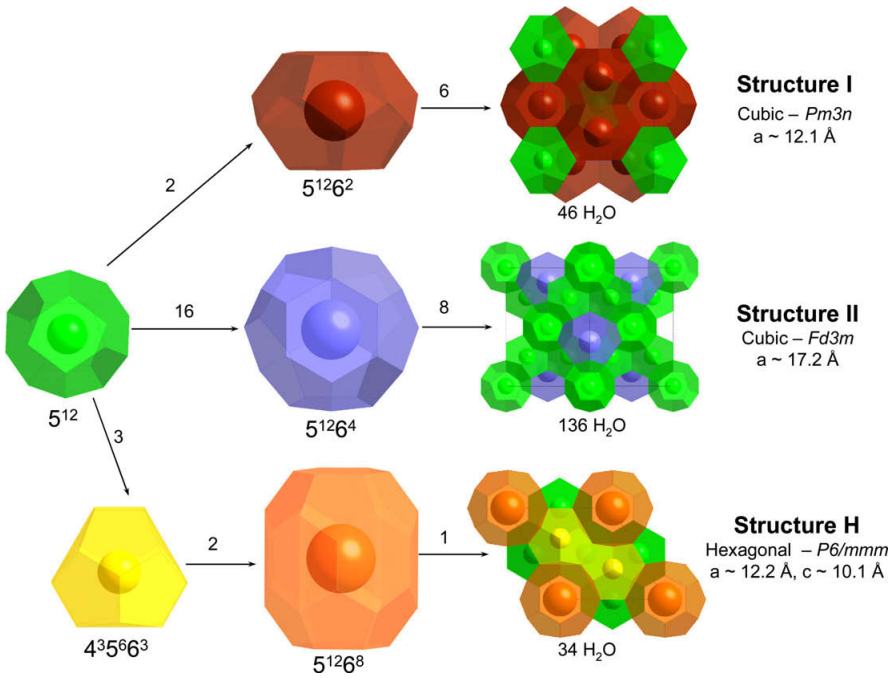

Figure 1.9: Three common clathrate hydrate lattices [27]

280K [46]. Other promoters were introduced, such as furan (F), 2,5-dihydrofuran (DHF), tetrahydropyran (THP) and 1,3-dioxolane (Diox). However, those suggested promoters are not as good as THF [17]. The main challenge of this materials is enhancement their hydrogen storage capacities under suitable working conditions.

So far, each of the current materials under investigation has advantages and disadvantages, but none of them fulfils all the requirements. For example, complex hydrides have good reversibility only at high temperatures and pressures. The more complex the structure is, the less effective reversibility can be attained. The carbon-based materials, such as carbon nanotubes, activated carbons and carbon nanofibers, provide high capacity and fast kinetics by physisorption process. Like other physisorption materials, MOFs also show impressive hydrogen sorption properites at liquid nitrogen temperature. However, the hydrogen uptakes in those adsorptive

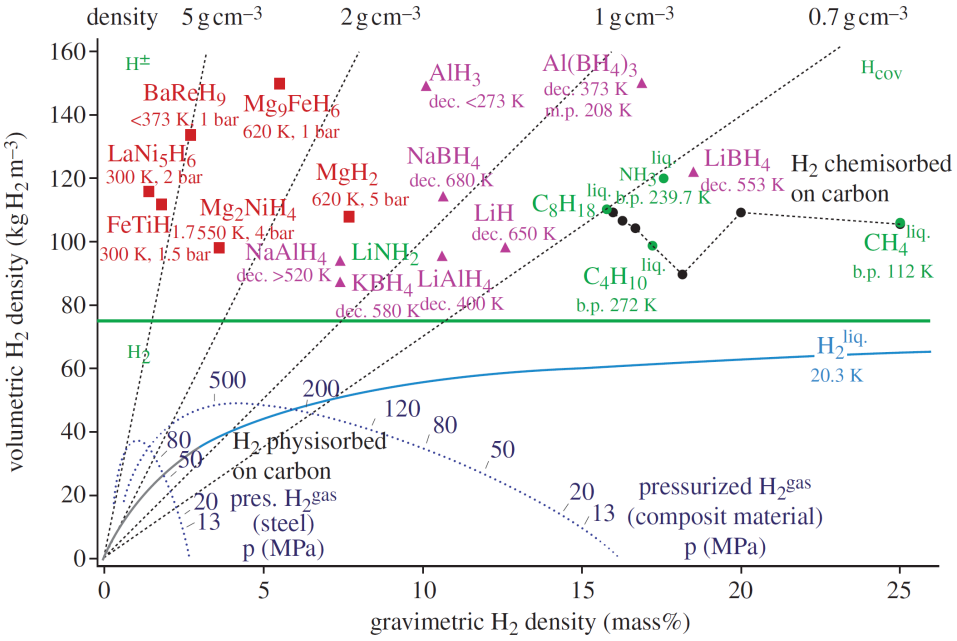

Figure 1.10: Comparison of volumetric and gravimetric hydrogen density of some selected hydrides [2]

materials are low at ambient conditions, which can be improved only at cryogenic temperatures and/or high pressures. Volumetric and gravimetric hydrogen density of selected hydrogen storage are compared in Fig. 1.10. Apparently, hydrogen storage materials need to be improved for practical applications.

1.2.4 Mg-based materials for hydrogen storage

As described in the preceding section, MgH_2 has promising aspects such as good gravimetric capacity, reversibility, cheap price and abundant. In bulk Mg, a tetragonal/rutile-type MgH_2 (T-MgH_2) is its stable phase at ambient conditions. However the hydrogen sorption properties of this bulk hydride form are hindered by kinetics and thermodynamic limitations. Because of the high stability of T-MgH_2, it releases hydrogen at a very high temperature and required hydrogen pressure greater than 3 MPa. In addition, the oxidation occurs, when it is exposed to air. MgO is

formed at the surface and impedes the hydrogenation process. MgO layer need to be dissociated before absoption process occurs. This process requires high temperature at the initial step. Even those Mg-O bonds are broken, the rate of hydrogen dissociation at the Mg surface is still slow due to a high dissociation energy. In addition, forming of MgH_2 phase at the surface obstruct the diffusion of other hydrogen atoms. Hydrogen atoms prefer diffusing along the interface than moving through the hydride layer. Therefore, it requires several hour to be fully loaded hydrogen in Mg, even at high temperature [47, 38]. The hydrogen pressure also affects on the grow rate of MgH_2. From literature, the adsorption and desorption properties in Mg-based materials can be enhanced by many approaches such as adding catalysts or additives, reducing size by using a ball milling approach, and using thin film engineering.

In 1999, Hout *et al.* reported that hydrogenation kinetics in bulk MgH_2 can be improved by using the ball (mechanical) milling method[48]. Sorption kinetics of milled MgH_2 shows five time faster than that of typical MgH_2. Using the ball milling technique would change a crystal structure, introduce structural defects and increase the specific surface area, which shorten the diffusion lengths and increase the nucleation sites in the materials. These factors promote the faster hydrogen sorption kinetics in MgH_2. In spite of the enhancement in kinetic property, its thermodynamic remains poor. The full absorption and desorption occur at $\sim 300^o$C and $\sim 350^o$C, respectively. Nowadays, ball milling techniques (i.e. mechanical grinding, mechanical alloying and reactive ball milling) are most widely used in preparation of Mg-based hydrogen storage materials [49].

On the other hand, improving the sorption properties of Mg hydride can be performed by adding catalysts. The transition metals or their oxides such as Nb, Ti, V, Sc, Ni, Fe, Mn and others have shown the catalytic effect on the sorption properties of Mg hydride[50, 51, 52, 53, 54, 55]. The addition of catalyst can be done by using

ball milling methods also. For example, catalytic effects of several metal oxides (i.e. Nb_2O_5, Fe_3O_4, Cr_2O_3, V_2O_5, TiO_2) prepared by the ball milling technique, were compared by Barkhordarian *et al.* [53]. As a result, the Nb_2O_5 additive exhibits the most enhancement of hydrogen sorption properties compared to other studied metal oxides. At 250^{o}C, this Nb_2O_5 catalyzed MgH_2 desorbs hydrogen faster than the Nb catalyzed MgH_2. At that temperature, it releases amount of 6.6wt%H_2 which is greater than that in the Nb catalyzed MgH_2 (4.5wt%H_2). The alloy formation with other metals is another useful method. The mechanical alloying and milling can be used for preparing materials. Lowering of hydrogen desorption temperature was observed in Mg_2NiH_4. This aspect was first proposed by J.J Reilly and R.H. Wiswall [56]. ΔH_f reduces to -65 kJ/mol H_2 in Mg_2NiH_4 alloy [38]. More improvement has been found in $Mg_{20-x}La_xNi_{10}$, when La substitutes at Mg position in Mg_2Ni [57]. $Mg_{20-x}La_xNi_{10}$ (x=2) optimizes hydrogen desorption kinetics at 200^{o}C.

Thin films technology is one useful tools for improving in hydrogenation properties of metal hydrides [58, 59]. This technique provides many advantages such as increasing surface area and raising hydriding/dehydriding rate. In addition, the surface of thin films can be coated to avoid oxidation of Mg. Also, the catalyst layer can be deposited on top of the films to assist the hydrogen dissociation process at the surface. The surface orientation and degree of crystallinity play an important role on the sorption kinetics of hydrogen in Mg thin films [60]. The significant improvement of the thermodynamics was observed in three layered Pd/Mg/Pd films proposed by Higuchi *et al.* [61]. The films releases hydrogen at much lower temperature ($\sim$360K) than bulk MgH_2, but the hydrogen capacity also decreases to 5 wt.%. Yoshimura *et al.* reported that the observed intermixing of Mg and Pd at the interface results faster forming of MgH_2 phase at room temperature

Desorption properties of selected Mg-based materials are compared to the prop-

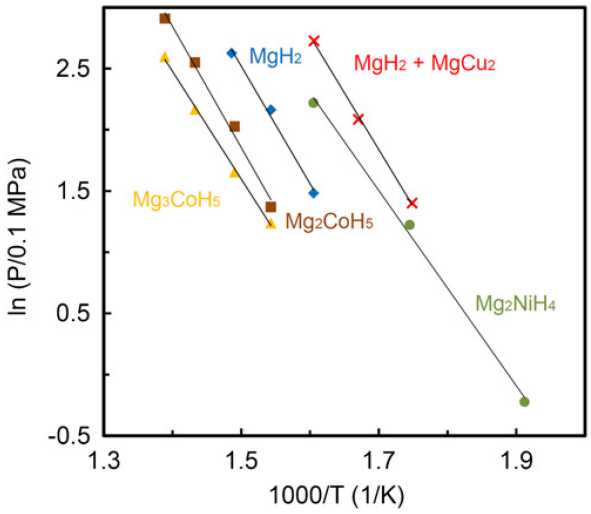

Figure 1.11: Van't Hoff plot for desorption of different Mg-based nanoparticles. [49]

erty of bulk MgH_2 shown in Fig. 1.11. As stated before, the desorption temperature influenced by the stability of the hydride structure and it can estimated from ΔH_f and ΔS_f by using Van't Hoff's equation (Eq. 1.3). As present in Fig. 1.11, the stability of these hydrides decreases as the following order; Mg_2CoH_5, MgH_2, MgH_2+$MgCu_2$, Mg_3CoH_5 and Mg_2NiH_4.

Besides those methods mentioned previously, there are other procedures for enhancing Mg-based hydrogen storage materials. In one interesting example, buried Mg_H nanocrystals (NCs) inside a PMMA gas selective polymer matrix provides a good hydrogen sorption kinetics (30 minutes at 200^{o}C). This Mg NCs/PMMA nanocomposite displayed in Fig. 1.12 is an air-stable material which allow only hydrogen gas pass through the polymer shell. This composite material can store hydrogen up to 4 wt.% for the composite.

In summary, the Mg-based materials is one of the most promising hydrogen storage. The ultimate goal is achieving all good sorption properties and good capacity

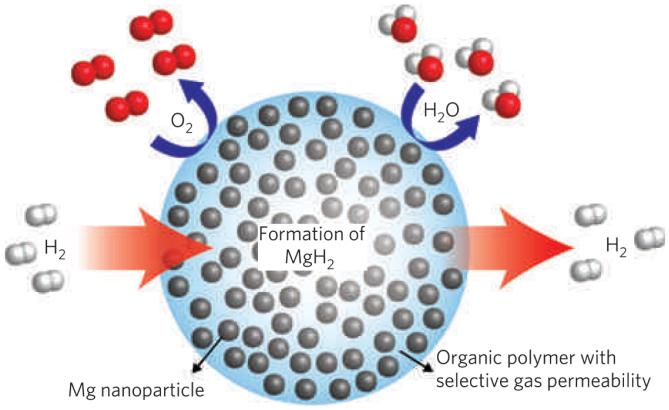

Figure 1.12: Schematic of hydrogen storage of Mg nanocrystals are encapsulated by a selectively gas-permeable polymer [62]

required in the practical applications. The development of Mg-based materials will still be the on-going step.

2. METHODOLOGY: COMPUTATIONAL METHOD

2.1 Computational methods used in hydrogen storage materials

Computational methods such as density Functional Theory (DFT), Monte Carlo (MC), Molecular Dynamics (MD), Phase Field modeling, etc. have become useful tools for investigating properties and understanding important phenomena in materials [63, 64]. For instance, MC simulations have been used for elucidating hydrogen storage properties in carbon-foam, nanostructured graphite platelets and MOFs [65, 66, 67]. The DFT method is one of the most powerful tools for investigating the fundamental properties of hydrogen storage materials. This method has been widely used for predicting free energies and formation enthalpies of hydrides, predicting the equilibrium phases of hydride structures, calculating thermodynamic properties, investigating the dissociation of hydrogen on the surface of materials, studying hydrogen diffusion mechanisms inside materials and predicting novel hydrogen storage materials [68, 69, 15, 70, 71, 1]. In this study, DFT methods have been used to investigate properties of Mg-based materials and their hydrogenation properties. The basic theory of the DFT method, its applications and its limitations are introduced in this chapter.

2.2 Density Functional Theory (DFT)

2.2.1 The many body electronic system

In quantum mechanics, behavior of any electronic systems can be predicted by solving the Schrödinger equation. The Schrödinger equation of many electron system

is expressed in Eq. 2.1.

$$\hat{H}\Psi(r_1, r_2, ..., r_N) = E\Psi(r_1, r_2, ..., r_N) \tag{2.1}$$

where $\hat{H}$ is the Hamiltonian operator. Ψ and E are eigenstates of the Hamiltonian (or electron wave functions) and associated eigenvalues (or the ground state energy of the electrons), respectively. N represents the number of electrons.

In a complex system, which consists of many interacting electrons and many nuclei, the Hamiltonian can be written as:

$$\hat{H} = -\frac{\hbar^2}{2m_e}\sum_i \nabla_i^2 - \sum_{i,I}\frac{Z_I e^2}{|r_i - R_I|} + \frac{1}{2}\sum_{i\neq j}\frac{e^2}{|r_i - r_j|} - \sum_I \frac{\hbar^2}{2M_I}\nabla_I^2 + \frac{1}{2}\sum_{I\neq J}\frac{Z_I Z_J e^2}{|R_I - R_J|} \tag{2.2}$$

where m_e is the electron mass. e_i and Z_I denote the charges of an electron i and a nucleus I, respectively. The first and the fourth terms represent the kinetic energy terms of the electrons and the nuclei, respectively. The second term represents the interaction between nuclei and electrons. The third term shows the electron-electron interaction. Lastly, the interaction between a nucleus and another nucleus is denoted by the last term. The full electronic wave function (Ψ) is a function of each of the spatial coordinates of each N electrons that is represented as:

$$\Psi = \Psi(r_1, ..., r_N) \tag{2.3}$$

In general complex systems, there are many electrons involved, and solving the Schrödinger equation is much more difficult than when studying a simple system. In fact, only very simple systems, such as an hydrogen atom, have been rigorously solved using explicit solutions to the Schrödinger equation. In order to simplify the

problem, the Born-Oppenheimer approximation is used. Under this approximation, the nuclei are assumed to remain static while the electrons are free to 'move' or relax. This approximation is justified in most cases since the nuclei, having much larger masses, move at a much slower rates than the electrons. This approximation, however, becomes invalid under very energetic conditions or when processes occur at very fast rates. In the particular case under study, the Oppenheimer assumption holds, and the therefore the kinetic term of the nuclei can be neglected. Eq. 2.2 can be rewritten as:

$$\hat{H} = \hat{T} + \hat{V}_{ext} + \hat{V}_{int} + E_{II} \tag{2.4}$$

where $\hat{T}$ is the first term in Eq. 2.2. $\hat{V}_{ext}$ is the potentials acting on the electrons due to the nuclei. The last term, E_{II}, is the interactions among nuclei [72].

Even under the Oppenheimer approximation, however, we still have a many-body system that is extremely difficult to solve explicitly, and other approximation methods have been proposed for simplifying this many-body problem. Examples of these approximations are the non-interacting (Hartree-like) electron approximation and the Hartree-Fock approximation. These two methods assume that the electrons are uncorrelated to each other but that they obey the exclusion principle. While powerful, these approximations are still difficult to implement in a practical way whenever the number of electrons is large. The solution to the resulting equations needs to account for the individual electronic degrees of freedom explicitly.

2.2.2 The Kohn-Sham equation in DFT method

In 1964, the DFT method was introduced by Kohn and Sham [73]. This method reduces the complexity of the electronic many-body interactions into an effective one electron potential (the exchange correlation functional), which depends exclusively on

the electron density ($n(r)$). The key insight of this theory is the idea that the energy of a system in its ground state is variational with respect to the electron density: there is only one electron density distribution consistent with the ground state of the system. If this electron density is found, then it is possible to describe the electronic degrees of freedom as well as their changes when the system is perturbed. Thanks to this powerful idea it is possible to calculate many important and fundamental physical properties of atomic arrangements. The electron density ($n(\mathbf{r})$) can be calculated by sums of the orbitals for each spin (σ) as the following expression:

$$n(\mathbf{r}) = \sum_{\sigma} n(\mathbf{r}, \sigma) = \sum_{\sigma} \sum_{i=1}^{N^{\sigma}} |\psi_i^{\sigma}(\mathbf{r})|^2 \tag{2.5}$$

Within DFT, the many-electron Schrödinger equation is reformulated in terms of the Kohn-Sham equation shown in Eq. 2.6. From now on, Hartree atomic units, $\hbar$=m_e=e=$4\pi/\epsilon_0$=1, will be used for simplifying the equations.

$$\Big[-\frac{1}{2}\nabla^2 + V_{eff}^{\sigma}(\mathbf{r}) \Big] \psi_i^{\sigma}(\mathbf{r}) = \epsilon_i^{\sigma} \psi_i^{\sigma}(\mathbf{r}) \tag{2.6}$$

$$V_{eff}^{\sigma}(\mathbf{r}) = V_{KS}^{\sigma}(\mathbf{r}) = V_{ext}(\mathbf{r}) + V_{Hartree}(\mathbf{r}) + V_{xc}^{\sigma}(\mathbf{r}) \tag{2.7}$$

where the effective potential ($V_{eff}^{\sigma}(\mathbf{r})$) or the Kohn-sham potential ($V_{eff}^{\sigma}(\mathbf{r})$) can be described by three separate terms expressed in Eq. 2.7. $V_{ext}(\mathbf{r})$ represent the external potential, which includes any interaction between electrons and the nuclei, and any interaction due to other external fields. The second term is the Hartree potentials ($V_{Hartree}(\mathbf{r})$) that describe the self-interaction (or the Colombic interaction) of the electron density $n(r)$. Since $V_{Hartree}$ term includes a Coulomb interaction between the electron and itself, the self interaction can not be described explicitly. Then, the last potential term ($V_{xc}^{\sigma}(r)$) is provided for the correction of several effects. This $V_{xc}^{\sigma}(\mathbf{r})$ is

the exchange-correlation potential. While the exact form of this exchange-correlation functional is unknown for complex systems, it has been calculated using Quantum Monte Carlo methods for a simple electron gas and from the parametrization of this functional, general expression for this potential can be derived in terms of local and non-local (i. e. gradients) properties of the electronic charge distribution.

The ground state energy functional derived from the Kohn-Sham method is present in Eq 2.8. In this equation, a functional of the density $n(r, \sigma)$ is expressed by $[n]$.

$$E_{KS} = T_s[n] + \int dr V_{ext}(\mathbf{r}) n(\mathbf{r}) + E_{Hartree}(n) + E_{II} + E_{xc}[n] \tag{2.8}$$

2.2.3 The exchange-correlation approximation

As stated above, the real form of V_{xc} can not described explicitly. The exchange-correlation term needs to be approximated in order to achieve the ground state properties of the many-body electronic system. The examples of approximation approaches are the local density approximation(LDA)[74], the generalized-gradient approximation (GGA)[75], and the hybrid functionals [76, 77]. In the LDA method (or Local Spin Density Approximation (LSDA)), $E_{xc}[n]$ is an integral over all space with the exchange-correlation energy density at each point, which have the same exchange-correlation energy per electron of homogenous electron gas at a same density n (ϵ_{xc}^{hom}). The general form of E_{xc}^{LSDA} is:

$$E_{xc}^{LSDA}[n\uparrow, n\downarrow] = \int d^3r \; n(\mathbf{r}) \epsilon_{xc}^{hom}(n\uparrow(\mathbf{r}), n\downarrow(\mathbf{r})) \tag{2.9}$$

Secondly, the GGA method uses both the local electron density and the local gradient in the electron density (∇n). Its exchange-correlation energy is expressed

in the following equation:

$$E_{xc}^{GGA}[n\uparrow, n\downarrow] = \int d^3r\ n(\mathbf{r})\epsilon_{xc}(n\uparrow, n\downarrow, |\nabla n\uparrow|, |\nabla n\downarrow|, ...) \tag{2.10}$$

Another example is the hybrid functional, this method combines orbital-dependent Hartree-Fock and an explicit density functional (i.e. LDA and GGA) together. For example, the half-and-half form can be represent as:

$$E_{xc} = \frac{1}{2}(E_x^{HF} + E_{xc}^{DFA}) \tag{2.11}$$

HF and DFA stand for the explicit density functional and orbital-dependent Hartree-Fock terms, respectively. The well known functional is B3LYP (Becke,3-parameter-Lee-Yang-Parr) hybrid functional [76, 77]. This hybrid functional is widely used in molecular calculations in computational chemistry. In addition, other functionals such as the self-interaction correlation (SIC), the optimized effective potential method (OEP) and the exact exchange (EXX) were also developed [72].

2.2.4 Solving the Kohn-Sham equation

Because all the effective potential $V_{eff}^{\sigma}(r)$, electron density $n(\sigma, r)$ and the wave function ($\psi^{\sigma}(r)$) are related to each other, the Kohn-sham equation needs to be solved by a self-consistent method illustrated in Fig. 2.1. The criteria of the calculations are the consistency of $V_{eff}^{\sigma}(r)$ and $n(\sigma, r)$ [72].

At the beginning, a trial electron density—for example, an electron density consistent with that of isolated atoms—is defined and used for calculating the effective potential in the next step. Next the Kohn-Sham equation is solved and gives the new electron density. The calculated electron density is compared to the input one. If these two electron densities are the same, this electron density is the ground state

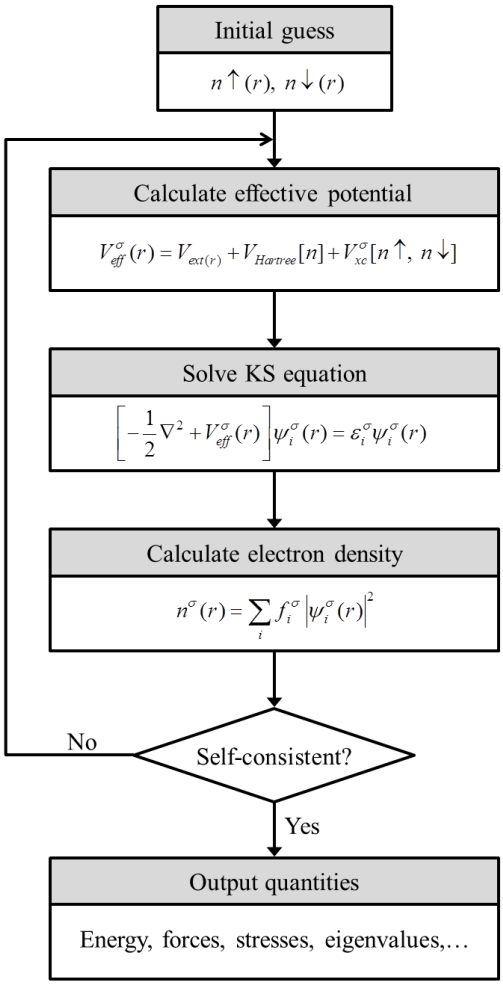

Figure 2.1: A schematic of a self-consistent calculation [72]

electron density. It will be used for determining other properties such as energies, forces, and stresses. On the other hand, if the calculated electron density differs from the previous value, the initial electronic density will be updated (i.e. linear mixing and Broyden mixing) and put into the new loop again.

2.2.4.1 Wave functions

Typically, the electron wave functions ($\psi_i(r)$) are described as a linear combination of a finite number of basis functions. In practice, using the full form of the wave functions needs expensive computational resources, especially in complex systems. Three applicable methods, which are linear combinations of atomic orbitals (LCAOs), plane wave, augmented plane waves (APWs), are widely used for the calculation of independent-particle electronic states of materials [72, 78]. Firstly, in the LCAOs approach, wave function are written as a linear combination of localized atomic-like orbitals (i.e. Gaussian-type orbitals (GTOs) and Slater-type orbitals (STOs)). This method is famous in Chemistry and it can enable efficient calculations with appropriate choices of basis sets, and small number of basis sets can be used to get a reasonable result. Nevertheless it depends on the position of atoms and the Pulay force is needed for correcting the error [79].

In plane wave (PW) approach, wave functions are expanded as a summation of plane waves. This method is simple to implement and suitable for periodic lattices. The Fast-Fourier transform (FFT) can expedite the calculations. Moreover, plane waves do not rely on the atomic positions. The forces are calculated directly from the Hellmann-Feynman theorem [80] without the Pulay correction term. However a large number of plane waves are needed to reach a good convergence.

In APWs, the atomic sites and interstitial regions are separated and represented in different ways. Spherical harmonic functions are used for the wave functions

inside the atomic sites, while plane waves are used at the interstitial sites. Even if the suitable functions are applied to specific regions, those functions are required to be matched. Examples of APWs methods are the multiple-scattering theory (MST), the muffin-tin orbital (MTO), and the linearized augmented plane waves (LAPWs). Full-potential-linearized-APW (FLAPW) method is the all-electron calculation. It does not apply any shape approximation to the effective one-electron potential. This approach provides the most accurate result, but requires a high computational cost.

To overcome the difficulties of the LCAO approach, the pseudopotential approach was introduced. The pseudopotential approach treats atomic sites as the core orbitals and the valence orbitals. The wave functions of the core region and the valence orbitals close to the core region are reshaped from the nodal characteristic to the nodeless pseudo-wave function as show in Fig. 2.2. In another word, wave functions of a nucleus and core electrons are substituted by a fixed effective one, while the outer valence orbitals, which significant to the chemical bonding, remain the same. Many pseudopotentials have been developed. The two important keys of development of pseudopotentials are the transferability, which means it can be used in all system (i.e. molecule, cluster, surface), and the softness, that refers to fewer plane waves are involved the softer it is. The examples of pseudopotentials are the norm-conserving pseudopotential (NCPPs) and the ultra-soft pseudopotentials (US-PP).

Based on the pseudopotential method, the projector-augmented-wave (PAW) method was developed [82]. This method incorporates both the pseudopotential approach and the augmented wave method together. A basic idea of this method is given in Fig. 2.3. This method applies auxiliary localized function around each atom similar to the US-PP approach, and keeps the full all-electron wave functions in atomic sites like APW method. This approach is as accurate as the all electron approach.

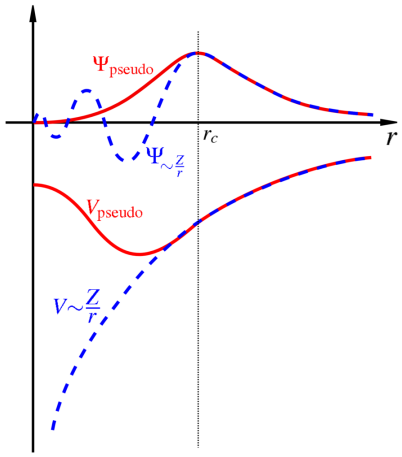

Figure 2.2: Pseudopotantial and Pseudo wave function. The blue dash lines represent the real wave function and the real potential. The red lines are the pseudo-wave function and the pseudopotential r_c is the cut off radius. [81]

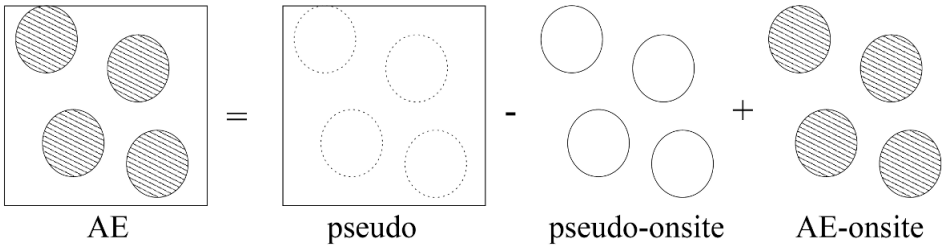

Figure 2.3: A simple schematic of PAW approach. AE and pseudo stand for an all electron and a pseudopotential regimes. [81]

2.2.5 The DFT calculations in periodic solids

In periodic solids, atoms in their crystal structures arrange periodically in space. The Bloch theorem can be applied for describing the wave function in this type of materials. When the plane wave-based methods are comprised in periodic materials, some important variables should be considered in order to get a good result. For example, cutoff kinetic energy (E_{cut}) relates to the number of plane waves involving in the calculation. In the plane wave-based methods the calculations are performed

in the reciprocal spaces and FFT is used for transforming the wave functions and electron density between the reciprocal and real spaces. The number of k-point meshes, sampling in Brillouin zone (BZ) of the reciprocal space, affects on the accuracy and the computational effort of calculation. Monkhorst-Pack scheme[83] is the most popular method for generating k-points. BZ integration methods (i.e. the special-point scheme[84] and the tetrahedron method[85]) are also significant. The famous method is tetrahedron method.

In summary, the suitable choices of parameters, such as the exchange-correlation functional, basis sets, pseudopotentials, k-point meshes affect, and numerical methods for solving KS equations, need to be considered in DFT calculations.

2.3 Properties evaluated from DFT calculations

2.3.1 Applications and limitations

Generally, DFT calculations are performed at 0 K. The ground state properties of materials such as equilibrium structure, cohesive energy, phase transitions, elastic properties, charge density, magnetic order, etc. , can be attained by using the DFT method. For instance, the energy (E), pressure (P) and bulk modulus (B) can be gained from DFT calculations as shown in the following relationship[72]:

$$E = E(\Omega) \equiv E_{total}(\Omega) \tag{2.12}$$

$$P = -\frac{dE}{d\Omega} \tag{2.13}$$

$$B = -\Omega\frac{dP}{d\Omega} = \Omega\frac{d^2E}{d\Omega^2} \tag{2.14}$$

where Ω stands for a cell volume. A number of particles is fixed in all quantities. One example is the calculation of equation of state (EOS). The energies (E) are calculated as a function of volume (Ω). The plot is fit analytically (e.g. using

Murnaghan equation). At the minimum E, the volume equivalent to the equilibrium volume (Ω^0) and P is zero. B can be obtained by calculating the second derivative of the plot.

DFT approaches have been used to elucidate the many phenomena in materials, such as phase transitions under pressure, thermal properties (by using the quantum molecular dynamics (QMD) method, atomic diffusion, defects in materials, surface or interface studies, etc. [86, 72, 78].

On the contrary, there are some limitations of using DFT calculations. For example, they cannot be used for studying excited states. Calculated band gaps in semiconductors and insulators are always underestimated. However better band gaps can be elucidated by using hybrid functionals. LDA approach usually provides large cohesive energies leading smaller lattice parameters and higher bulk moduli. Although it provides the better results in most cases, GGA was developed for solving the over binding problem in LDA method by including the local variations of electron densities. In some cases, the GGA method presents overcorrection and results in an underbinding issue. Another example is that GGA fails to estimate the strength of hydrogen bonds, which is better determined by using the hybrid functional methods. The van-der-Walls interactions are not included in the DFT approach. At the present, DFT calculations can be performed very fast for tens of atoms and their capability is usually up to a few hundred of atoms for regular calculations [78, 86, 72].

The details of some approaches used in this study are explained in the following sections.

2.3.2 Ground state electronic properties

Electronic properties at the ground state can explain the bonding and characteristic of structures. The DFT calculations can be used for determining the density of

states (DOSs), electronic charge density, and Electron Localization Function (ELF) properties in the materials. The meaning of ELF property and its application is explained more in this section. ELF was first proposed by Becke and Edgecombe [87]. ELF is originally defined by the probability density to find the second like-spin electron near the reference location. According to its magnitude of 0 to 1, it can verify the strength of repulsion between two electrons having same spin. In the other words, ELF can measure the same-spin pair density. The ELF is a useful tool to distinguish chemical bonding types in solids, such as metallic, covalent, and ionic bonds. ELF analysis has been used for identifying type of bonding [88, 89]. The bonding type can be classified by the topology and magnitude of ELF. ELF analysis of a given valence region informs about bonding in that region as they concern only on the bonding electrons of the relevant valence shell. By definition, the ELF value is 0.5 represented an electron gas, it closes to 1.0 for paired electron in covalent bond and unpaired electron in a dangling bond [90]. However, the ELF values lower than 0.5 cannot be defined evidently.

2.3.3 Lattice Dynamic properties

The lattice dynamic or phonon properties can be derived from the relation between forces and displacements of atoms in the crystals expressed via the force constant matrix. In general, there are two methods used to calculate these properties in crystals, which are the linear response [91] and the direct methods [92]. The direct method, sometimes called the supercell method, was used in this study. Theoretical background of this direct method is briefly explained in this section.

In a crystal, the potential energy (V) can be written in terms of the position of atomic nuclei:

$$V = V(..., R(n, \mu), ..., R(m, \nu), ...) \tag{2.15}$$

where n and m are the lattice sites, and μ and ν are the primitive unit cell n and m, respectively. In harmonic approximation, the expansion of this potential energy in terms of displacements, $u(n,\mu) = R(n,\mu) - R^0(n,\mu)$:

$$V = V(..., R^0(n,\mu), ...) + \frac{1}{2} \sum_{n,\mu,m,\nu} \phi(n,\mu;m,\nu) u(n,\mu) u(m,\nu) \tag{2.16}$$

$R^0(n,\mu)$ is the position at the minimum of the potential energy. The first term is the athermal crystal ground-state energy. The 3×3 matrix of force constant connecting atoms (n,μ) and (m,ν) can be defined as:

$$\phi(n,\mu;m,\nu) = \frac{\partial^2 V}{\partial R(n,\mu) \partial R(m,\nu)} \tag{2.17}$$

For the direct method, the periodic boundary conditions of the super cell are applied. The force $F(n,\mu)$ of the super cell is

$$F(n,\mu) = - \sum_{(m,\nu) \in SC} \phi^{(SC)}(n,\mu;m,\nu) \cdot u(m,\nu) \tag{2.18}$$

where $\phi^{(SC)}$ stands for the supercell force constant. Next, the eigenvalue problem can be applied to the phonon frequencies (k,j) as the following equation:

$$\omega^2(k,j) E(k,j) = D(k) E(k,j) \tag{2.19}$$

where k is the wave vector, and j are the phonon branches. $E(k,j)$ and $D(k)$ terms are the polarization vector and the dynamical matrix, respectively. For the supercell,

its dynamical matrix can be expressed in term of the force constant as

$$D^{SC}(k;\mu\nu) = \frac{1}{\sqrt{M_\mu M_\nu}} \sum_{m \in SC} \phi^{(SC)}(0,\mu;m,\nu) \times \exp\{-2\pi i k \cdot [R(0,\mu) - R(m,\nu)]\} \tag{2.20}$$

The atom (0,μ) locates at the center of the supercell, and M represents mass of each displacive particle.

In the direct force constant method, each unequivalent atom is displaced from its ordinary position. The forces constant matrix can be derived from the Hellmann-Feynman (HF) forces acting on atoms in the supercell. The fourier transformation of the forced constants represents in term of the dynamical matrix. Finally, the phonon dispersion and the phonon density of states (DOSs) can be obtained from the force constant calculations. The thermodynamic properties, such as free energy, heat capacity and thermal expansion coefficient, can be calculated from the phonon DOSs by using statistical mechanics [93, 94].

3. POLYMORPHIC PHASE TRANSITION IN MG/NB MULTILAYERS AT AMBIENT PRESSURE*

The goal of this study is to investigate the polymorphic phase transition in Mg/Nb multilayers by using theoretical methods. First, the concept of classical thermodynamics was applied for understanding the phase stability in Mg/Nb multilayered thin films. The so-called bi-phase diagram of Mg/Nb multilayers was constructed for predicting the phase change as a function of thickness and a volume fraction of constituent element. Next, the deeper investigation of the stabilized metastable bcc Mg phase was further performed by calculating the lattice dynamics, the electronic density of states (e-DOS), and the mechanical properties of bcc Mg. Moreover, Burgers' transformation, which is one of possible bcc-hcp transformation paths, was studied in the last section.

3.1 Introduction: polymorphic phase transition in thin films

On the basis of the underlying thermodynamic constraints, phase stability of constituents in metallic multilayer thin films can be markedly different from the stability of the same material in bulk form [95]. In the absence of size effects, metastable (and even unstable) phases can only be stabilized in bulk form under further constraints, such as elevated-pressures and temperatures. On the other hand, interfacial effects resulting from the growth of nanolayer systems has been shown to stabilize these metastable phases under ambient conditions, albeit under coherency constraints arising from the epitaxial growth of these films. The stabilization of these so-called

*Part of this chapter is reprinted with permission from "Stabilization of bcc Mg in thin films at ambient pressure: experimental evidence and *ab initio* calculations" by A. Junkaew, B. Ham, X. Zhang, A. Talapatra and R. Arróyave. *Materials Research Letters*, 1(3):161-167, 2013, Copyright by Taylor & Francis, available online at: http://www.tandfonline.com/10.1080/21663831.2013.804218.

pseudomorphic phases results from the competition between bulk and interfacial contributions to the free energies of the multilayer systems [96].

Over the past decades, the stabilization of metastable phases has been observed in nanolayer thin films consisting of at least two layers of dissimilar materials. For example, the metastable face-center-cubic (fcc) structure of Ti was observed in Ti/Ag thin films[97], Ti/Al multilayers [98, 99], and Ti thin films on a (100) Si substrate [100]. The metastable tetragonal Ta phase was formed in Ta/Cu multilayers [101]. The metastable rhombohedral Fe phase was observed in the Fe/Sb multilayers [102]. Examples of stabilization are not limited to metastable phases. In fact, thin film conditions have been shown to stabilize structures that are mechanically unstable under bulk conditions. For example, bcc Zr has been shown to be stable in Nb/Zr multilayers [103, 104]. Although, bulk bcc Zr is dynamically unstable, with the high-symmetry phonon branch [$\xi\xi\xi$] (with $\xi = 23$) exhibiting pronounced softening at low temperatures. The displacement pattern generated by this phonon mode corresponds to the $bcc \rightarrow \omega$ transformation [105]. The epitaxial conditions arising from the growth of Zr on Nb suppresses this unstable mode and stabilizes the bcc structure. Similarly, the fcc Nb structure has been observed to become stable in Cu/Nb multilayers [106]. Many studies reported the formation of the unstable bcc Co or the metastable hcp Cr in Co/Cr multilayers [107, 108, 109].

3.2 Polymorphic phase transition in Mg/Nb multilayers

3.2.1 Experimental observation of metastable bcc Mg phase

Magnesium (Mg) itself is one of the most attractive metals for the aerospace and automotive industries due to its high specific strength [110]. Under ambient conditions, bulk Mg exists in the hexagonal close packed (hcp) crystal structure, which has limited ductility due to the reduced number of active slip systems at room

temperature [110]. In bulk systems, alloying with cubic elements can be used to stabilize Mg-based cubic solid solutions. Unfortunately, Mg either forms miscibility gaps or numerous intermetallic compounds when alloyed with cubic elements. A notable exception is the Mg-Li system, in which an fcc solid solution is stabilized with only 30 at.% Li[110, 111, 112].

Under non-bulk thermodynamic constraints (i. e. in thin film or nano-structures), phase stability can be modified through the introduction of coherency constraints [113] and it is likely that Mg-based solid solutions with a wider range of alloying elements can be stabilized. Recent work aimed at improving the limited hydrogen storage properties of Mg-based systems by Tan *et al.* [114] has shown that it is possible to stabilize a bcc Mg-based solid solution with the addition of 25 at.% Nb in co-sputtered thin films.

Although theoretical and experimental work shows that Mg can be stabilized in fcc and bcc structures (under bulk and thin-film conditions) through alloying, pure Mg in the bcc structure has only been stabilized at extremely high pressures ($\sim$50 GPa) in the work reported by Olijnyk *et al.* [115]. In fact, bcc Mg turns out to be dynamically unstable under normal conditions, as will be discussed below. The phase diagram and phase transformation of Mg have been investigated by others [116, 117], but these studies have been limited to the stable bulk phases.

Recently, Ham and Zhang [118] showed that bcc Mg can be stabilized in Mg/Nb thin-film multilayers under ambient conditions. These results *may constitute the first instance of experimental evidence showing that it is possible to stabilize pure bcc Mg under ambient temperature/pressure conditions.* Mg/Nb multilayers with a thickness of a few nanometers have a much higher mechanical strength compared to bulk Mg[118] and much better hydrogenation performance compared to bulk Mg [119].

As an example, a high resolution transmission electron microscopy (HRTEM)

image of the interface in Mg/Nb 5 nm multilayers in Fig. 3.1(a) shows an occurrence of bcc Mg in the region close to the interface along with Nb. bcc Mg grows epitaxially on top of Nb, as confirmed by the Fast Fourier Transform (FFT) of the high resolution image in Fig. 3.1(b). The X-ray diffraction (XRD) pattern in Fig. 3.1(c) shows the major peak to be located at the Nb(110) position. Superlattice peaks are observed on the shoulder of the Nb peak. The signal for hcp-Mg (0002) is weak and overlaps with a satellite peak due to the formation of bcc Mg near the Nb layer interface.

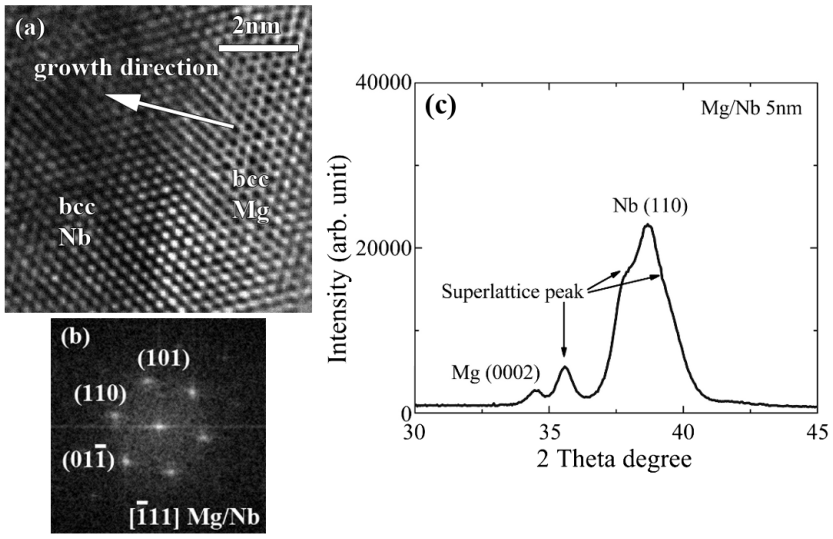

Figure 3.1: (a) HRTEM micrograph of Mg/Nb 5 nm multilayers showing the interface between Mg and Nb. Mg with bcc phase has grown epitaxially on Nb. (b) The FFT of Mg and Nb confirms the epitaxial relation between bcc Mg and Nb. (c) The XRD pattern of the specimen. [120]

In this work, theoretical studies were used for understanding this phenomenon in Mg/Nb multilayers.

3.2.2 A phase stability analysis by classical thermodynamic approach

3.2.2.1 Classical thermodynamic approach

In the past decades, there have been significant efforts to investigate the effect of epitaxial constraints on the phase stability of alloys. Zunger and collaborators [121, 122, 123], for example, have considered the effect of epitaxial constraints by constraining the lattice parameters of the alloy system along the epitaxial plane and have used cluster expansion techniques to predict theoretical phase diagrams of alloy systems. The theory considers long-range elastic interactions resulting from biaxially deforming a structure from its own ground state lattice parameters on the plane of the substrate. Formally, they used a mixed basis approach through the use of the so-called Constituent Strain Energy (CSE) in which the long-range elastic interactions are defined in reciprocal space, while the chemical configurational contributions are treated in the real space. This approach has already yielded important theoretical results, such as the stabilization of solid solutions—and even ordered phases—in systems, such as (In,Ga)N [122], that in the bulk state exhibit phase separation behavior.

While *ab-initio* based microscopic approaches have been shown to be very powerful to investigate the effect of small scales (and coherency) on the phase stability of systems, other approaches based on classical (continuum) thermodynamic approaches have been shown to be rather useful. The so-called nano-CALPHAD (CALculation of PHAse Diagram) approach [124] proposes to use the number of atoms in the system as another thermodynamic variable. This approach results in the re-definition of thermodynamic concepts, such as the Gibbs phase rule, tie-lines, etc. Perhaps one of the salient aspects of this recent work is the realization that concepts used in bulk thermodynamics are sometimes not adequate to represent equilibria (i.e. phase

diagrams) in nano-systems.

In the very specific case of nanolayer films, a formalism to understand the phase stability observed in experiments was developed by Dregia *et al.* [95]. Classical thermodynamics was applied to systematically understand equilibria in metallic multilayers. Specifically, the unit bilayer consisting of component A and B in their strain-free, stable crystal structures, is a reference state. Two independent thermodynamic degrees of freedom are used to completely define a thermodynamic state. The first degree of freedom is the bilayer thickness (λ), which is defined as the summation of the thicknesses of the individual component layers A and B ($\lambda = h_A + h_B$). The other degree of freedom corresponds to the overall composition of the bilayer and this is expressed in terms of the volume fractions of component A (f_A) and component B (f_B), satisfying $f_A + f_B = 1$. The free energy of the reference bilayer is denoted by G. If at least one of the components of the bilayer is transformed to a metastable (or unstable) structure, the total free energy of the bilayer system is G'.

$$G = N_A G_A + N_B G_B + 2\gamma S \tag{3.1}$$

$$G' = N_A G'_A + N_B G'_B + 2\gamma' S \tag{3.2}$$

where N_i and G_i are the number of atoms and chemical potential of species i ($i = A$ and B), respectively. S and γ stand for the area of interface and the interfacial energy, respectively. Assuming that the interface area between layers A and B is invariant during the transformation, the specific free energy of formation of the bilayer—normalized per interfacial area—, Δg, is given by:

$$\Delta g = 2\Delta\gamma + [\Delta G_A f_A + \Delta G_B f_B]\lambda \tag{3.3}$$

In this equation, $\Delta\gamma$ is the change in the interfacial energy upon transformation, ΔG_i is the allotropic free energy change (normalized per volume) of the reference component, i. Note that $\Delta\gamma$ is affected by chemical and structural interfacial effects and that ΔG_i may include not only the difference in the thermodynamic bulk free energies of the phases but also include other volume effects, such as those associated to strain energy.

If one considers that $1/\lambda$ and f_i are the thermodynamic degrees of freedom in the system, it is then possible to determine the thermodynamic state of the system as a function of $1/\lambda$ and f_i and encode the results in so-called bi-phase diagrams. In these diagrams, the transitions from different configurations in the A/B multilayers can be expressed in terms of so-called coexistence lines.

A simplification can be made if one assumes that $\Delta\gamma$ and ΔG_i are independent of the layer thickness. Along the coexistence lines, Δg is equal to zero, in an analogous fashion to the conditions for equilibrium for coexistence lines in single-component, multi-phase systems. From this condition, a (linear) function relating $1/\lambda$ and f_i can be derived. The slope and intercepts of each of the bi-phase boundary lines can be calculated from ΔG_i, $\Delta\gamma$, and the constrained coordinates (f_i,$1/\lambda$) such as the (0,0) and the (1,0) points. This approach was used to predict the bi-phase diagram of Co/Cr and Al/Ti multilayer thin-films and compared to experimental results. The stabilization of the metastable phases was described by the decreasing of the interfacial energy ($\Delta\gamma$)[95, 125].

Based on the pioneering work of Dregia *et al.* , there were some studies including the effect of coherency strains in the theoretical models. For example, Banerjee *et al.* investigated the pseudomorphic growth of fcc Ti in Ti/Al multilayers. The strain energy (W_{el}) term, which is derived from a biaxial elastic modulus (Y_i) and a coherency strain of component i (ϵ_i), is included into Eq. 3.3. The predicted bi-

phase diagram of Ti/Al multilayers compared well to experimental data. Thompson *et al.* studied the Nb/Zr multilayers [104] and proposed the bi-phase diagram by using the classical thermodynamic approach, including both coherency effect and the chemical component of the interfacial energy. For the structural component of $\Delta\gamma$, a misfit dislocation network model, evaluated from the Bollman's O-lattice [126] formalism, was used for a semi-coherent interface.

An alternative method for estimating the interfacial free energy is considering a liquid as a solid with a high concentration of dislocation cores. At melting point, a solid-solid interfacial energy (γ_{ss}) is shown to be approximately twice of the solid-liquid interfacial energy (γ_{sl}) [127, 128]. This concept was applied for estimating the first order approximation of γ_{ss} from mean values of both constituent substances in multilayers. It was used to approximate interfacial energies of various interfaces such as Cu/Mo, Cu/W, Ni/Mo, Ni/W, Cu/Ni and Mo/W systems, and approximated values provided a good agreement with other works [128]. Li *et al.* applied this method for estimating an incoherent interfacial free energy (γ_{inc}) expressed in Eq. 3.4 [96].

$$\gamma_{inc} \approx 2\gamma_{sl} = \frac{4\bar{d}\bar{S}_{vib}\bar{H}_m}{3\bar{V}_m R} \tag{3.4}$$

The properties present in Eq. 3.4 are mean values of both constituent elements. $\bar{S}_{vib}$ and $\bar{H}_m$ are the mean values of the vibrational melting entropy and the melting enthalpy, respectively. $\bar{d}$ and $\bar{V}_m$ denote the mean values of the atomic diameter and molar volume, respectively. The R is the ideal gas constant. In case of coherent or semi-coherent interfaces, γ_c is in turn obtained from $\gamma_c = Nu_d/S$. N and S denote the number of dislocations and the interfacial area between film and substrate. u_d defines the misfit energy of a single dislocation. This u_d can be derived for an edge dislocation without dislocation core energy presented in the following equation [129]:

$$u_d \approx \frac{\mu_A \mu_B b^2 l}{2\pi(\mu_A + \mu_B)(1+\nu)}[\ln \frac{\delta}{b} + 1] \tag{3.5}$$

where the Burger's vector $b = \bar{d}$ and l is the dislocation length. μ and ν are the shear modulus and the Poisson ratio, respectively. δ represent a half of the distance between two adjacent dislocations.

$$\frac{\delta}{\bar{d}} = \frac{d_A}{2|d_A - d_B|} \tag{3.6}$$

and the total number of dislocations on the interface is $N = S/\delta$. After substituting $\delta/\bar{d}$ and N into Eq. 3.5, γ_c can be found from:

$$\gamma_c = \frac{\mu_A \mu_B \bar{d}|d_A - d_B|}{\pi(\mu_A + \mu_B)(1+\nu)d_A}[\ln \frac{d_A}{2|d_A - d_B|} + 1] \tag{3.7}$$

The expressions for γ_{inc} and γ_c can be used to obtain the change in interfacial energy ($\Delta\gamma$) according the phase transformation in multilayers. Finally, taking into account the coexistence condition $\Delta g = 0$, one can obtain expressions for each slope of the boundary lines in a typical bi-phase diagram in which constituents A and B have different ground state crystal structures [96]. This approach was used for investigating the bi-phase diagrams of the Co/Cr, the Ti/Nb, the Zr/Nb and the Ti/Al multilayers [96] and it has recently been used to explain the observation of fcc Nb in Cu/Nb multilayers [106].

3.2.2.2 Theoretical procedure

Following the formalism by Dregia and Li [95, 96], the bi-phase diagram in Mg/Nb multilayers was predicted in this work. In Fig. 3.2, three zones of microstructures, which are consisted of hcp Mg/bcc Nb, bcc Mg/bcc Nb and hcp Mg/hcp Nb, are separated by three boundaries labelled by the Arabic number. In this paper, line(1)

to (3) are the boundary between hcp Mg/bcc Nb and bcc Mg/bcc Nb, the boundary between hcp Mg/hcp Nb and bcc Mg/bcc Nb, and the boundary between hcp Mg/bcc Nb and hcp Mg/hcp Nb, respectively. From Eq. 3.3, slopes (m) and constants (c) of three linear lines can be derived by setting $\Delta g = 0$.

For example, hcp Mg/bcc Nb $\rightarrow$ bcc Mg/bcc Nb transformation is considered for determining the boundary line (1). In this case, ΔG_{Nb} is zero, because Nb has the same bcc phase. A slope (m_1) and a constant (c_1) of line (1) are $\Delta G_{Mg}/2\Delta\gamma_1$ and $-\Delta G_{Mg}/2\Delta\gamma_1$, respectively. The free energy change of Mg (ΔG_{Mg}) can be calculated from $G_{Mg}^{bcc} - G_{Mg}^{hcp}$. The free energy of each phase was obtained from the thermodynamic data for the pure elements by SGTE (Scientific Group Thermodata Europe)[130], developed by the CALPHAD approach[131, 132]. $\Delta\gamma_1$, which is $\Delta\gamma_1$=$\gamma_{bcc/bcc}$-$\gamma_{hcp/bcc}$, denotes the interfacial energy difference between bcc Mg/bcc Nb and hcp Mg/bcc Nb interfaces. Details of the calculations of free energies from Calphad method are given in Appendix A. Slopes and constants of other two lines can be elucidated by using the same procedure. Eq. 3.4 was used for calculating $\gamma_{hcp/bcc}$ of hcp Mg/bcc Nb interface. $\gamma_{bcc/bcc}$ of bcc Mg/bcc Nb interface and $\gamma_{hcp/hcp}$ of hcp Mg/hcp Nb interface were estimated by using Eq. 3.7.

Parameters of hcp Mg and bcc Nb used in the calculations are given in Table 3.1. The atomic diameters of atoms in metastable phases are obtained from the Goldschmidt premise [133]. When the coordination number of the lattice is changed from 8 in bcc to 12 in hcp, the atomic diameter contracts by 3%, and vice versa. Gibbs free energies (G) of Mg and Nb structures were calculated at 298.15 K and reported in Table 3.2. The calculated γ value of each type of interfaces are shown in Table 3.2.

Table 3.1: Properties of hcp Mg and bcc Nb

Properties	Mg	Nb
d (Å)^a	3.20	2.86
T_m (K)^a	922	2740
H_m (kJ/mol)^a	8.7	26.4
V_m (cm^3/mol)^a	14.0	10.9
ΔS_{vib} (J/mol·K)^a	7.73	8.15
μ (GPa)^b	17.3	37.7
ν ^{b}	0.29	0.39

^{a} Ref. [134], ^{b} Ref. [135]

3.2.2.3 Pridicted bi-phase diagram of Mg/Nb multilayers

As a result, the predicted bi-phase diagram is illustrated in Fig. 3.2. Three regions, which are hcp Mg/bcc Nb (green), bcc Mg/bcc Nb (blue) and hcp Mg/hcp Nb (red) phases, are separated by three boundary lines. The pseudomorphic growth of the bcc Mg and hcp Nb phases can be indicated at the particular bilayer thickness and f_{Nb} values. The triple point, which consisted of all three phases, is located at $f_{Nb} = 0.15$ and $1/\lambda = 0.29\ nm^{-1}$ or at the bilayer thickness of 3.5 nm.

3.2.2.4 Experimental validation

To verify the predicted bi-phase diagram, additional experiments were performed by B. Ham and X. Zhang. Mg/Nb multilayers with different layer thickness were deposited by DC magnetron sputtering at room temperature onto Si (100) substrates with 1 μm thermal oxides. The base pressure of the sputter chamber was around 5×10^{-8} Torr before the deposition. Mg and Nb targets, with 99.99% purity, were used. The films were deposited under $\backsim$2.5 mTorr UHP Argon. The deposition rates for Mg and Nb were $\backsim$2 and $\backsim$0.5 nm/s, respectively. Transmission electron microscopy (TEM) specimens were prepared by grinding, polishing and finished by low energy

Table 3.2: Calculated interfacial energy (γ) and the allotropic free energy per unit volume (G) of Mg and Nb

Properties	Calculated valued
γ (J/m^2)	
$\gamma_{hcp/bcc}$	0.544
$\gamma_{bcc/bcc}$	0.284
$\gamma_{hcp/hcp}$	0.285
G at 298.15 K (J/m^3)	
G^{hcp}_{Mg}	-6.96×10^8
G^{bcc}_{Mg}	-5.20×10^8
G^{bcc}_{Nb}	-9.98×10^8
G^{hcp}_{Nb}	-9.07×10^6

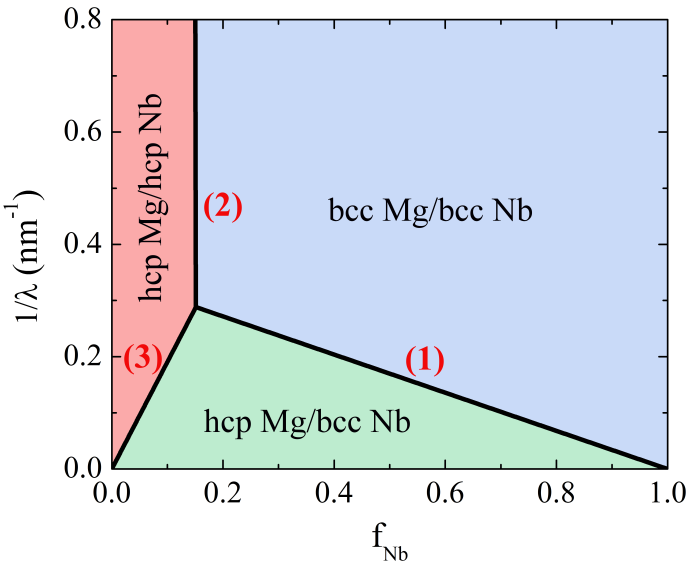

Figure 3.2: The predicted diagram of Mg/Nb multilayers is plotted as a function of $1/\lambda$ and f_{Nb}.

ion milling. TEM was performed using a JEOL 2010 microscope operated at 200 kV. XRD experiment was performed on a Bruker-AXS D8-focus BraggBrentano X-ray diffractometer.

Since metastable bcc Mg and hcp Nb cannot be observed in bulk systems, at ambient conditions. DFT methods provided a good agreement of lattice parameters of their stable lattices, which are hcp Mg and bcc Nb [120]. Therefore, the lattice parameters of hcp and bcc forms of Mg and Nb were calculated by using DFT calculations. The generalized gradient approximation (GGA-PW91) [136] with projector augmented-wave (PAW) pseudo-potentials [82], implemented in the Vienna *ab initio* simulation package (VASP) [137], was used. A self-consistency convergence criterion of 10^{-6} eV and the plane-wave cut-off of 520 eV were used. Monkhorst-Pack grids used for hcp and bcc structures are $18 \times 18 \times 11$ and $18 \times 18 \times 18$, respectively. The 2θ values of these optimized structures were predicted by using Powder Cell software [138] and used as the reference values shown in Fig. 3.4.

The predicted bi-phase diagram was validated by selecting specimens from three different zones in Fig. 3.2. As the results show, the formation of metastable phases in Mg/Nb multilayers was observed in HRTEM micrographs. For the first example, Mg 1.5 nm/Nb 0.5 nm multilayers shown in Fig. 3.3(a) shows that metastable bcc Mg structure formed and the interface was coherent between bcc Mg and Nb. This is consistent with the prediction based on the calculated bi-phase diagram. Mg appears to grow epitaxially on Nb as confirmed by the inserted fast fourier transforms (FFTs) of the image examined along Nb $[\bar{1}11]$ zone axis. Also the layer interface was chemically-abrupt. In the second case, HRTEM micrograph of Mg 1.8 nm/Nb 0.2 nm multilayers (Fig. 3.3(b)) shows that hcp Nb has grown epitaxially on hcp Mg. The orientation of crystals was confirmed by the inserted FFT of the micrograph examined along hcp $[2\bar{1}\bar{1}0]$ zone axis. HRTEM micrograph and FFT patterns of Mg

5 nm/Nb 5 nm multilayers shown in (Fig. 3.3(c)) explain growth of bcc Nb on hcp Mg.

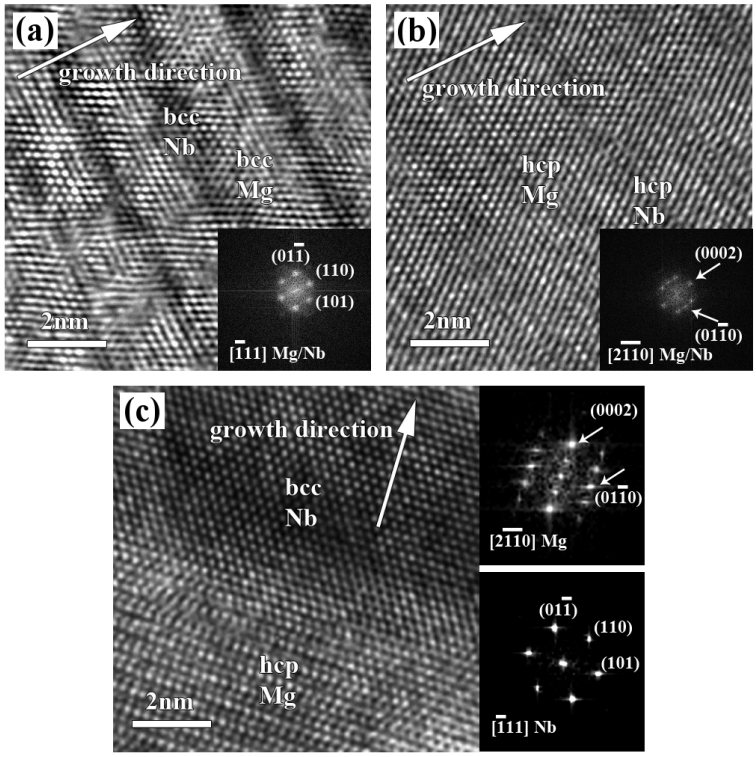

Figure 3.3: (a) High resolution TEM image and corresponding fast Fourier transform (FFT) pattern of Mg 1.5 nm/Nb 0.5 nm multilayers, (b) HRTEM micrograph of Mg 1.8 nm/Nb 0.2 nm multilayers and correlated FFT pattern, and (c) HRTEM micrograph of Mg 5 nm/Nb 5 nm multilayers and correlated FFT patterns in Mg and Nb

Fig. 3.4 shows XRD profiles of representative specimens from three different regions in the bi-phase diagram. The dashed vertical lines represent the reference 2θ values of hcp Mg (a=3.2Å and c=5.19Å), bcc Mg (a=3.57Å), bcc Nb (a=3.32Å) and hcp Nb (a=2.88Å and c=5.26Å) obtained from DFT calculations. Mg 11.58nm/Nb

0.42nm multilayers (Fig. 3.4(a)) shows fully coherent Mg and Nb hcp structure. Mg 1.8nm/Nb 0.2nm nanolayers (Fig. 3.4(b)) indicates that Mg lattice is slightly distorted and a small bcc Nb peak is observed. However, coherent hcp Mg and hcp Nb peaks are dominant. As the fraction of Nb in the bilayer increases, a major Mg with coherent Nb peak shifts toward the bcc Mg position. The predominant peak in Mg 1.5nm/Nb 0.5nm multilayers (Fig. 3.4(c)) shifted from hcp to bcc Mg position and bcc Nb peak with higher intensity than Fig. 3.4(b) specimen is also shown. However the hcp Nb peak is still observed indicating a small fraction of hcp lattice exists. These three specimens correspond to the Mg-rich region of the phase diagram. Instead of aligning epitaxially with bcc Nb, hcp Mg is distorted towards bcc Mg's lattice parameter in Fig. 3.4(b) and (c). For the same bilayer thickness, changing of volume ratio of components has an effect on the magnitude of distortion from the hcp to bcc structures.

In order to achieve a better understanding of the experiments, the predicted bi-phase diagram is replotted as the function of f_{Nb} and λ and illustrated in Fig. 3.5. The experimental points are compared in this figure. The expanded boundary lines corresponds to the distorted structures observed in the experimental results. As Nb is much stronger than Mg, metastable bcc Mg can be stabilized under thin films with the small ratio of Nb thickness ($f_{Nb} \sim 0.15$). On the other hand, metastable hcp Nb phase can be observed in the region in which the volume fraction of Nb is low with a few layer thick and larger fraction of Mg thick. For larger λ, increasing of f_{Nb} is required for stabilizing bcc Mg phase and vice versa in case of hcp Nb. Likewise, the interfacial energy has less contribution to the free energy of the system when the thickness increases. The experimental data agrees well with the predicted bi-phase diagram and shows that the coexistence of otherwise metastable interfaces can be explained in great part by the competition between chemical free energy differences

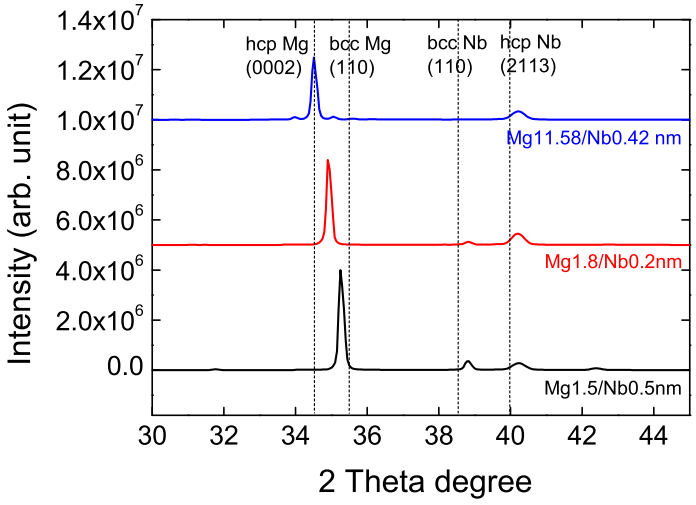

Figure 3.4: XRD profiles of three representative specimens from different regions of the bi-phase diagram. (a) the Mg 11.58nm/Nb 0.42nm multilayers, (b) the Mg 1.8nm/Nb 0.2nm multilayers, and (c) the Mg 1.5nm/Nb 0.5nm multilayers

between stable and metastable (unstable) phases and simple models to calculate differences in interfacial energies.

3.2.3 Stabilization of metastable bcc Mg phase studied by DFT calculations

Stimulated by the experimental observation, this section attempts to further elucidate the apparent (meta)stability of bcc Mg through *ab initio* calculations at 0K. While this section focuses exclusively on the particular case of epitaxially grown Mg/Nb multilayers, this research can provide more general insight into the stabilization of bcc Mg in nano-structured alloy systems.

3.2.3.1 Computational procedure

To theoretically investigate the stability of bcc Mg in multi-layered Mg/Nb thin films, we performed DFT calculations based on pseudo-potentials as implemented

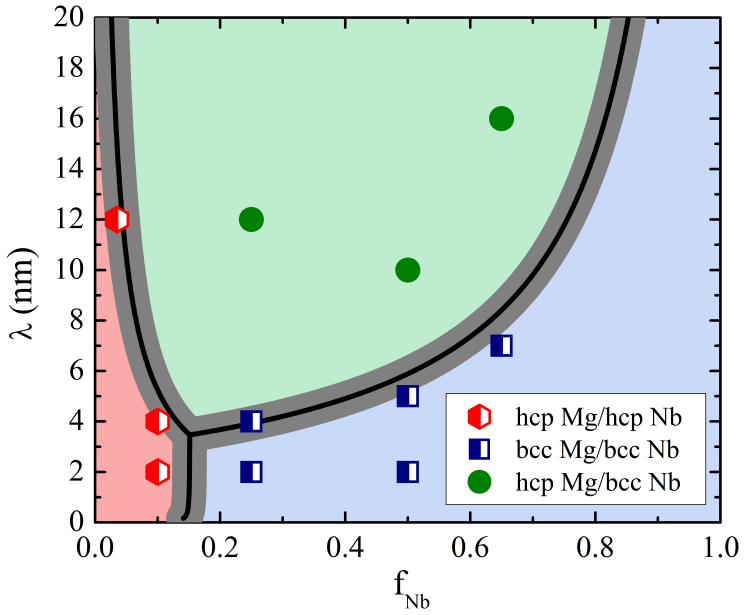

Figure 3.5: Comparison of the predicted diagram of Mg/Nb multilayers and experimental results. The bi-phase diagram are plotted as a function of λ and f_{Nb}. The experimental results are represented by points.

in VASP [137, 139]. The generalized gradient approximation (GGA-PW91) [136], with projector augmented-wave(PAW) pseudo-potentials[82] was used—blue In the Supplementary Material section it is shown that the particular choice of exchange correlation approximation used (GGA, LDA, PBE) does not have significant effect on the results. Convergence of the electronic structure was assumed when changes between two consecutive electronic steps fell below 10^{-7}eV. During the optimization stage of the calculations, Monkhorst-Pack grids of $18 \times 18 \times 11$ and $18 \times 18 \times 18$ were used for hcp- and bcc-structures, respectively. The lattice dynamics of bcc Mg were calculated by using the direct force constant method implemented in the PHONON code [94]. The supercell consisted of 54 atoms with an atomic displace-

ment of ±0.05Å. The chosen atomic displacement corresponds to approximately 2% of the interatomic distance in the structure and allows the accurate calculation of interatomic forces without necessarily sampling the anharmonic regime of the crystal potential. The force constant calculations were performed using VASP. A plane wave cut-off energy of 520 eV and Monkhorst-Pack grids of $10 \times 10 \times 10$ were used to guarantee good convergence in the interatomic forces. For the Burgers transformation calculations, Monkhorst-Pack grids of $17 \times 17 \times 11$ were used. The calculations correspond to 0 K. However, since the temperatures of the films correspond to approximately 30% of the melting point of Mg anharmonic effects are not expected to be important.

3.2.3.2 Thermodynamic Stability

The optimized structural parameters and formation enthalpies of the structures mentioned above are reported in Table 3.3. The formation enthalpy (ΔH) was calculated by using the element in the gas phase as the reference state. The calculated ΔH of hcp Mg is higher than the experimental value by about 2%. Moreover, the stability of simulated Mg crystals can be evaluated by comparing their ΔH values. In hcp Mg, the calculated lattice constants show good agreement with previous work [140]. ΔH of hcp Mg is lower (more negative) than both types of bcc Mg. This implies that Mg is more stable in the hcp phase. The simulation shows that if relaxation is allowed, both types of constrained bcc Mg (grown epitaxially on bcc Nb with a = 2.953 Å and pressurized bulk with a = 2.953 Å) will relax to a lattice parameter of 3.571 Å. On the other hand, bcc Mg relaxes to an atomic volume similar to that calculated for hcp Mg (∼23 Å^3). This relaxed structure corresponds to the (unstable) equilibrium bcc Mg structure at 0 K.

Table 3.3: Formation enthalpies (ΔH) and calculated lattice parameters of hcp Mg, bcc Mg and bcc Nb

Structure	ΔH	Lattice Parameter (Å)	
	(kJ/mol)	Calculation	References
hcp Mg			
full relaxation	-142.6	a=3.198	a=3.22
	(-145.90 ± 0.80)[c]	(c/a=1.621)	(c/a=1.624)[d]
bcc Mg			
full relaxation	-139.7	a=3.571	a=3.571[e]
constraint	-22.2	a=2.953	a=2.9530±0.002[a]
(high pressured lattice parameter)[a]			
constraint	-126.1	a=3.324	
(lattice coherency with bcc Nb)[b]			
bcc Nb			
full relaxation	-677.0	a=3.324	a=3.300[f]

[a]lattice parameter corresponds to the experimental lattice parameter determined experimentally at 50 GPa [115].
[b]bcc Mg with a = 3.324 $\mathring{A}$ was observed experimentally as Mg grew epitaxially on Nb.
[c][141], [d][142], [e][143], [f][144]

3.2.3.3 Lattice dynamics (Phonon) calculations

Further investigation of the effects of lattice parameter on the stabilization of bcc Mg was done by examining the lattice dynamical properties of bcc Mg at multiple lattice parameters. The phonon dispersion relations in the bcc Mg phase were investigated by using the direct force constant method. Three forms of bcc Mg were considered: fully relaxed bcc Mg (a=3.571 Å), bcc Mg with the lattice parameter of bcc Nb (a=3.324 Å) and bcc Mg under high pressure with a lattice parameter of 2.953 Å [115]. Fig. 3.6(a) shows the phonon dispersion relations along selected symmetry directions N [12,0,0] $\rightarrow$ Γ [0,0,0] $\rightarrow$ H [12,12,-12]$\rightarrow$ P [14,14,14] $\rightarrow$ Γ [0,0,0] for the three bcc structures. Since the primitive cell of bcc Mg consists of a

single atom, there are only acoustic branches in the dispersion curve.

The figure clearly shows that the fully relaxed bcc Mg structure shows negative (imaginary) frequencies along the $\Gamma - N$ direction in the Brillouin zone. This instability in the phonon structure indicates that this crystal is actually mechanically unstable: any distortion along the directions corresponding to the unstable (imaginary) phonon modes results in a spontaneous transformation to a dynamically stable state of lower energy (hcp, for example). Remarkably, Fig. 3.6(a) shows that these unstable modes are not observed in the constrained bcc Mg with a lattice parameter corresponding to bcc Nb. The phonon branches are even harder (higher frequencies) for the bcc Mg structure corresponding to high pressure experiments. This indicates that the softening of the transverse acoustic (TA) branch tends to disappear as the lattice parameter of the structure decreases. This hardening of the phonon branches is consistent with the observed stabilization of bcc Mg in regions close to the Mg/Nb interfaces.

We also notice that even though ΔH of both types of constrained bcc Mg is greater than that of fully-relaxed bcc Mg, the (compressed) metastable structures can be stabilized under the following specific conditions: either high hydrostatic pressure or constraints arising from interfacial interactions between Nb and Mg. In fact, interfacial and other thermodynamic effects important in nano-scale systems can promote the stabilization of metastable phases in thin films [95, 104, 113].

Further insight into the stabilization of bcc Mg can be derived by studying the evolution of the phonon dispersion with lattice parameter, varying from that corresponding to the fully-relaxed bcc Mg 3.571 Å(a_0, V_0=22.769 Å^3/atom) to bcc Mg with the lattice parameter of Nb 3.324 Å($0.931a_0$, V=18.363 Å^3/atom). The phonon dispersion curves of bcc Mg with varied lattice constants were calculated using the PHONON code.

The gradual dynamic stabilization of bcc Mg can be observed as the lattice constant deceases. In fact, Fig. 3.6(b) shows that the unstable transverse acoustic (TA) mode vanishes with a decrease of 2%-3.4% in the lattice parameter. The appearance of these soft modes agrees well with previous work[145]. The softening of the TA mode along the $\Gamma - N$ direction, represented by $[\xi, \xi, 0]$, indicates an instability along $[1\bar{1}0]$ planes. The softening of this phonon branch has been deemed responsible for structural transformations of bcc metals [146, 147]. It should be noted that the calculated tetragonal shear constant $C' = (C_{11} - C_{12})/2$ for the fully relaxed bcc Mg structure is very close to zero ($\sim$2 GPa) and those very close to the Born stability limit [148, 149]. The detail will be explained in the following section.

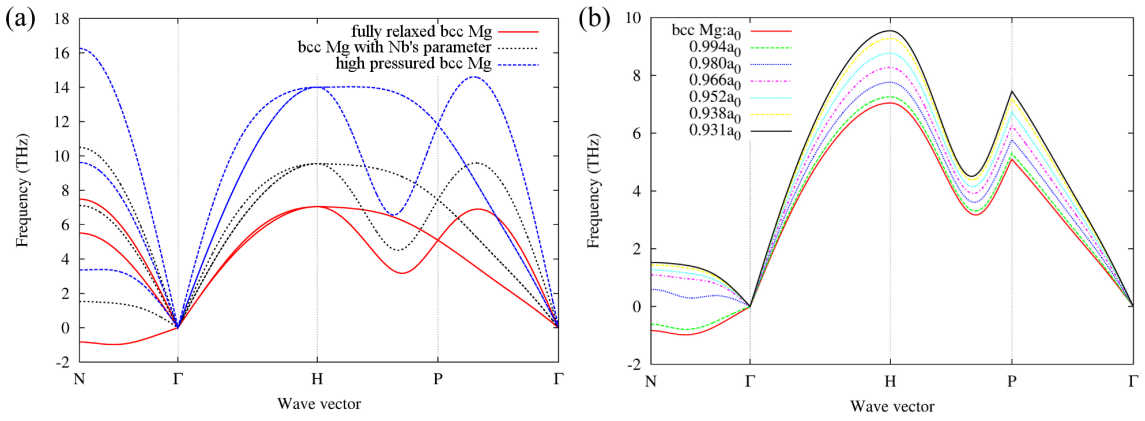

Figure 3.6: Phonon dispersion curves along the symmetry directions (a) comparison of calculated phonon dispersion relations of fully relaxed bcc Mg, bcc Mg with bcc Nb's lattice parameter and high pressured bcc Mg (b) comparison of acoustic branches of varied lattice para-meters (frequency in THz versus wave vector in arbitrary units).

3.2.3.4 Comparison of the mechanical properties as a function of volume in bcc Mg

The elastic stiffness constants (C_{ij}) have been calculated based on the stress-strain method [150]. Elastic constants (C_{ij}) as a function of atomic volume of bcc Mg are compared in Fig. 3.7(a). For a cubic lattice, elastic stability can be explained by a $(C_{11} - C_{12})/2$ value [148, 149]. In Fig. 3.7(a), bcc Mg lattices are more mechanically unstable, which are indicated by decreasing in $(C_{11} - C_{12})/2$ values, when their atomic volume increases. The fully relaxed bcc Mg has a low $(C_{11} - C_{12})/2$ ($\sim$ 2.5 GPa).

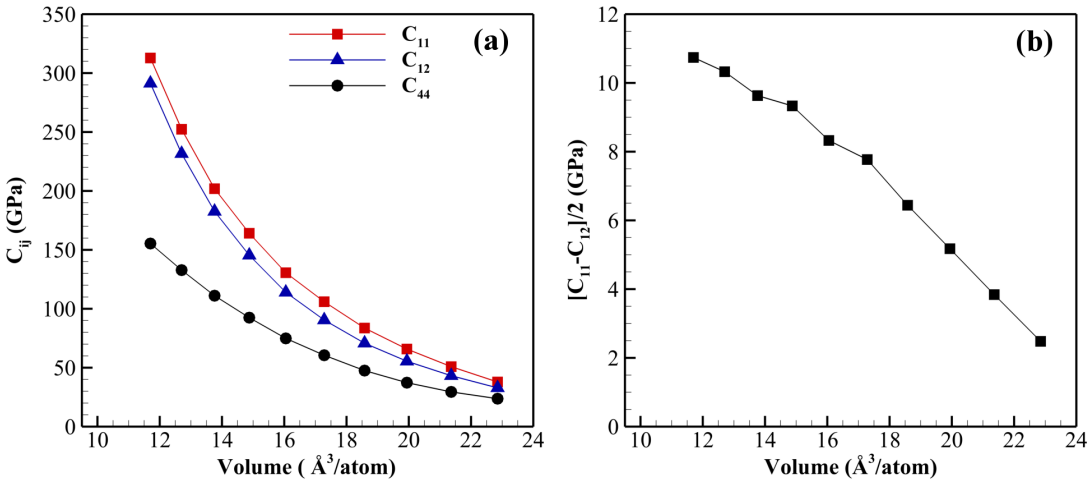

Figure 3.7: (a) Elastic constants (C_{ij}) as a function of atomic volume of bcc Mg and (b) $(C_{11} - C_{12})/2$ as a function of atomic volume of bcc Mg

3.2.3.5 Electronic Density of States (e-DOS)

In this section, the electronic structure of Mg crystals is studied by analyzing the e-DOS. Total and partial e-DOS plots of hcp Mg, relaxed bcc Mg, bcc Mg with bcc Nb's lattice parameter and bcc Mg under high pressure are presented in Fig. 3.8(a)- 3.8(d), respectively. The figure shows that all structures exhibit metallic-

Table 3.4: Elastic constants (C_{ij}) in GPa of Mg structures calculated by using PAW-GGA(PW91) method

Structure	C_{11}	C_{12}	C_{13}	C_{33}	C_{44}	C_{66}
bcc Mg						
full relaxation	38.07	33.07			23.77	
hcp Mg						
Calculation	72.70	18.99	17.88	69.54	17.83	26.86
Exp. (0K)[151][a]	63.48	25.94	21.70	66.45	18.42	18.75
Exp. (298K)[151]	59.43	25.60	21.40	61.64	16.42	16.91

[a]The extrapolated values from an experiment performed by using an ultrasonic pulse technique[151]

type bonding with occupied states at the Fermi level. For the hcp Mg crystal, the calculated e-DOS is in agreement with previous studies [152, 153]. DOS plots of bcc Mg with decreasing cell volume are shown in Fig. 3.8(b) to 3.8(d), respectively. Smaller bcc unit cell leads to a shifting of the Fermi energy level (E_F) to higher energies and qualitative changes in the e-DOS close to E_F. Decreasing the volume of the bcc Mg cell leads to a reduction in the number of electronic states (at E_F) and the local maximum—which is an indication of instability—in the e-DOS at the Fermi level observed in the fully relaxed bcc Mg (Fig. 3.8(b)) no longer appears as the volume decreases. These changes are also correlated to a larger partial e-DOS in the p-channels at the expense of the s-states at energies close to E_F. In fact, close inspection of Fig. 3.8 suggests that s-states in a bcc-like environment make the structure unstable and it is the slight dominance—most evident at the smallest lattice parameter considered—of p-states with decreased volume which stabilizes the bcc structure. The (slight) predominance of p-states at E_F can also be observed in fully relaxed hcp Mg (Fig. 3.8(a)). Moriarty *et al.* suggested that decreasing the

atomic distance in compressed bcc Mg can result in lowering and partial filling of empty 3d bands, which in the end results in stronger interatomic bonds and a more stable structure [154].

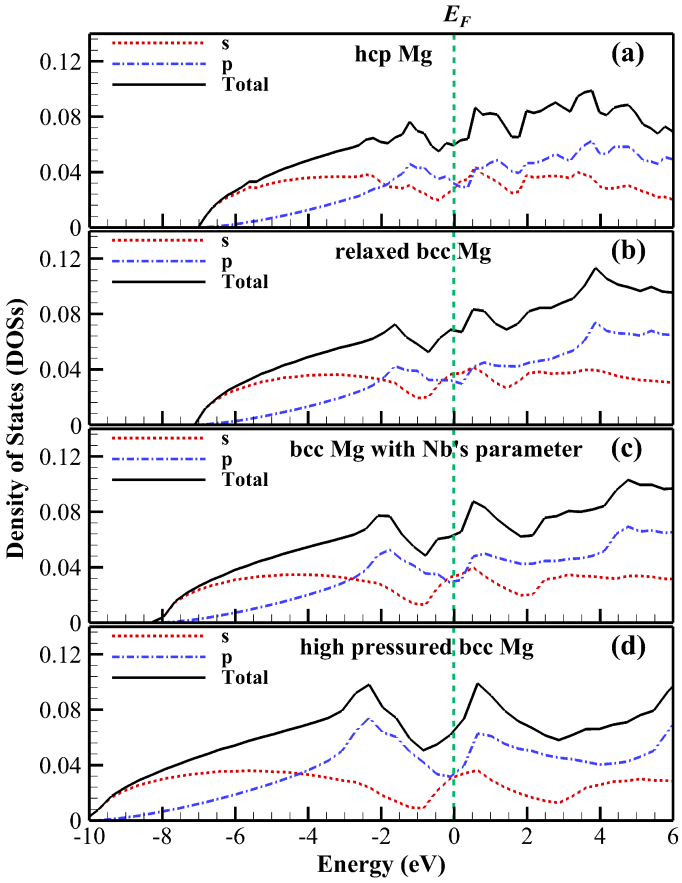

Figure 3.8: Partial Density of States (DOS) in (a) hcp Mg, (b) relaxed bcc Mg, (c) bcc Mg with bcc Nb's lattice parameter and (d) high pressured bcc Mg. Fermi level (E_F) is represented by an vertical dashed line.

3.2.3.6 Burgers' transformation

The transformation path proposed by Burgers when studying the bcc-hcp transformation in Zirconium (Zr) [155] has been used to describe the bcc-hcp transition in many metals such as barium (Ba) [156], titanium (Ti)[157], and iron (Fe) [158]. The crystallographic orientation relations (OR) during the bcc-hcp transition are typically $(110)_{bcc}||(0001)_{hcp}$ and $[110]_{bcc}||[11\bar{2}0]_{hcp}$ [155]. This transition consists of shearing and shuffling in specific directions and planes.

The simplest bcc to hcp transition occurs through the (intermediate) base-centered orthorhombic structure (oS4) by keeping the atomic volume constant. Two independent processes are necessary to realize this transformation: first, a shear deformation from bcc (110) planes to the hexagonal basal plane and, second, an alternate shuffle along the $[1\bar{1}0]$ direction of the planes. The deformation during the Burgers transformation is quantified in terms of two order parameters denoted as λ_1 and λ_2, which represent shear deformation and shuffle displacement, respectively. By starting with the bcc lattice parameter a, the intermediate orthorhombic lattice parameters vary during the transition according to the following relations:

$$a_0(\lambda_1) = \frac{a}{\alpha(\lambda_1)}, \qquad b_0(\lambda_1) = \alpha(\lambda_1)\sqrt{2}a, \qquad c_0 = \sqrt{2}a, \tag{3.8}$$

where

$$\alpha(\lambda_1) = 1 + [(\frac{3}{2})^{\frac{1}{4}} - 1]\lambda_1, \qquad \alpha = [(\frac{1}{\sqrt{2}})tan(\frac{\theta}{2})]^{\frac{1}{2}} \tag{3.9}$$

In the bcc and hcp structures, θ takes values of 109.47° and 120°, respectively. The positions of the two atoms in the cell, x_1 and x_2 are given by $[(3+\lambda_2), (3+\lambda_2)/12, 1/4]$ and $[-(3+\lambda_2, -(3+\lambda_2)/12, -1/4]$, respectively. (λ_1, λ_2) is (0,0) for the bcc structure, and (1,1) for the hcp structure, respectively.

Fig. 3.9(a) and 3.9(b) show the calculated total energy contours as a function of (λ_1,λ_2) in relaxed bcc-Mg and bcc-Mg with bcc-Nb's lattice parameter, respectively. The Burgers path shown in Fig. 3.9(a) corresponds to the transformation from bcc (a=3.571Å,V=45.538Å^3/f.u.) to hcp (a=3.227Å, c=5.050 Å, c/a=1.565). For the case of bcc Mg with Nb's lattice parameter, the initial bcc structure with a=3.324 Å(V=36.727 Å^3/f.u.) is transformed to the hcp Mg (a=3.004 Å, c=4.701 Å, c/a=1.565) shown in Fig. 3.9(b). In both contours, the bcc structures are located at unstable/metastable saddle points, while the hcp structures are located at the global minima. This result is reasonable as the hcp Mg is more stable than the bcc Mg structure in a bulk form.

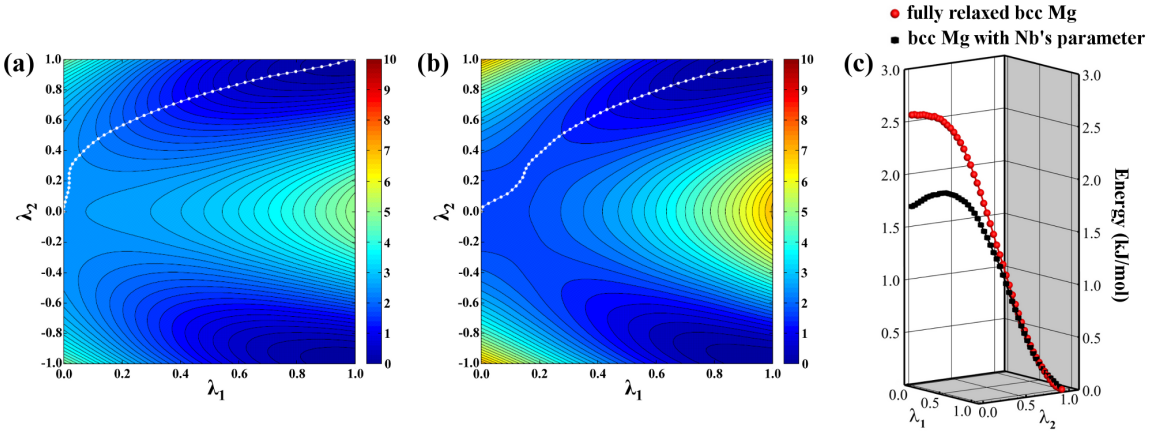

Figure 3.9: The total energy contour (kJ/mol) as a function of $\lambda_1$and λ_2 for the Burgers' paths of (a) fully relaxed bcc Mg and (b) bcc Mg with bcc Nb's lattice parameter. Minimum Energy Path (MEP)is represented by white dots. The contour step is 0.234 kJ/mol. (c) Comparison the MEPs of bcc Mg model (red circles)and bcc Mg with Nb's lattice parameter model (black squares)

The minimum energy path (MEP) was analyzed in both systems. The MEP for the Burgers transformation is identified by using the modified string method

proposed by Weinan *et al.* [159], which is derived from the zero temperature string method [160]. From the MEP analysis, energy barriers as a function of λ_1 and λ_2 of both models are compared in Fig. 3.9(c). The lines with red circle and black square markers represent the MEP of bcc Mg and bcc Mg with Nb's parameter, respectively. The magnitude of the energy difference between bcc Mg (0,0) and hcp Mg (1,1) in bcc Mg is 2.566 kJ/mol, while the magnitude of the energy difference between bcc Mg with Nb's lattice parameter and hcp Mg with Nb's lattice parameter is 1.817 kJ/mol. Moreover, it can be observed that the bcc structure corresponding to the Burgers transformation of bcc Mg with the lattice parameter of bcc Nb actually sits on a metastable saddle point along the energy landscape. This means that the transformation from bcc to hcp is not spontaneous as there is a finite (albeit small) barrier to the transformation. This is not the case for bcc Mg with fully relaxed lattice parameter. In this latter case, the bcc-hcp transformation is barrier-less, and therefore spontaneous.

3.2.4 Conclusions

The predicted bi-phase diagram of Mg/Nb multilayers has a good agreement with the experimental data. Both metastable bcc Mg and hcp Nb can be stabilized under Mg/Nb multilayers under appropriated thickness region and volume ratio of components. Under nano scale thin film conditions, the reduction in the interfacial energy is the dominant effect that controls the phase stability of nano-scaled multilayers. For the same bilayer thickness, the magnitude of the lattice distortion of metastable phase is related to the volume fraction of the constituents.

In the second part, the stabilization of bcc Mg in multi-layered Mg/Nb nanofilms [118] was examined by using calculations based on the DFT approach. Under normal thermodynamic constraints, bcc Mg is unstable and this is manifested by the

presence of an imaginary branch along the $\Gamma - N$ direction in the Brillouin zone, which is related in turn to the existence of a local maximum in the e-DOS at the Fermi level. The observed stabilization of bcc Mg in Mg/Nb nano-films is associated with the disappearance of the local maximum in the e-DOS at the Fermi level and results from the reduction in the lattice parameter of bcc Mg. Calculations of the Burgers transformation path between bcc and hcp show that bcc Mg sits on a local minimum in the energy landscape when comparing bcc and hcp structures. This, along with the calculated hardening of the soft TA branch along the $\Gamma - N$ direction indicates that the stabilization of bcc Mg is mainly due to the mechanical constraints imposed when Mg is forced to (epitaxially) grow on bcc Nb. The stabilization of bcc Mg grown epitaxially on the bcc Nb substrate [118] is thus analogous to the stabilization of bcc Mg under high pressures [115].

These results provide further motivation to investigate the synthesis of Mg-based materials with properties not observed in bulk Mg by using thin film engineering. Based on this work, it is likely that similar stabilization effects can be generated by using other bcc substrates, as long as their lattice parameter is smaller than that of (fully relaxed) bcc Mg, the substrate is immiscible with Mg and is much stiffer than Mg. This stabilization can be further improved through the use of alloying, as demonstrated in the work by Tan *et al.* [114].

4. INTERFACE CALCULATIONS OF MG/NB THIN FILMS

The purpose of this chapter is to expand our investigations on Mg/Nb films. The DFT approach was used for understanding the stable and metastable interfacial structures observed experimentally in Mg/Nb nanofilms. Possible Mg/Nb multilayer models, which consist of hcp Mg(0001)/bcc Nb(110), bcc Mg (110)/bcc Nb(110), and hcp Mg(0001)/hcp Nb(0001) multi-layers and corresponding freestanding films were considered in this work. Some important properties of these films (e.g. structural, energetic, electronic charge properties) were compared to those properties of bulk Mg and bulk Nb.

4.1 Introduction

The cohesive and structural properties of the interfaces in various systems have been explored through both computational and experimental work. For example, the structure, bonding, adhesions and other properties of the Cr/Fe [161], the Nb/W [162], the NiAl/Cr [163], the ZrC(100)/Fe(110) [164], and MgO/Fe [165] were investigated through the use of electronic calculations based on the DFT approach. A fundamental understanding of adhesion and electronic structure of interfacial systems can be pursued by computational studies.

Typically, there are two quantities used to elucidate the thermodynamic and mechanical properties of the interfaces. Firstly, the work of adhesion W_{ad} is defined as the reversible work needed to break interfacial bonds and separate the interface into two free surfaces. Plastic deformation and diffusion are neglected for simplification. Then, the mechanical properties can be linked to this W_{ad} value. The ideal W_{ad} is

represented in the following equation:

$$W_{ad} = 1A(E_{sl(A)} + E_{sl(B)} - E_{sl(A/B)}) \tag{4.1}$$

where $E_{sl(A)}$ and $E_{sl(B)}$ are the total energy of isolated slab A and B. The total energy of the interfacial slab is represented by $E_{sl(A/B)}$. A donates an interface area.

Another quantity is the interfacial energy γ_i, which is defined as the free energy difference between the interfacial atoms and the interior atoms. Besides that, the interface energy is the work required for producing the interface from bulk materials. Contrary to the work of adhesion, this quantity cannot absolutely measure the interface bond strength as interfacial energy results from the comparison of the energetic of atoms at the interface with respect to those in the bulk. In thermodynamic terms, this interfacial energy is simply the excess free energy of the interface.
The interfacial energy and the work of adhesion are dependent quantities related through the following relation:

$$\gamma = \sigma_A + \sigma_B - W_{ad} \tag{4.2}$$

For example, the W_{ad} and γ of 5ML-bcc Mg /5ML-bcc Nb model can be calculated from

$$W_{ad} = 1A(E_{sl(5ML-bccMg)} + E_{sl(5ML-bccNb} - E_{sl(5ML-bccMg)})$$
$$\gamma = \sigma_{5ML-bccMg} + \sigma_{5ML-bccNb} - W_{ad} \tag{4.3}$$

The surface energy σ_i of the slab i (i= A or B) can be calculated by:

$$\sigma_i = \frac{1}{2A}[E_{sl(i)} + (\frac{N_{sl(i)}}{N_{b(i)}})E_{b(i)}] \tag{4.4}$$

where $E_{sl(i)}$ and $E_{b(i)}$ stand for the total energies of the surface slab and the bulk structure of component i, respectively. The number of atoms i contained in the slab- and the bulk structures are $N_{sl(i)}$ and $N_{b(i)}$, respectively. The factor of 2 is used because there are two free surfaces in the surface model separated by a vacuum region. The surface energy signifies the stability of the surface.

4.2 Computational procedure

All calculations were performed with the DFT approach implemented in VASP [81]. The projector augmented method (PAW) [139] was used for a plane-wave basis. The local density approximation (LDA) [74] and the generalized gradient approximation (GGA)[166] were chosen for the exchange and correlation terms. In this work, electrons in $4p^6 4d^4 5s^1$ and $3p^6 3s^2$ orbitals have been taken into account as the valence electrons of Mg and Nb elements. The plan-wave cutoff is 520 eV. As for bulk calculations, Monkhorst-Pack grids of $18 \times 18 \times 18$ and $18 \times 18 \times 11$ were employed for k-point sampling in the Brillouin zone of the bcc and hcp primitive cells, respectively.

For the thin film calculations, the thickness of the simulated film is represented by the number of monolayers (ML). In all slab models, the slab is separated by a 20Åvacuum space in the direction normal to the surface. This vacuum prevents interaction between the images of periodic slabs. The k-mesh of $18\times10\times1$ was used. There are three main types of interfacial models, which are the hcp Mg(0001)/bcc Nb(110), the bcc Mg (110)/bcc Nb(110), and the hcp Mg(0001)/hcp Nb(0001) models. The interfaces were constructed based on the orientation relations observed by the experimental evidence [118], $0001_{hcp}||110_{bcc}$, $[2\bar{1}\bar{1}0]_{hcp}||[\bar{1}11]_{bcc}$, and $[01\bar{1}0]_{hcp}||[21\bar{1}]_{bcc}$. The

(110) stacking and (0001) stacking are used in the bcc- and the hcp-layers, respectively. In this paper, coherent interfaces are considered. For example, the in-plane lattice parameters of the bcc Mg(110)/bcc Nb(110) are laterally constrained to the lattice constants of bcc Nb. This simulated coherent interface relates to the HRTEM result in that the metastable bcc Mg has a lattice parameter similar to that of the bcc Nb layer. Similarly, the in-plane lattice parameters of the hcp Mg(0001)/hcp Nb(0001) are based on the lattice parameters of hcp Mg. According to a lattice mismatch of the hcp Mg(0001)/bcc Nb(110) interface, the coherent interfaces can be constructed by assuming the matching of the in-plane lattice parameters of Mg or Nb layers to each other occurs. Then, there are two models that can be considered, which are the distorted in-plane hcp Mg (pseudo-hcp Mg) and the distorted in-plane bcc Nb (pseudo-bcc Nb). The Mg-Mg and the Nb-Nb interlayer distances are obtained from the spacing between two (110) planes in bcc Nb and the spacing between two (0001) planes in hcp Mg, respectively. The interfacial spacing is an average value of the Mg-Mg and Nb-Nb interlayer distances in hcp Mg and bcc Nb.

The interfacial bcc Mg/bcc Nb models were created by fixing 5ML-bcc Nb thick and varying the thickness of the Mg layer, while the rest of the models were created by fixing 7ML-hcp Nb thick and varying the thickness of the Nb layer. The adhesion of pseudomorphic bcc Mg on bcc Nb was monitored through calculations of W_{ad}. Under the thin film condition, atoms are allowed to move along an out-of-plane direction, while they are constrained along the in-plane. Fig. 4.1(a)- 4.1(c) demonstrate the interface model of 5ML-bcc Mg(110)/5ML-bcc Nb(110) structure, 7ML-hcp Mg(0001)/7ML-hcp Nb(0001) structure and 7ML-hcp Mg(0001)/5ML-bcc Nb(110) structures, respectively.

Furthermore, the interactions between interfacial atoms were investigated by their electronic properties. The charge distribution, electron localization function

(ELF) and density of states (DOS) were used to indicate the interaction at the interfaces. The charge density and ELF contour of the unit cell were visualized by using VESTA [167].

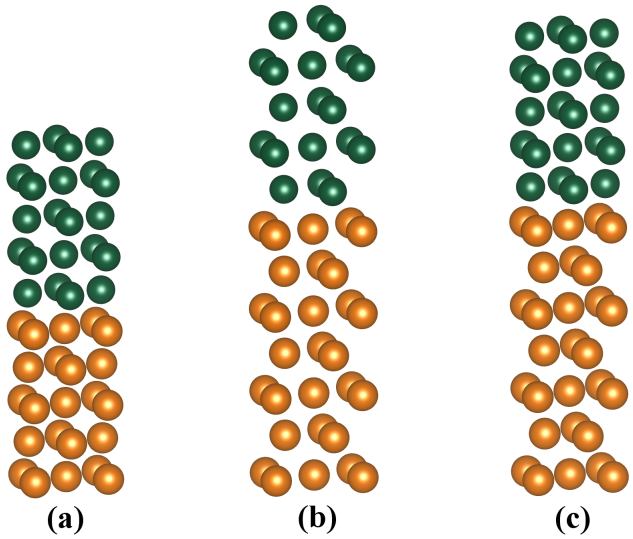

Figure 4.1: Slab models of (a) 5ML-bcc Mg(110)/5ML-bcc Nb(110) structure, (b) 7ML-hcp Mg(0001)/7ML-hcp Nb(0001) structure and (c) 7ML-hcp Mg(0001)/5ML-bcc Nb(110) structure

4.3 Bulk Mg and bulk Nb

4.3.1 Energetic and structural properties

The optimized cell parameters of bcc Nb, bcc Mg, and hcp Mg are displayed in Table 4.1. LDA calculations show smaller cell constants than those in GGA calculations for all models. The results obtained in this work are in good agreement with literature as it is usual for LDA calculations to overestimate cohesive energies in metals, resulting in smaller lattice cell parameters. GGA calculations, on the other

hand, tend to underestimate cohesion and result in larger lattice parameters. In the case of bcc Mg, the lattice parameters from literatures were characterized under high pressure condition [115]. Additionally, electronic charge properties of these bulk structures were also carried out.

Table 4.1: The optimized cell parameters of bulk structures (Å) by PAW-GGA and PAW-LDA

Structure	Calculation		Experiment
	LDA	GGA	
hcp Mg	a=3.140,c/a=1.622 (a=3.13, c/a=1.615[a])	a=3.197,c/a=1.622 (a=3.20, c/a=1.660[a])	a=3.22, c/a=1.624[b]
bcc Mg	a=3.508	a=3.571	a=2.9530±0.002[c]
bcc Nb	a=3.264	a=3.324	a=3.300[d]
hcp Nb	a=2.827, c/a=1.831	a=2.879, c/a=1.828	

[a][140], [b][142], [c][115], [d][144]

4.3.2 Bonding and electronic charge properties

In this part, Electron Localization Function (ELF) are combined with charge density analysis to further elucidate the electronic interactions in the systems under study. ELF was first proposed by Becke and Edgecombe [87]. ELF is originally defined by the probability density to find the second like-spin electron near the reference location. According to its magnitude of 0 to 1, it can verify the strength of repulsion between two electrons having same spin. In the other words, ELF can measure the same-spin pair density. The ELF is a useful tool to distinguish chemical bonding types in solids, such as metallic, covalent, and ionic bonds. ELF analysis has been used for identifying type of bonding [88, 89]. The bonding type are classified based on the topology and magnitude of ELF. ELF analysis of a given valence region

informs about bonding in that region as they concern only on the bonding electrons of the relevant valence shell. By definition, a local ELF value of 0.5 represented a electron gas, while a value close to 1.0 corresponded to paired electron in covalent bond and unpaired electron in a dangling bond [90]. However, ELF values lower than 0.5 cannot be properly identified to a particular type of bonding.

At this point, the electronic structures of the bulk phases were evaluated through valence charge density and ELF analysis. ELF and charge density contours projected on the (0001) plane of the conventional hcp structure and the (110) plane of the conventional bcc structure are discussed in this section. Those properties in bulk Mg and bulk Nb are demonstrated in Fig. 4.2(a)- 4.2(d) and Fig. 4.3(a)- 4.3(d), respectively.

Charge density analyses in Mg and Nb structures are displayed in Fig. 4.2(a)-4.2(b) and Fig. 4.3(a)-4.3(b), respectively. Charge densities at atomic positions show the denser charge densities than outer regions. Changes of charge densities around atomic sites can be indicated by contour lines. For Mg crystal, their charge and ELF contours of hcp form are more distorted than those in bcc form. Fig. 4.2(a) and 4.2(b) show electron distribution directions and interactions between Mg sites in hcp-and bcc-Mg lattices, respectively. Metallic characteristics can be observed in their ELF. At the core electron region, ELF presents very low value related to low charge density in the pseudopotential regime. Apparently, ELF maximum is $\sim$0.55 appeared between an atom and its nearest neighbor atoms, which identifies the free electron behavior in bcc Mg. The ELF maximum on (0001) plane is $\sim$0.69, this show the covalent-like behavior in hcp Mg.

For bulk Nb, slightly distorted shapes of charge distributions, presented in Fig. 4.3(a) and 4.3(b), indicate interactions among valence charges of Nb atoms. For typical metallic bonding, ELF value exists in range of 0.3 to 0.6 in the interstitial re-

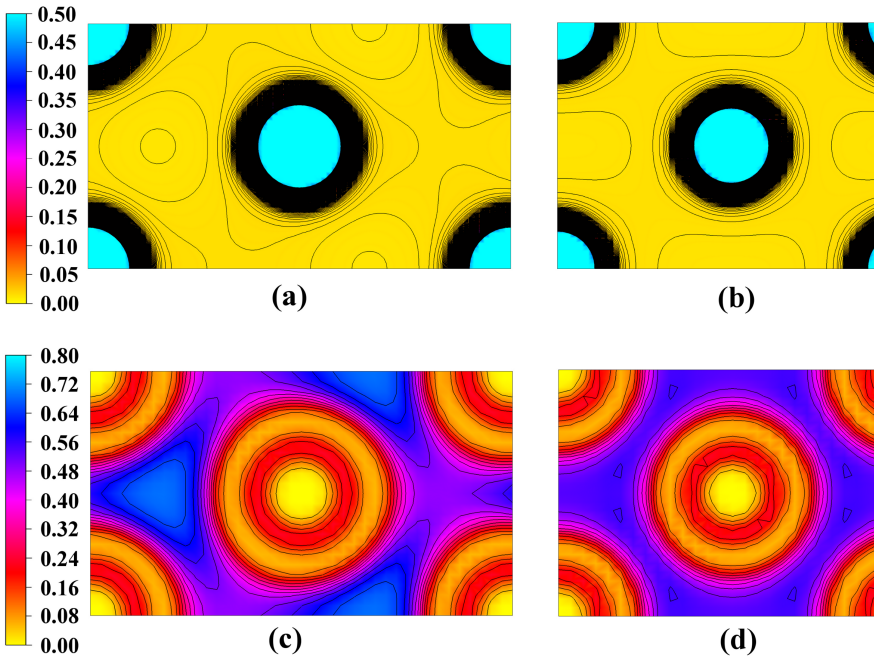

Figure 4.2: Electronic charge structures projected on the hcp(0001) and bcc(110) planes in Mg structures (a) the charge density distribution in hcp Mg, (b) the charge density distribution in bcc Mg, (c) the ELF contour in hcp Mg, and (d) the ELF contour in bcc Mg. For charge density distributions, the contour lines are drawn from 0 to 0.5 at 0.0015 e/Å^3 intervals. The contour lines are drawn from 0 to 0.80 at 0.05 intervals in ELF contours.

gions [168]. Then, the characteristic of metallic bonding also appears in the bcc Nb crystal shown in Fig. 4.3(d). Its ELF contour is influenced by the contribution of its 4d states. The complexity of d orbitals mediates on its ELF contour. The non uniform occupation of particular d orbitals affects the no spherical symmetry of ELF contour [169]. However, the complexity of ELF in hcp Nb shown in Fig. 4.3(c) cannot be explained explicitly.

Therefore, four crystal structures demonstrate metallic behavior. According to the electronic states of bcc crystals, there are two irreducible representations of the d orbitals, which are the e_g and the t_{2g} states. The e_g and the t_{2g} states point along

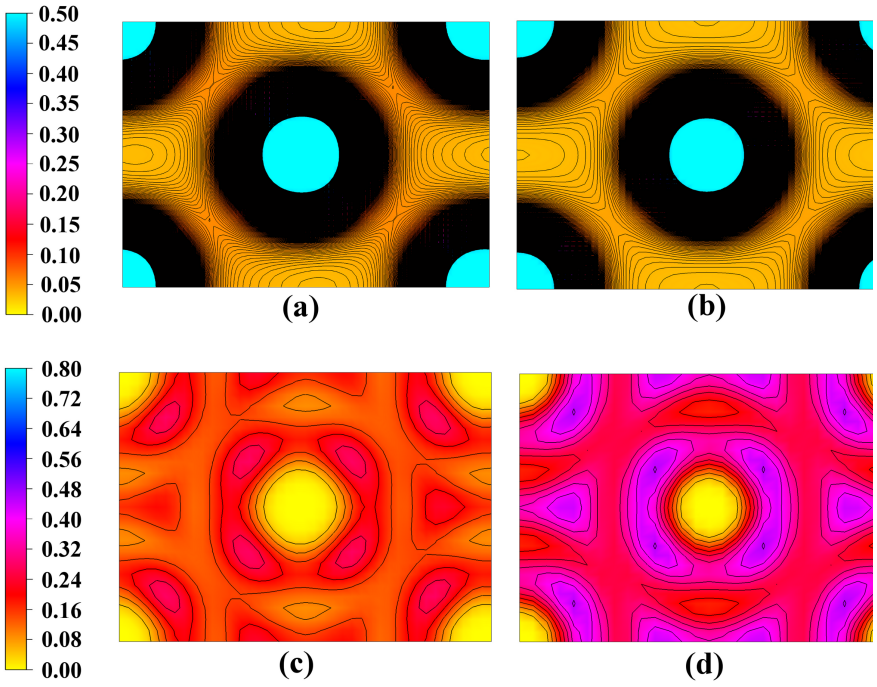

Figure 4.3: Electronic charge structures projected on the hcp(0001) and bcc(110) planes in Nb structures (a) the charge density distribution in hcp Nb, (b) the charge density distribution in bcc Nb, (c) the ELF contour in hcp Nb, and (d) the ELF contour in bcc Nb. For charge density distributions, the contour lines are drawn from 0 to 0.5 at 0.0015e/Å^3 intervals. The contour lines are drawn from 0 to 0.80 at 0.05 intervals in ELF contours.

[111] and [100] directions to the nearest-neighbor atoms. The bcc structure is more stabilized when more electrons are filled into the e_g states. These are the reason that bulk Nb posses in bcc form, while bcc Mg can be stabilized under high pressure. Because of compression stabilize the bcc Mg structure by lowering of $3d$ band toward the Fermi level (E_F) [170, 154].

Moreover, both partial density of states (PDOSs) and total density of states (DOSs) were attained from bulk Nb and Mg. The results are demonstrated in Fig. 4.4. A red dash line represents the Fermi level (E_F).

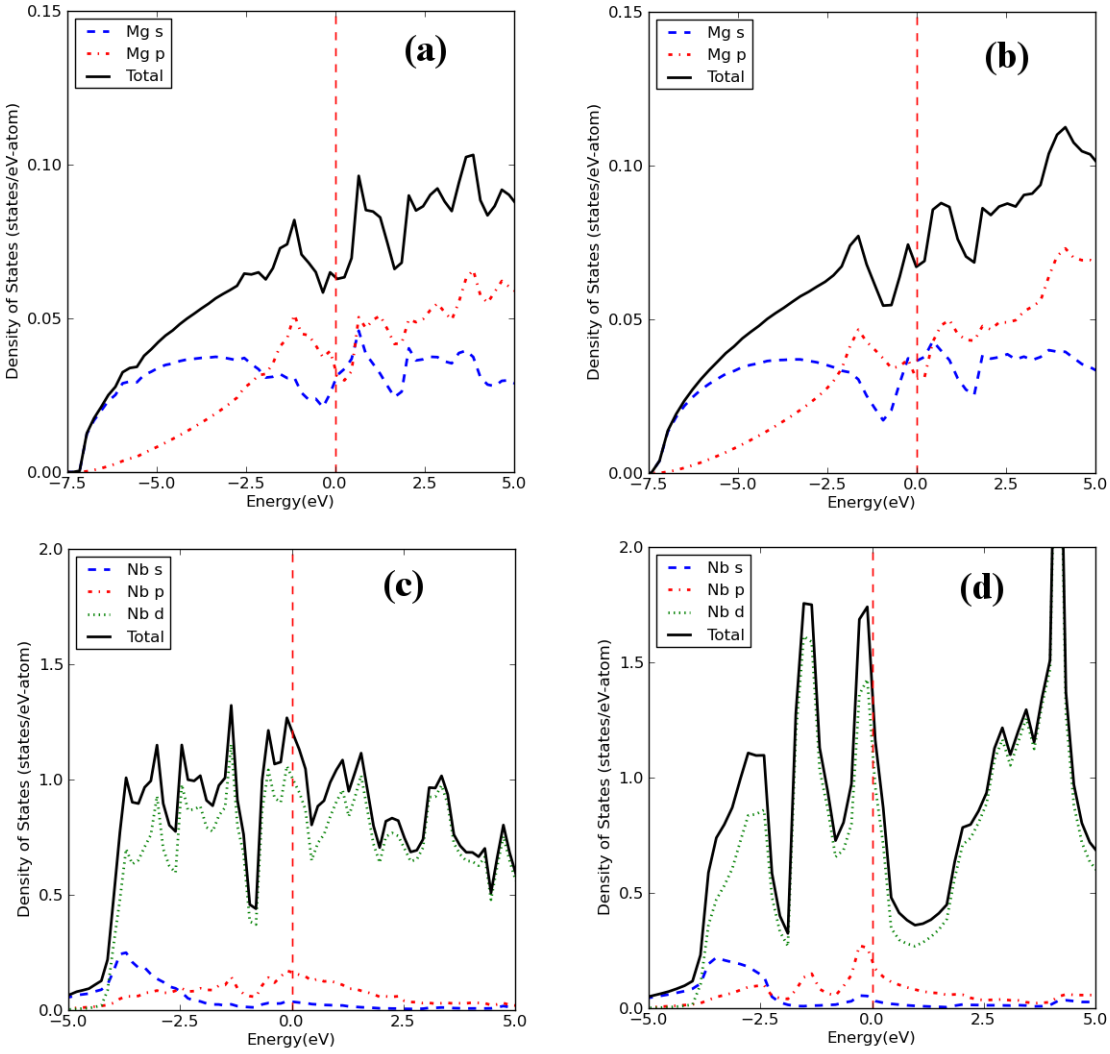

Figure 4.4: DOSs of (a) hcp Mg, (b) bcc Mg, (c) hcp Nb, and (d) bcc Nb

In Fig. 4.4, all Nb and Mg crystals have the metallic behavior as there is no significant band gap separating between conduction and valence bands. DOSs of hcp Mg reveal the same behavior with a literature [152]. For bcc Nb crystal, the

most contribution of DOSs comes from electrons in d band. There are three sets of peaks existing in DOSs of bcc Nb, which are -4 eV to -2 eV, -2 eV to 0.5 eV, and 2 eV to 6 eV. This result is in good agreement with literatures [171, 172, 173]. Both Mg forms provide similar DOSs, while there are some differences in the calculated DOS of two Nb forms. More continuous change can be observed around E_F in hcp Nb.

4.4 Surface and interface calculation of Mg/Nb films

4.4.1 Energetic properties

In this work, the interfacial properties of three major forms of interfacial structures in the observed synthesized multi-layer films, which are the hcp Mg(0001)/bcc Nb(110), the bcc Mg(110)/bcc Nb(110), and the hcp Mg(0001)/hcp Nb(0001), are determined by DFT calculations. By neglecting the incoherent interfaces, four coherent interfacial structures were constructed with the optimized lattice parameter of bulk Nb and bulk Mg. The number of Nb layers is varied from 1ML to 5ML, while the number of Mg layers is fixed at 7ML, in case of the hcp Mg(0001)/hcp Nb(0001), the hcp Mg(0001)/pseudo-bcc Nb(110), and the pseudo-hcp Mg(0001)/bcc Nb(110). For the bcc Mg(110)/ bcc Nb(110) models, the number of Mg layers is varied from 1ML to 5 ML, while the number of Nb layers is fixed at 5ML. The surface energies in isolated slabs, work of adhesion and interface energies in interfacial structures are shown in Fig. 4.5 and 4.6, respectively.

It is to be noted that the isolated 2ML-hcp Nb model exhibits very high surface energy, which is 6.17 J/m^2, compared with those in other Nb surface structures. This high surface energy, which represents a low stability, can be explained by splitting of two Nb layers observed in the relaxed 2ML-hcp Nb model. Due to that surface calculation, the W_{ad} and γ of the 7ML-hcp Mg /2ML- hcp Nb model are 10.05 and

-3.24 J/m^2. These high W_{ad} and low γ values indicated that forming bilayer structure with the 7ML-hcp Mg can stabilize the 2ML-hcp Nb. To compare the trends of σ, W_{ad} and γ in other models the calculated properties of the 2ML-Nb and the 7ML-hcp Mg/2ML-hcp Nb models are not present in Fig. 4.5 and 4.6.

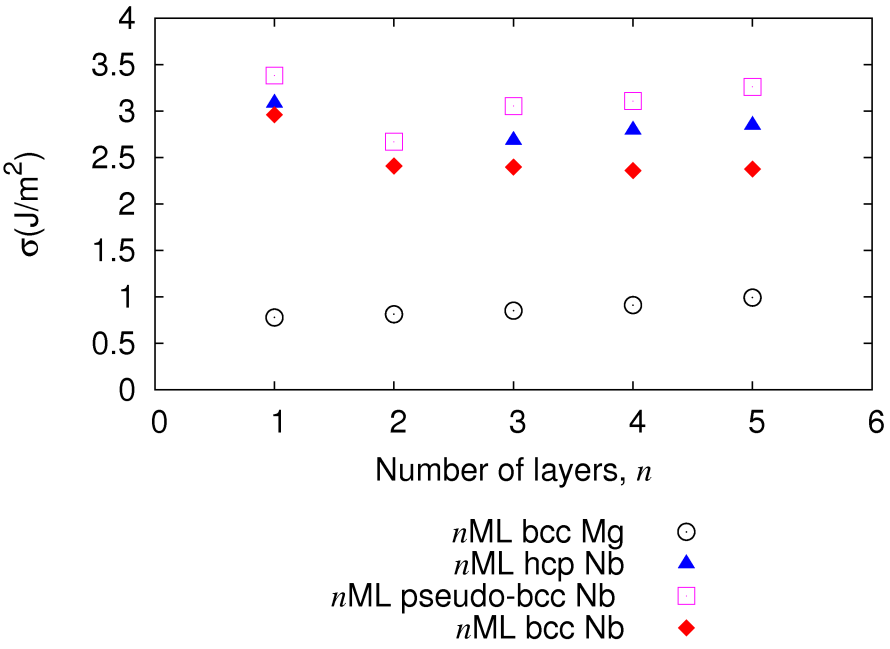

Figure 4.5: Surface energies in simulated surface models

In Fig. 4.5, calculated σ results of nML-bcc Mg, nML-pseudo-bcc Nb, and nML-bcc Nb are in range of 0.78 J/m^2 to 0.99 J/m^2, 2.67 J/m^2 to 3.38 J/m^2, and 2.36 J/m^2 to 2.96 J/m^2, respectively. The bcc Nb(110) surface has been claimed to be the most stable one among other low-index crystalline orientations, such as (100)

and (210) surfaces [174, 175]. From the literature, the surface energy of Nb (110) is in the range of 2.4 J/m^2 to 2.9 J/m^2 [174, 175, 176, 177, 178, 179]. The 2.655 J/m^2 of surface energy of this (110) plane was measured by experiment [180].

A slight increment of surface energies of the isolated bcc Mg(110) occurs as slab thickness increases. While a declining trend happens in a few isolated bcc Nb slabs, then it is steady after that. In case of the hcp Nb(0001) and the distorted bcc Nb(110), their surface energies tend to increase as the number of Nb layers are greater than three layers. Typically, the surface energy is related to the stability of one particular surface structure, so the Nb(110) facet is more stable as its thickness increases. Differently, there is less stability in the Mg(110) facet with increment of its thickness, which may be related to the fact that Mg is not stable in the bcc structure under normal conditions. Similar to the Mg(110) facet, the metastable hcp Nb and the distorted bcc Nb facets are less stable as the number of layers increases.

Next, the interface models were explored. Plots of W_{ad} and γ as a function of varied n layers, which specified in each interfacial model are shown in Fig. 4.6. Results for W_{ad} of the bcc Mg(110)/bcc Nb(110), the hcp Mg(0001)/pseudo-bcc Nb(110), and the pseudo-hcp Mg(0001)/bcc Nb(110) models are in range of 2.71 J/m^2 to 2.81 J/m^2, 2.26 J/m^2 to 3.03 J/m^2, and 2.71 J/m^2 to 3.25 J/m^2, respectively. In the hcp Mg(0001)/hcp Nb(0001) models, W_{ad} values are in range of 2.55 to 3.31 J/m^2, excluding the 7ML-hcp Mg /2ML-hcp Nb interface. Interestingly, all W_{ad} values are greater than zero. Significantly, these positive W_{ad} values demonstrate the attractive interactions between two layers at the interfaces in all simulated models, whether they are formed by metastable bcc Mg or metastable hcp Nb. However, W_{ad} values of the hcp Mg(0001)/hcp Nb(0001) models decrease when the number of hcp Nb layers increases. In case of metastable bcc Mg on bcc Nb, their W_{ad} are similar when the number of bcc Mg layers increases from 1ML to 5ML.

Fig. 4.6(b) shows that the excess free energy of the interface of the bcc Mg(110)/bcc Nb(110) increases with increasing of bcc Mg layers. The hcp Mg(0001)/pseudo-bcc Nb(110), and the pseudo-hcp Mg(0001)/bcc Nb(110) also have the similar trend when the number of Nb layers increases. While pseudo-hcp Mg(0001)/bcc Nb(110) models have the similar γ when the number of Nb increases. These results help verify the observed metastable phases in Mg/Nb thin films in the experiments.

In Fig. 4.6(b), the interface energies in the pseudo-hcp Mg(0001)/bcc Nb(110) models reveal similar values even if the number of bcc Nb layers change. Differently, the reductions of γ with lowering n values are presented in the rest interfacial models.

4.4.2 Microstructures of the surface and the interface models

To relate the calculations with real thin films conditions, the lateral extension of the models is fixed to that computed for bulk forms, but they are allowed to relax along the normal direction of (110) and (0001) planes for bcc and hcp layers, respectively. The relaxed interlayer distances $d_{i,j}$, where i and j represent two adjacent layers, were measured in both of surface and interface structures. The relaxation behavior are explained in term of the percentage of interlayer spacing change comparing with an initial value $\%\Delta d_{i,j}$, which is $(d_{i,j}$- $d_0)\times$ $100/d_0$. The d_0 values are 2.547 Åand 2.308 Åfor the hcp and bcc slabs, respectively. Calculated $\%\Delta d_{i,j}$ of selected Mg and Nb slabs are reported in Table 4.2. Expansion and contraction of the interlayer spacings referenced to the bulk values are indicated by the positive and negative signs of $\%\Delta d_{i,j}$.

Firstly, the microstructure of surface structures, which are isolated Mg and Nb slabs, are considered. It should be noted that these isolated films were simulated by placing slabs in the middle of cell and they are separated by 20Åvacuum on both sides. Thus, both sides of slabs are symmetric. For instance, the properties of the

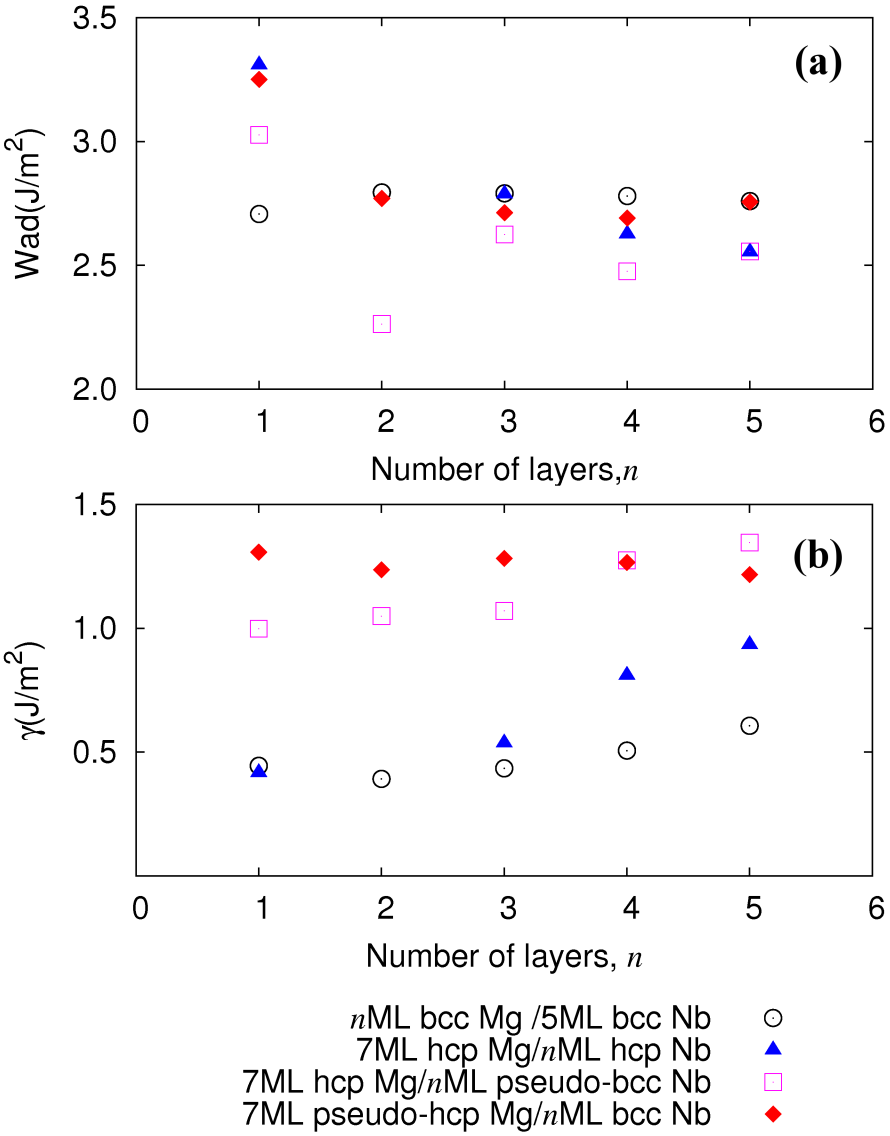

Figure 4.6: (a) Work of adhesion W_{ad}, and (b) interface energies γ in simulated interface models

first and the second layers of 5ML-Nb are identical to its fourth and fifth layers. Their structural changes after relaxation are reported in Table 4.2.

Table 4.2: Selected data of percentage of interlayer spacing change ($\%\Delta d_{i,j}$) of isolated Mg and Nb slabs

Structure	$\%\Delta d_{i,j}$		
	$\%\Delta d_{1,2}$	$\%\Delta d_{2,3}$	$\%\Delta d_{3,4}$
7ML-hcp Mg	+0.89	-0.17	-0.37
	$+1.9\pm0.3^a$	$+0.8\pm0.4^a$	-0.4 ± 0.5^a
	$+1.76^b$	$+0.0^b$	$+0.0^b$
	$+1.18^c$	$+0.36^c$	-0.73^c
	$+1.13^d$	$+0.31^d$	$+0.21^d$
7ML-pseudo-hcp Mg	+4.20	+3.05	+3.18
5ML bcc Mg	+4.41	+3.45	
5ML bcc Nb	-3.89	-0.00	
	-3.60^e	-0.5^e	
	-3.70^f		
	-4.3^g		
5ML pseudo-bcc Nb	-10.78	-4.93	
5ML hcp Nb	-24.42	-16.42	

[a]Experimental data (LEED 100K)[181],
[b]Experimental data (LEED 100K)[182],
Theoretical values: [c][183], [d][140], [e][184], [f][176], [g][173]

From this result, both of the surface and the in-plane constraint affect the relaxation behavior of the Mg and Nb slabs. The topmost interlayer distances of the Mg slabs are expanded comparing with the bulk values, and larger change can be examined in the pseudo-hcp Mg and the bcc Mg than that in the hcp Mg. There are both experimental and computational work investigating the interlayer relaxation in clean Mg(0001) surfaces [140, 185, 181, 183, 186, 187, 188]. An expansion of the topmost interlayer spacing in Mg(0001) was monitored in all works in slightly different of magnitude, while the next interlayer spacings show expansion or contraction behaviors in different works. From the experiments, the relaxations of the first three interlayer spacing of the clean Mg(0001)-(1×1) surface had been observed by using a dynamical low-energy electron diffraction (LEED) *I-V* analysis at 100 K [181]. They reported

that $\%\Delta d_{1,2}$= +1.9±0.3, $\%\Delta d_{2,3}$=+0.8±0.4, $\%\Delta d_{3,4}$= -0.4±0.5, $\%\Delta d_{4,5}$ = 0.0±0.5, where d_0 value is 2.61 Å. For the relaxations of the next interlayer separations, which are $\%\Delta d_{2,3}$ and $\%\Delta d_{3,4}$, are differ from other reported values in Table 4.2. However, these contractions of $\%\Delta d_{2,3}$and $\%\Delta d_{3,4}$ were present in theoretical investigations of the quatum-size effect (QSE) on Mg(0001) surface by Li *et al.* [188] and Zhang *et al.* [179].

In contrast with the relaxations in the Mg(0001) surface, the contraction of the topmost interlayer is found in the 5ML bcc Nb(110), which is comparable with the results from references [184]. Nevertheless, interlayer spacing of inner layers seems to be bulk-like for the 5ML bcc Nb(110). Additionally, compressions of their interlayer spacing can be monitored in all Nb slabs. The distances between a surface and the first subsurface layer $\%\Delta d_{1,2}$ are more compressed than next interlayer spaces $\%\Delta d_{2,3}$. The most contraction is shown in the topmost interlayer spacing of 5ML hcp Nb. This shortening of interlayer spacing between the surface and subsurface layer will be discussed by their charge properties in next section.

Secondly, the configuration of interface structures are determined. Fig. 4.7 demonstrates the comparison of $\%\Delta d_{i,j}$ as a function of varied layers. In Fig. 4.7(a), $\%\Delta d_{i,j}$ of nML-bcc Mg/5ML-bcc Nb is presented. Not only the surface effect, but also the interface effect influence their structure. The last five layers are Nb layers in this case. After relaxation, all interlayer distances in Nb region are contracted, excluding $d_{2,3}$ which is expanded slightly. It can be observed that the interlayer distances in the first four Nb layers are constant, even if the number of Mg layers increases. However, the nearest Nb layer beneath an interface is influenced by the interface effect, with $d_{4,5}$ increasing as the number of Mg layers increases. In contrast to the Nb region, distances of all upper Mg layers, including the interface region, are greater than the initial spacing. This can be explained by the lattice mismatch strain effect of the in-

terface [189]. Elastic distortion of the epitaxial layers, i.e. Mg layers, can be observed when their in-plane lattice parameter is constrained to the lateral (in-plane) Nb parameters. Then, the epilayer lattice parameter normal to the interface relaxes along the out-of-plane direction. According the bulk calculations, the optimized lattice parameters in bcc Mg and bcc Nb are 3.508Å (3.571 Å) and 3.264 Å (3.324 Å) from LDA (GGA) calculations, respectively. In this case, the lattice parameter of epilayer is greater than that of substrate, and then the epilayer lattice parameter expands along the interface normal. In addition, the topmost interlayer spacing exposes the most extension due to the free surface effect. All Mg interlayer spacings, including the interface, tend to decrease when the number of Mg layers increase.

In Fig. 4.7(b)- 4.7(d), first seven layers represent the Mg region and the next five layers are Nb layers. $\%\Delta d_{i,j}$ in the 7ML-hcp Mg/nML-hcp Nb, the 7ML-hcp Mg/ nML-pseudo-bcc Nb, and the 7ML-pseudo-hcp Mg/nML-bcc Nb are shown in Fig. 4.7(b), 4.7(c), and 4.7(d), respectively. Most of Nb interlayer spacings in Nb regions are contracted. Considering the Nb regions in these three models, $\%\Delta d_{i,j}$ as a function of Nb layers change in the same way, but in different values or magnitudes. For instance, the topmost Nb interlayers have the most contraction, and then next sublayers are less contracted than those in the topmost Nb interlayers. In these three major models, the black filled circles are the interfacial interlayers, which their reference values (d_0) are the average of the hcp Mg(0001) and the bcc Nb(110) spacings. Comparing Fig. 4.7(b) and 4.7(c), their $\%\Delta d_{i,j}$ as a function of Nb monolayers alter as the same trends, but the interfacial distances in the 7ML-hcp Mg/nML-hcp Nb models are closer than those in the 7ML-hcp Mg/nML-pseudo-bcc Nb. For the Mg regions in Fig. 4.7(b)- 4.7(d), $\%\Delta d_{i,j}$ as a function of Nb layers of the 7ML-pseudo-hcp Mg/nML-bcc Nb models have most change than other models. Obviously, the interfaces dominate the change in Mg regions in these three models.

Also, the lattice mismatch strain effect can be used for explaining these results. The interaction between two layers at the interface will be discussed in further sections.

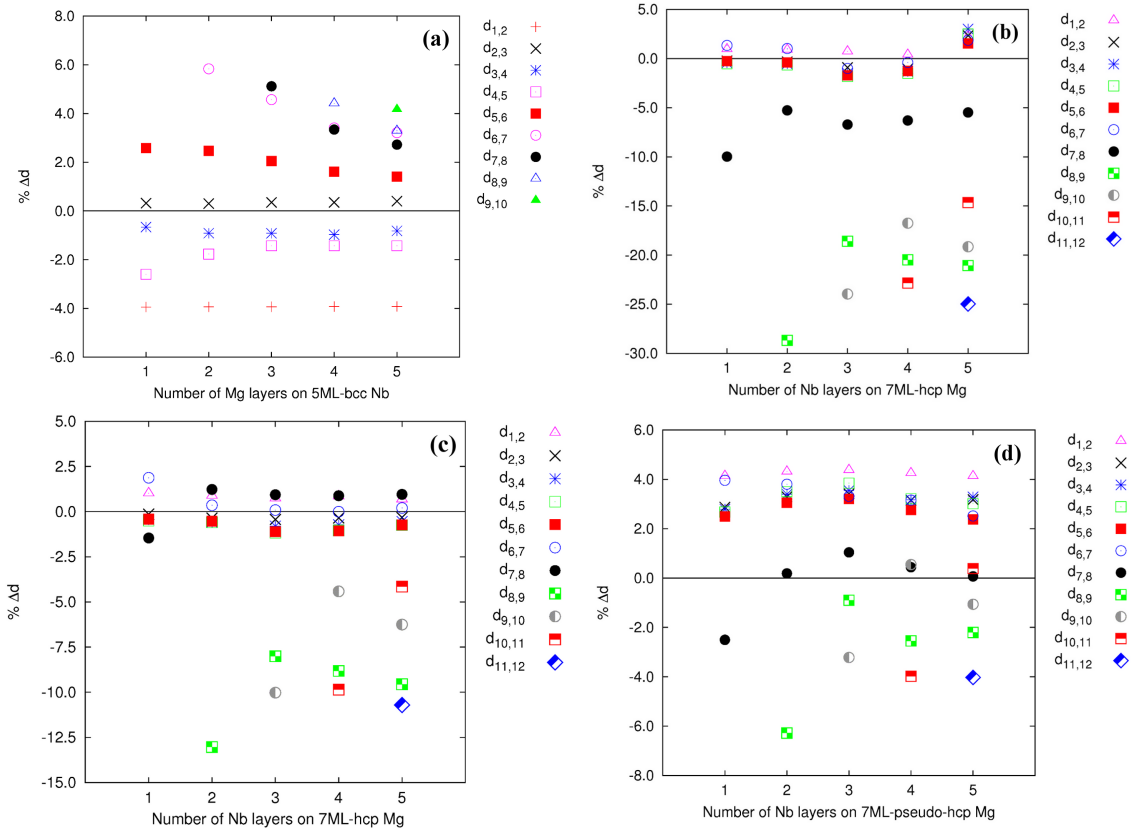

Figure 4.7: A percentage of interlayer spacing change $\%\Delta d_{i,j}$ in (a) nML-bcc Mg/5ML-bcc Nb, (b) 7ML-hcp Mg/nML-hcp Nb, (c) 7ML-hcp Mg/ nML-pseudo-bcc Nb, and (d) 7ML-pseudo-hcp Mg/nML-bcc Nb, where n=1-5

4.4.3 Bonding and electronic charge properties

In order to identify the type of atomic bonding across the interfaces studied, the electronic charge properties of the interfacial models are presented in this part. In

this section, the electronic charge density distribution, ELF, and DOSs analysis were evaluated to clarify interactions in slab structures.

4.4.3.1 Charge distribution and ELF analysis of 5ML-Mg and 5ML-Nb structures

According the symmetry of both surfaces, the contour plots of selected surface slabs are presented from the surface region to the middle layer of structures. The charge distributions and ELF contours of selected freestanding slabs are illustrated in Fig. 4.8(a)- 4.8(d), and Fig. 4.8(c)- 4.8(h), respectively.

In case of the Mg slab, the charge density distributions are distorted along an in-plane direction, which are shown in Fig. 4.8(a) and 4.8(b). Fig. 4.8(e) and 4.8(f) show the ELF contours corresponding with those charge distributions of 7ML-hcp Mg and 5ML-bcc, respectively. For all ELF contours, ELF value is zero in the vacuum region. The ELF maximum reaches to $\sim$0.8 at the surface, and ELF values in an interior region also comprise higher magnitude than ELF values in bulk bcc Mg. This high ELF value indicated the covalent-like feature of metallic bonding which involves mixing of the s and p atomic valence orbitals. This result is supported by DOS analysis in a latter section.

For surface structures, interactions between atoms in Nb structures can be observed in both of charge density distributions and ELF contours. Their charge distributions and ELF contours of 5ML-hcp Nb and 5ML-bcc Nb illustrate in Fig. 4.8(c)-4.8(d) and Fig. 4.8(g)- 4.8(h). The distributions of charge densities among those atoms can be notified obviously. In 5ML-bcc Nb, interactions between atoms in the second Nb layer have and atoms in the surface layer are also observed in Fig. 4.8(d). Additionally, these valence charge features of Nb slab can explain the shortening of interlayer spacing between its surface and subsurface layers. Fu *et al.* [190] proposed effects of localized d electrons and delocalized sp electrons on the relaxation of a

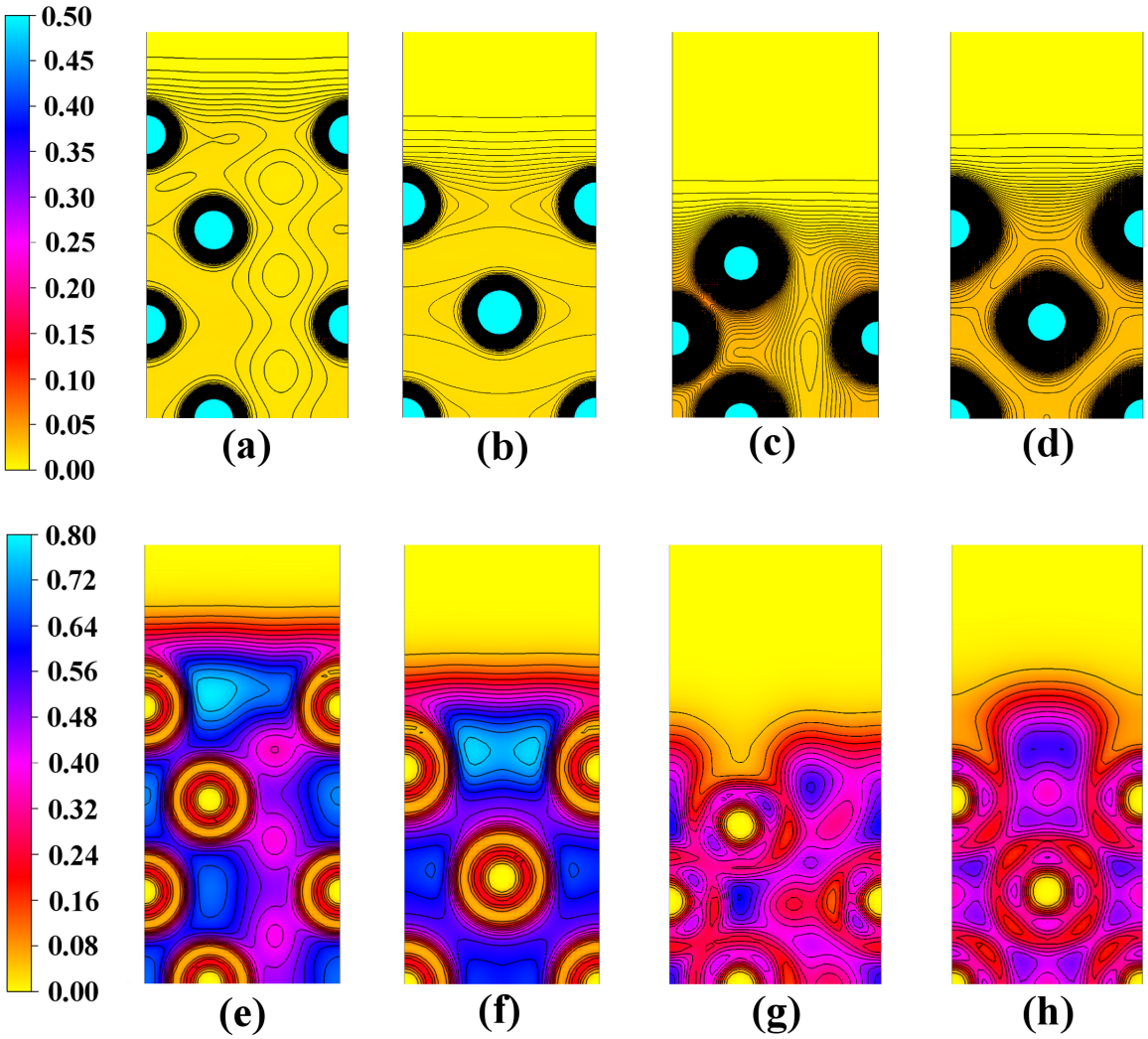

Figure 4.8: Charge distributions and ELF contours projected on (100) planes in freestanding slabs (a) charge distributions of the 7ML-hcp Mg model, (b) charge distributions of the 5ML-bcc Mg model, (c) charge distributions of the 5ML-hcp Nb model, (d) charge distributions of the 5ML-bcc Nb model, (e) ELF contour of the 7ML-hcp Mg model, (f) ELF contour of the 5ML-bcc Mg model, (g) ELF contour of the 5ML-hcp Nb model, and (h) ELF contour of the 5ML-bcc Nb model. For charge density distributions, the contour lines are drawn from 0 to 0.5 at 0.0015 e/$\mathring{A}^3$ intervals. The contour lines are drawn from 0 to 0.80 at 0.05 intervals in ELF contours.

transition-metal surface. Considering a bonding between surface atoms and subsurface atoms, the contraction of their interlayer distance happens as the $d-d$ bonding is increased and the delocalized *sp* electrons are extended outward to the vacuum region. In Fig. 4.8(g) and 4.8(h), the highest ELF value, which is ∼0.5, can be observed at a surface region. This high ELF value corresponds to the delocalized *sp* electrons on the topmost layer.

4.4.3.2 Charge distribution and ELF analysis of Mg/Nb interfaces

Contour plots of valence charge density and ELF on (100) cuts of selected interfaces are illustrated in Fig. 4.9(a)- 4.9(d) and Fig. 4.9(e)- 4.9(h). There are charge density gradient at the interface corresponding with the interaction across the interface.

The valence electron density distributions and ELF contour in the 5ML-bcc Mg/5ML-bcc Nb model are illustrated in Fig. 4.9(a) and 4.9(e). Its valence electron densities are distorted along an in-plane in each layer. Similar with the surface models, Mg region has higher ELF than Nb region. The ELF maximum is ∼0.8 at the surface Mg plane, which is not shown here. For Mg, ELF decreases along the direction from surface to interface area. For Nb, its ELF values are less than 0.5 found in inner layers, and its ELF maximum is shown at the surface. At the interface, the ELF values are close to 0.5 which signifies the free electron in metallic bonding. In other three interface models, which are the 7ML-hcp Mg/5ML-hcp Nb, the 7ML-hcp Mg/5ML-pseudo-bcc Nb, and the 7ML-pseudo-hcp Mg/5ML-bcc Nb models, reveal the similar characteristics in their charge structures. The interactions across the interface and metallic features can be elucidated as same as in the 5ML-bcc Mg/5ML-bcc Nb model.

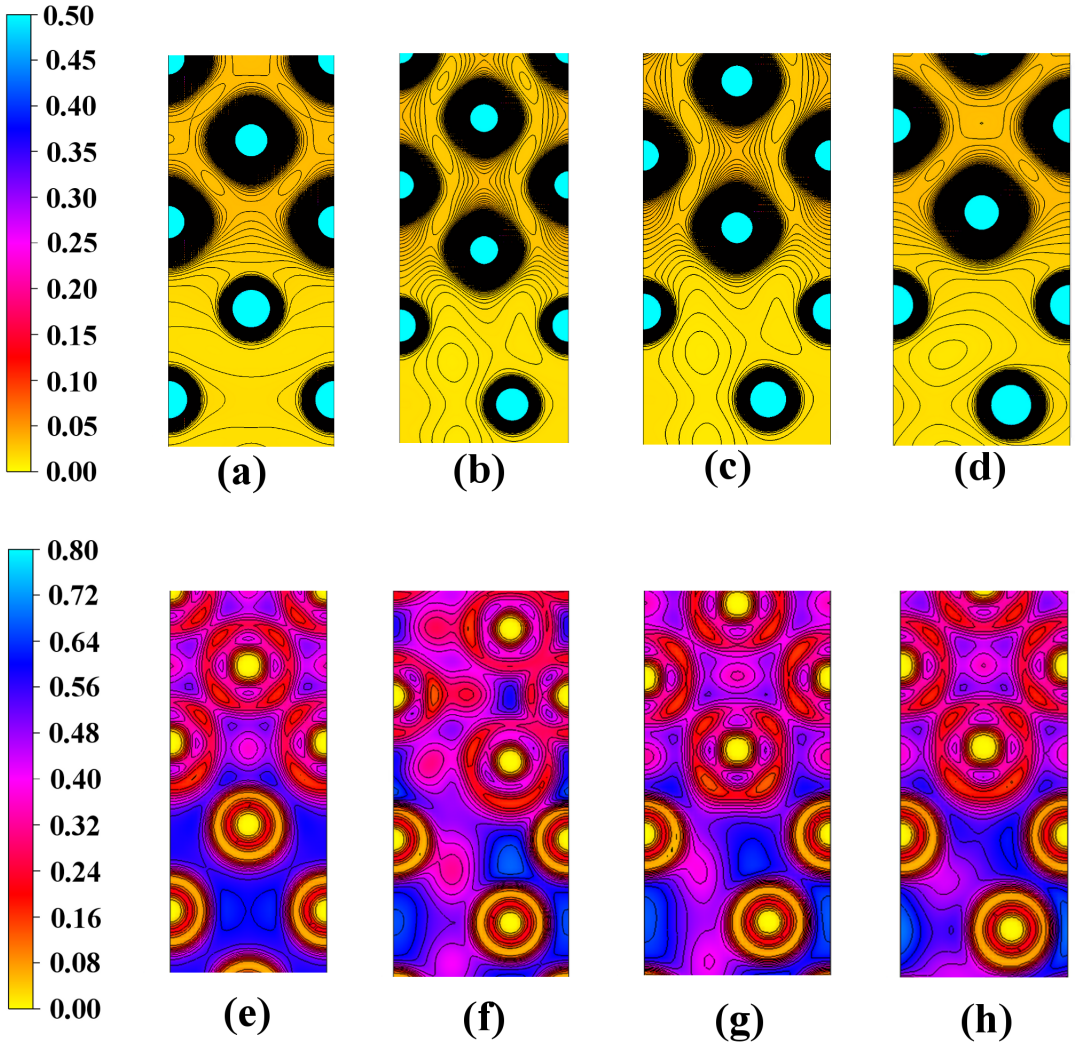

Figure 4.9: Charge distributions and ELF contours at the interfaces, projected on (100) planes in the interface structures (a) charge distributions of the 5ML-bcc Mg/5ML-bcc Nb model, (b) charge distributions of the 7ML-hcp Mg/5ML-hcp Nb model, (c) charge distributions of the 7ML-hcp Mg/5ML-pseudo-bcc Nb model, (d) charge distributions of the 7ML-pseudo-hcp Mg/5ML-bcc Nb model, (e) ELF contour of the 5ML-bcc Mg/5ML-bcc Nb model, (f) ELF contour of the 7ML-hcp Mg/5ML-hcp Nb model, (g) ELF contour of the 7ML-hcp Mg/5ML-pseudo-bcc Nb model, and (h) ELF contour of the 7ML-pseudo-hcp Mg /5ML-bcc Nb model. For charge density distributions, the contour lines are drawn from 0 to 0.5 at 0.0015 e/$\AA^3$ intervals. The contour lines are drawn from 0 to 0.80 at 0.05 intervals in ELF contours.

4.4.3.3 Density of states (DOSs)

The DOS in interface structures were carried out in comparison with the data for bulk Mg and Nb. The layer-projected DOS (LPDOS) of the freestanding films are not shown in this part, because they poses the similar aspects as the interface models. Fig. 4.10 to Fig. 4.13 demonstrate the layer-projected DOS (LPDOS) of selected interface models, which are the 5ML-bcc Mg/5ML-bcc Nb, the 7ML-hcp Mg/5ML-hcp Nb, the 7ML-hcp Mg/5ML-pseudo-bcc Nb, and the 7ML-pseudo-hcp Mg/5ML-bcc Nb models, respectively.

As a result, LPDOS in forming interfaces present different behaviors from those in bulk forms. In all interface structures, there are more filled electrons in electronic states than in their bulk states. In all Nb layers, LPDOS peaks are broadened near the Fermi level (E_F). For example, the LPDOS of each layer of the 5ML-bcc Mg/5ML-bcc Nb is illustrated in Fig. 4.10. Fig. 4.10(g) to 4.10(i) notify that interior layers pose in similar aspect. LPDOSs in multilayers also change from those in bulk forms. Likewise, the electronic behaviors in the rest model are similar with the 5ML-Mg/5ML-Nb model. In the multilayers, there are more states occupying in the valence bands than that in their bulks. In part of Nb layers, their LPDOSs are broad around E_F region compared to DOS of bulk Nb. The hybridization of *sp* orbitals are verified by overlapping of LPDOSs in Mg layers. A result of this interface structure is similar to its isolated Nb and Mg slabs in the region of the surface to interior layers. More number of states in both of *s*- and *p*-bands participates in valence band than in conduction band. These aspects imply that forming Mg/Nb multilayers affects on electronic properties of its components. Both of surface and interface parts dominate on their electronic characteristics.

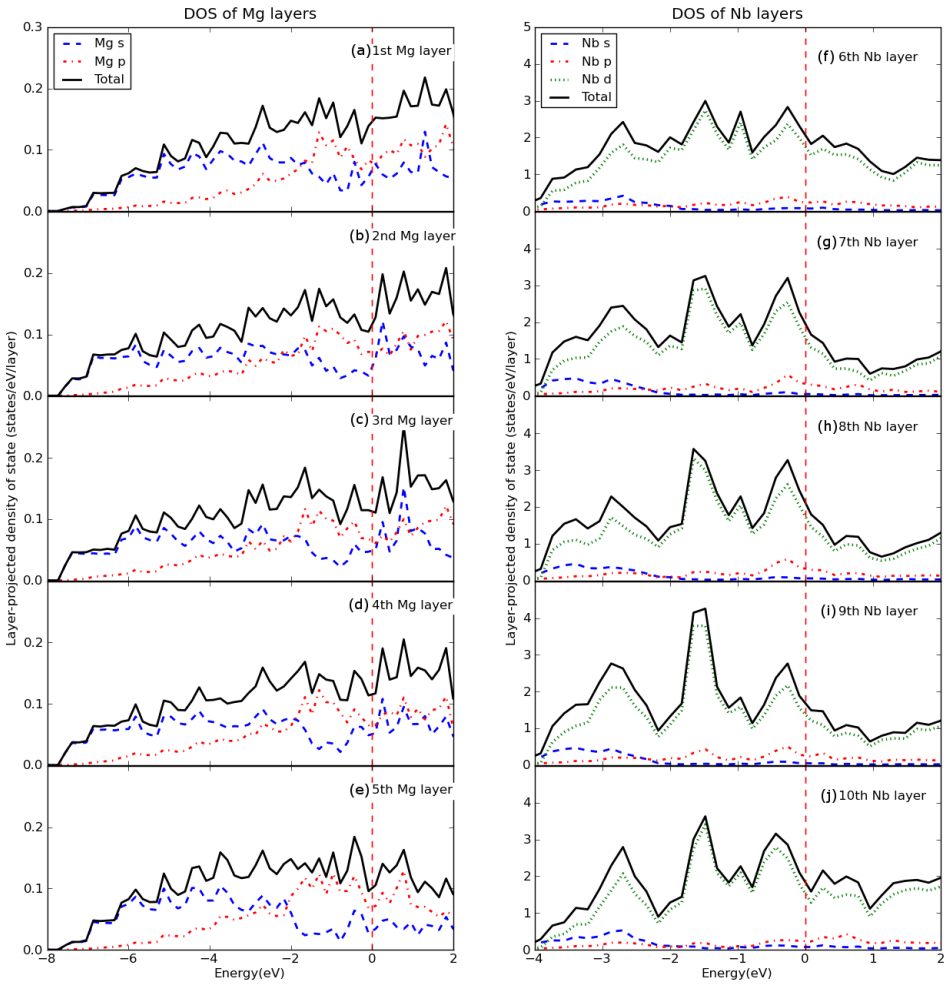

Figure 4.10: The layer-projected DOSs (LPDOSs) of the 5ML-bcc Mg/5ML-bcc Nb model (a)-(e) the first Mg layer to the fifth Mglayer (f)-(j) the sixth Nb layer to the tenth Nb

4.5 Conclusion

In conclusion, DFT methods were employed to study the stable and metastable interfacial structures in Mg/Nb multilayers. Calculated W_{ad} values correspond to

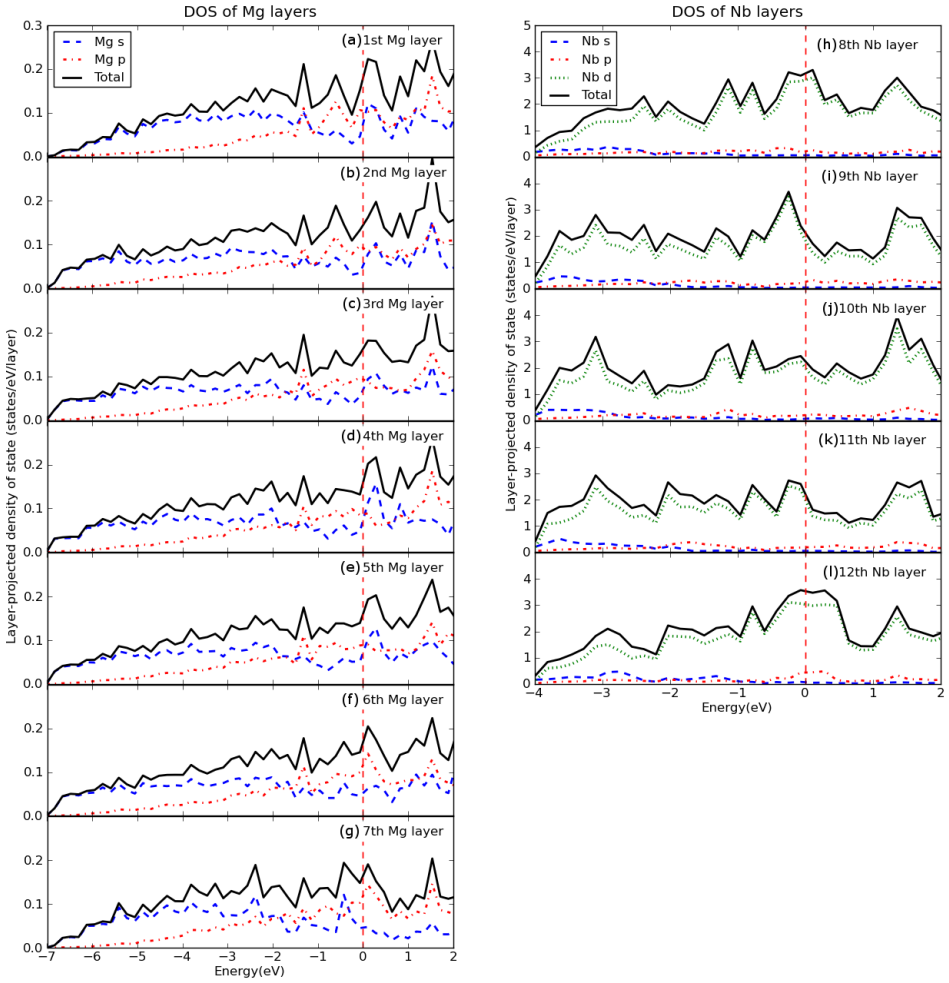

Figure 4.11: The layer-projected DOSs (LPDOSs) of the 7ML-hcp Mg/5ML-hcp Nb modell (a)-(g) the first Mg layer to the seventh Mg layer (h)-(l) the eighth Nb layer to the twelfth Nb

favorable interactions in all simulated interface models. This result supports an occurrence of metastable bcc Mg and hcp Nb phases in experiment. Moreover, the relaxed interlayer distances of surface and interface models were measured by

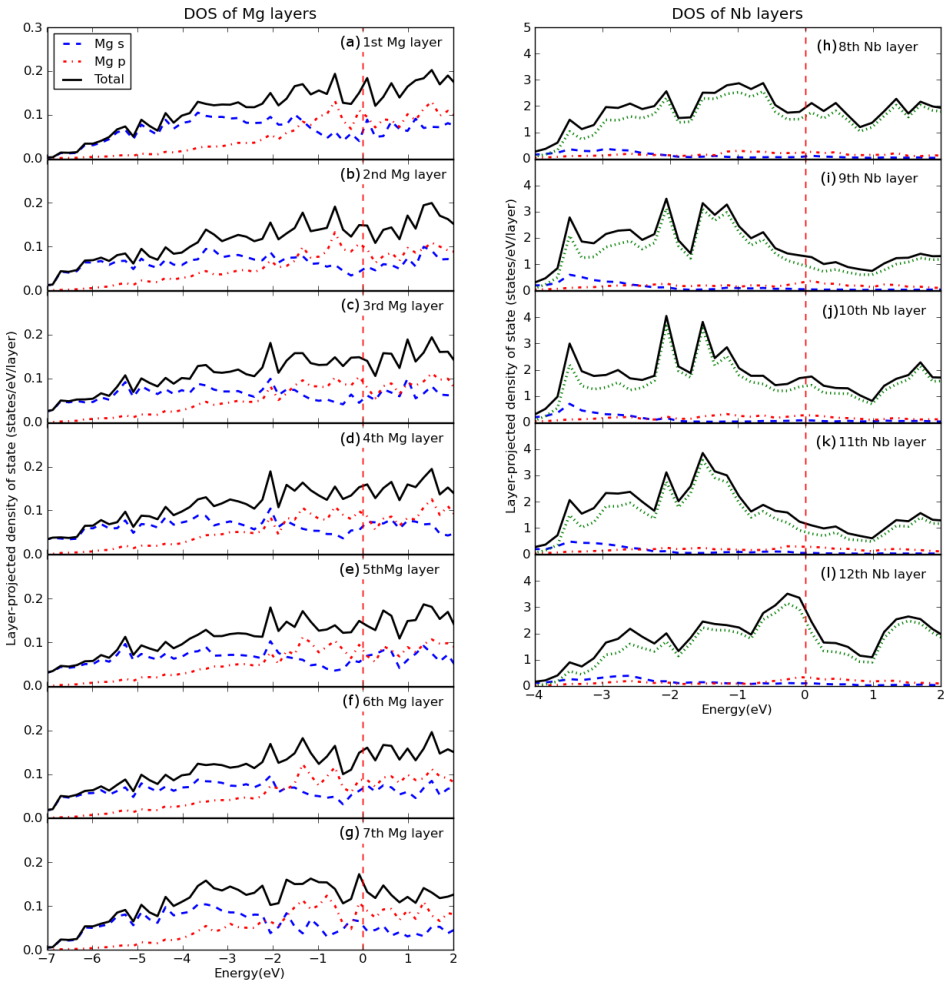

Figure 4.12: The layer-projected DOSs (LPDOSs) of the the 7ML-hcp Mg/5ML-pseudo-bcc Nb model (a)-(g) the first Mg layer to the seventh Mg layer (h)-(l) the eighth Nb layer to the twelfth Nb

comparing them with interlayer spacing of bulk forms. For isolated Nb film, the electronic properties dominate on the contraction of an interlayer spacing between its surface and subsurface layers. In case of Mg film, the interlayer expansions arise

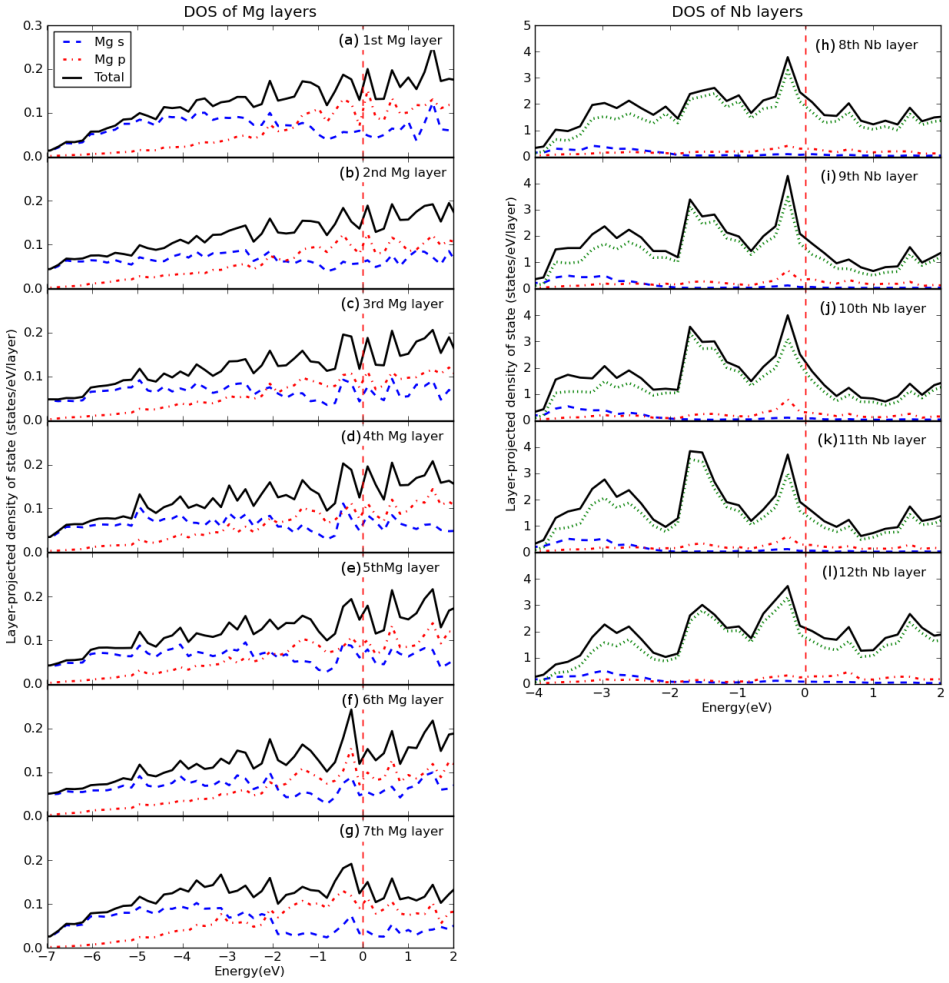

Figure 4.13: The layer-projected DOSs (LPDOSs) of the the 7ML-pseudo -hcp Mg/5ML -bcc Nb model (a)-(g) the first Mg layer to the seventh Mg layer (h)-(l) the eighth Nb layer to the twelfth Nb

from the lattice mismatch strain effect according to in-plane constraint. In the interface structures considered, they reveal a similar behavior to surface models, as well as the interface effect also dominates at interface region. The expansion values

of interfacial distance tend to decrease when number of Mg layers increases. Furthermore, the electronic charge properties were used as a tool for indicating bonding and interactions in structures. The metallic characteristics are present in both Mg and Nb regions. Comparison with electronic charge properties in bulk forms, more states are involved in valence bands in all slab models. The d orbitals provide the most contributions on interactions among Nb atoms. The partial covalent feature in metallic bonding presented in Mg region is investigated by DOS and ELF analysis.

5. ENHANCEMENT OF HYDROGEN SORPTION TROUGH METASTABLE ORTHORHOMBIC MG HYDRIDES IN MG-BASED THIN FILMS*

In this chapter, the hydrogen desorption properties of free standing Mg films and Mg/Nb multilayers were elucidated by DFT calculations. Thermodynamically destabilized Mg hydride under thin films can be explained by formation of enthalpies (ΔH_f) and estimating desorption temperatures (T_d) from DFT calculations. In addition, the computational tools were used for assisting the experimental characterization.

5.1 Introduction

As introduced in Chapter 1, the sorption properties of metal hydrides can be probed by PCI studies, which depicts the relationship between the hydrogen pressure and hydrogen composition in films under isothermal loading (unloading) conditions. This is illustrated in Fig. 1.8. Formation entropy (ΔS_f) and formation enthalpy (ΔH_f) can be used for estimated desorption temperature (T_d) by Van't Hoff's equation (given in Eq. 1.3), that is $ln[p_{eq(H_2)}/p^0_{eq}] = (\Delta H/RT) - (\Delta S/R)$.

The hydrogenation reaction in bulk Mg is described by $Mg + H_2 \rightleftarrows MgH_2$. The formation enthalpy of MgH_2 ($\Delta H_{f(MgH_2)}$) can be calculated by:

$$\Delta H_{f(MgH_2)} = E_{(MgH_2)} - E_{(Mg)} - E_{(H_2)} \tag{5.1}$$

where $E_{(MgH_2}$, $E_{(Mg)}$ and $E_{(H_2)}$ denote the calculated total energies (at 0 K) of

*Reprinted with permission from "Hydrogen sorption in orthorhombic Mg hydride at ultra-low temperature"by B. Ham, A. Junkaew, R. Arróyave, J. Chen, H. Wang, P. Wang, J. Majewski, J. Park, H.-C. Zhou, R.K. Arvapally, U. Kaipa, M.A. Omary, X.Y. Zhang, Y. Ren and X. Zhang. *International Journal of Hydrogen Energy*, 38(20):8328-8341, 2013. Copyright by ELSEVIER, available online at: http://dx.doi.org/10.1016/j.ijhydene.2013.04.098.

MgH_2 , bulk Mg and H_2, respectively. For bulk MgH_2 (rutile-type MgH_2 or T-MgH_2), ΔH_f and ΔS_f have been measured and reported in many studies at different conditions [191, 192, 193, 194]. In this study, the desorption temperature (T_d) were estimated by using ΔS_f = 135.0 J/mol·K [194]. Based on Eq. 1.3, the calculated ΔH_f of bulk MgH_2 is ∼77 kJ/mol·H_2, at ∼573 K and 1 bar.

5.2 Methodology

5.2.1 Experimental procedure

In this study, the experimental work was performed by B. Ham, X. Zhang and collaborators. Mg/Nb multilayers with individual layer thickness of 10 nm and 100 nm were deposited by DC magnetron sputtering on oxidized Si (100) substrates with 1 μm thermal oxides and on glass slides at room temperature. A 25 nm thick Pd cap layer was deposited on top of all films to protect samples from oxidization and catalyze the dissociation of hydrogen molecules. In multilayers the top and bottom layer were Nb so that Mg would not be in direct contact with the substrate or Pd. The films were grown under ∼0.33 Pa ultra high purity Argon. Mg and Nb single layer films, 1.6 μm in thickness, were deposited on Si substrates (2.5 cm×5 cm). Glass substrates were used for the deposition of 10 μm thick Mg 100 nm/Nb 100 nm multilayers and 30 μm thick Mg films. The deposition rates for Mg and Nb were ∼2 nm/s and ∼0.5 nm/s, respectively.

After deposition, samples were transferred directly into a custom-made high vacuum annealing chamber for hydrogen loading and unloading studies. Certain specimens were hydrided at 353 K for 12 hours. Hydrogen desorption studies were performed by thermal desorption spectroscopy (TDS) method. Samples were heated from room temperature up to a maximum of 623 K at a constant heating rate of 4 K/min. Pressure-composition isotherm (PCI) curve measurements were per-

formed. The characterization have been carried by using X-ray diffraction (XRD), transmission electron microscopy (TEM), scanning electron microscopy (SEM) and synchrotron XRD experiments.

5.2.2 Computational procedure

The structures of Mg hydride for DFT calculations were constructed based on experimental observations. The predicted lattice parameters and corresponding *d*-spacing values were then determined by using Powder Cell software [138]. All DFT calculations were performed using the VASP code [138]. The PAW-GGA method and the plane-wave cut-off of 350 eV were used. A self consistency convergence criterion of 10^{-7} eV for the total energy per simulation cell was applied. A $2 \times 2 \times 2$ Å^3 cell was used for calculating the properties of the H_2 diatomic molecule. Mg has the hexagonal closely packed (hcp) structure, and belongs to the $P6_3/mmc$ space group. At ambient conditions, the stable (bulk) MgH_2 has rutile (tetragonal) structure with the $P4_2/mnm$ space group. Monkhorst-Pack grids of $18 \times 18 \times 11$ and $9 \times 9 \times 13$ were used for k-point sampling in Brillouin zone of the hcp Mg and the T-MgH_2 primitive cells, correspondingly. The full relaxations were performed for these structures. For metastable (distorted) Mg hydride, a mesh of at least 10,000 k-points per unit cell was used. Hydrogen atoms are allowed to relax in the constrained lattice parameters.

DFT calculations tend to underestimate the formation enthalpy of MgH_2 and thus only qualitative comparisons between the measured and calculated (using DFT) desorption temperatures can be made. In this work, we used the calculated formation enthalpy of the stable tetragonal Mg hydride (T-MgH_2) at room temperature and atmosphere pressures as the reference to extrapolate the desorption temperature (T_d) in predicted orthorhombic Mg hydride (O-MgH_2). At 1 bar, the variation of T_d as a function of ΔH_f can be evaluated as the following equation:

$$T_{d(2)} - T_{d(1)} = (\Delta H_{f(1)} - \Delta H_{f(2)})/\Delta S \tag{5.2}$$

where 1 and 2 denote the properties of MgH_2 with either tetragonal or other MgH_2 structure. The difference between the formation enthalpy of the predicted MgH_2 structure and T-MgH_2, $\Delta H_{f(O-MgH_2)} - \Delta H_{f(T-MgH_2)}$, thus directly indicates the evolution of T_d.

5.3 Observation of metastable orthorhombic Mg hydride in Mg-based thin films

Based on the experimental characterization, the T-MgH_2 feature cannot be observed in both single layer case and multilayer case. The experimental data are provided in Table 5.2, 5.4 and Fig. 5.2. Other possible Mg hydride structures were sought to commit the experimental data. In literature, many possible Mg hydride structures such as α-PbO_2-type structure (Pbcn), CaF_2-type structure ($Pa\bar{3}$), $AlAu_2$-type structure (Pnma), $InNi_2$-type structure ($P6_3$), Ag_2Te-type structure ($P2_1/c$) and $AuSn_2$-type structure (Pbca), CaF_2-type structure ($Fm\bar{3}m$) and $CaCl_2$-type structure (Pnnm) were reported [195]. Among those magnesium hydride structures, the distorted $CaCl_2$-type MgH_2 structure provides the closest match to experimental d-spacings. On the other hand, other possible hydride structures do not show all the predominant d-values observed in experimental measurements. As a result, extensive analyses of the interplanar spacings (from TEM and synchrotron x-ray diffraction) suggest that the crystal structure of the magnesium hydride is orthorhombic in both single layer and multilayer case.

The distorted orthorhombic structures for the hydrides in single layer films and the multilayers are labeled as O_s-MgH_2 and O_m-MgH_2, respectively.

5.3.1 The determination of O-MgH_2 structure in single layer Mg films

From the synchrotron X-Ray data shown in Table 5.2 and Fig. 5.2(a), the first two dominant peaks are d(110) = 0.3148 nm and d(200) = 0.1926 nm. The relationship between the *d*-spacing of the (hkl) plane and the lattice constants (a, b and c) of the orthorhombic structure is expressed in the following equation:

$$\frac{1}{d_{hkl}^2} = (\frac{h}{a})^2 + (\frac{k}{b})^2 + (\frac{l}{c})^2 \tag{5.3}$$

The a and b parameters can be achieved from those observed *d*-spacings by using Eq. 5.3. The predicted models were constructed by matching the *d*-spacing data observed in synchrotron X-Ray diffractions presented in Table 5.1. The distorted $CaCl_2$-type MgH_2 structure with a = 0.3851 nm, b = 0.5464 and c = 0.3144 (c increases +4.59% from that in the regular $CaCl_2$-type MgH_2 structure), is perfectly matched with the x-ray diffraction data presented in Table 5.1 and Fig. 5.2(a). The O_s-MgH_2 structure has ∼7% volume expansion with respect to the volume of T-MgH_2. *d*-spacings of synchrotron X-ray measurement, predicted O_s-MgH_2 and T-MgH_2 are compared in Table 5.2. The contraction of a and expansion of b and c compared to T-MgH_2 structure can be observed and represented by the three dimensional structure in Fig. 5.1(b).

5.3.2 The determination of O-MgH_2 structure in hydrided Mg/Nb multilayers

In the multilayer case, the situation is more complex than in its single layer counterpart. Based on TEM measurement, the [200] direction is indexed as the out-of-plane direction and [011] direction is the in-plane direction. In TEM analysis, ∼6.8% expansion of the out-of-plane (d(200) spacing) and ∼3.7% contraction of the in-plane (d(011) spacing) indicate that the magnesium hydride is distorted to

Table 5.1: Predicted *d*-spacing (nm) of O_s-MgH_2 in hydrided single layer films with varied c-parameter (a- and b-parameters are fixed)

c change (%)	V change (%)	d_{110} (nm)	d_{101} (nm)	d_{011} (nm)	d_{200} (nm)	d_{111} (nm)	d_{201} (nm)	d_{211} (nm)	d_{001} (nm)
-10	-7.60	0.3148	0.2214	0.2425	0.1926	0.2052	0.1569	0.1508	0.2706
-8	-5.55	0.3148	0.2247	0.2468	0.1926	0.2078	0.1580	0.1518	0.2766
-6	-3.50	0.3148	0.2278	0.2510	0.1926	0.2103	0.1591	0.1528	0.2826
-4	-1.44	0.3148	0.2310	0.2552	0.1926	0.2127	0.1602	0.1537	0.2886
-2	0.61	0.3148	0.2340	0.2593	0.1926	0.2151	0.1612	0.1546	0.2946
0	2.66	0.3148	0.2370	0.2634	0.1926	0.2174	0.1622	0.1555	0.3006
2	4.72	0.3148	0.2399	0.2674	0.1926	0.2197	0.1631	0.1563	0.3067
4.59	7.37	0.3148	0.2436	0.2725	0.1926	0.2225	0.1642	0.1573	0.3144
6	8.82	0.3148	0.2455	0.2753	0.1926	0.2240	0.1648	0.1578	0.3187
8	10.88	0.3148	0.2482	0.2791	0.1926	0.2260	0.1656	0.1585	0.3247
10	12.93	0.3148	0.2509	0.2829	0.1926	0.2280	0.1664	0.1592	0.3307
Synchrotron		0.3148		0.2725	0.1926		0.1642	0.1573	

an orthorhombic form. However, the TEM data shows only local features of the microstructure. Thus, the synchrotron X-Ray data given in Table 5.4 was used to predict the structures. Whereas the a parameter can be attained directly from the observed d(200) spacing value, there are many possible b and c values which are related to the reported d(011) value (as expressed in Eq. 5.3). In this calculation, b parameter was varied from 20% contraction to 12% expansion from b-parameter in the $CaCl_2$-type MgH_2crystal studied by Vajeseston *et al.* [195]. Predicted *d*-spacings as a function of b parameter are reported in Table 5.3.

As a result, the distorted $CaCl_2$-type MgH_2 structure with a = 0.4903 nm, b = 0.3789 nm and c = 0.3215 nm reveals the most agreement to the experimental data. This O_m-MgH_2 is the distorted orthorhombic structure with ∼3% volume contraction from the T-MgH_2. The three dimensional structure of this predicted O_m-MgH_2 is displayed in Fig. 5.1(c). This structure is distorted differently form the O_s-MgH_2.

Table 5.2: Comparison d-spacings (nm) from synchrotron X-ray measurement and predicted O_s-MgH_2 in hydrided single layer Mg films (1.6 m in thickness)

#	index	Experiment	Predicted O_s-MgH_2 (a=0.3851nm, b=0.5464nm, c=0.3144nm)	T-MgH_2 (a=0.4517nm, c=0.3020nm)
1	O_s-MgH_2 (110)	0.3148	0.3148 (110)	0.3194 (110)
2	O_s-MgH_2 (011)	0.2725	0.2725 (011)	0.2511 (101)
3	O_s-MgH_2 (200)	0.1926	0.1926 (200)	0.2020 (210)
4	O_s-MgH_2 (201)	0.1642	0.1642 (201)	0.1679 (211)
5	O_s-MgH_2 (211)	0.1572	0.1573 (211)	0.1597 (220)

The contraction of b and expansion of a and c compared to T-$MgHH_2$ structure can be observed in this case.

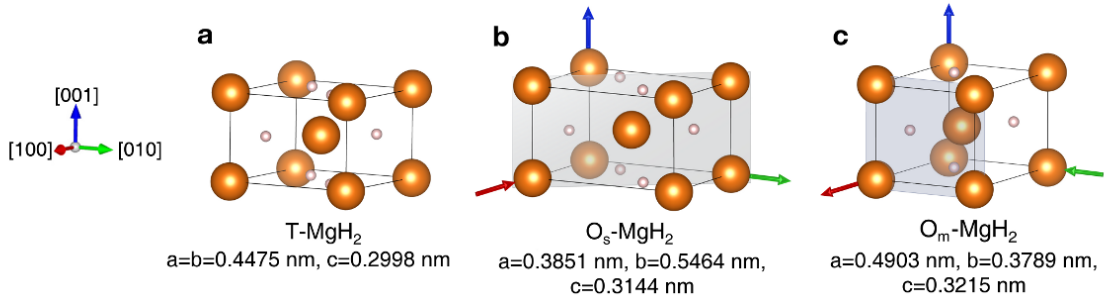

Figure 5.1: Three dimensional structures of Mg hydride crystals. (a) The T-MgH_2 with a=b=0.4475 nm and c=0.2998 nm. (b) The O_s-MgH_2 structure with a=0.3851 nm, b=0.5464 nm and c=0.3144 nm, which is con-sistent with the synchrotron XRD data for single layer O_s-MgH_2. (c) The O_m-MgH_2 structure with a=0.4903 nm, b=0.3789 nm, c=0.3215 nm, consistent with the synchrotron XRD data. Arrows indicate the direction of distortion compared to T-MgH_2.

Finally, synchrotron X-ray diffraction profiles of as deposited and hydrogen loaded single layer Mg films and Mg/Nb multilayers are indexed as shown in Fig. 5.2. After

Table 5.3: Predicted d-spacing (nm) of O_m-MgH_2 in hydrided Mg/Nb multilayers with varied b-parameter (a is fixed and c is varied coordinately)

b change (%)	V change (%)	d_{110} (nm)	d_{011} (nm)	d_{200} (nm)	d_{111} (nm)	d_{210} (nm)	d_{201} (nm)	d_{211} (nm)	d_{001} (nm)
-20	-4.21	0.2887	0.2451	0.2451	0.2193	0.2021	0.1982	0.1733	0.3370
-18	-3.85	0.2934	0.2451	0.2451	0.2193	0.2037	0.1968	0.1733	0.3300
-15.16	-3.08	0.2998	0.2451	0.2451	0.2193	0.2058	0.1949	0.1733	0.3215
-12	-1.93	0.3066	0.2451	0.2451	0.2193	0.2080	0.1931	0.1733	0.3136
-8	-0.14	0.3149	0.2451	0.2451	0.2193	0.2105	0.1912	0.1733	0.3055
-4	1.93	0.3227	0.2451	0.2451	0.2193	0.2128	0.1895	0.1733	0.2988
0	4.21	0.3302	0.2451	0.2451	0.2193	0.2149	0.1881	0.1733	0.2933
4	6.66	0.3372	0.2451	0.2451	0.2193	0.2168	0.1868	0.1733	0.2886
8	9.24	0.3438	0.2451	0.2451	0.2193	0.2185	0.1858	0.1733	0.2847
12	11.92	0.3501	0.2451	0.2451	0.2193	0.2201	0.1848	0.1733	0.2812
Synchrotron			0.2451	0.2451			0.1949	0.1733	0.3215

Hydrogen loading (373 K/24 h), the single layer Mg films completely transform to O_s-MgH_2 with strong (110) texture (Fig. 5.2(a)). Transformation of Mg to O_m-MgH_2 with (200) texture and Nb to O-NbH phase with (111) texture are revealed in both Mg/Nb 100 nm multilayers (Fig. 5.2(b)) and Mg/Nb 10 nm multilayers (Fig. 5.2(c)).

From the observed experimental data, the orthorhombic MgH_2 structure can be characterized from their distorted d-spacing values. However, the hydrogen atomic positions in these hydride forms are difficult to specify by experiment due to their light weight. The first principle DFT calculations have been compromised for investigating the structural property and thermodynamic stabilities of the suggested magnesium hydride forms found in the studied films in the next section.

Table 5.4: Comparison d-spacings (nm) from synchrotron X-ray measurement and predicted O_m-MgH_2 in hydrided Mg/Nb 100nm

#	index	Experiment	Predicted O_m-MgH_2 (a=0.4903nm, b=0.3789nm, c=0.3215nm)	Mismatch (%)	T-MgH_2 (a=0.4517nm, c=0.3020nm)
1	O_m-MgH_2 (200)	0.2451	0.2451 (200)	0	0.2511 (101)
	NbH (111)		0.2451 (011)		
2	O_m-MgH_2 (001)	0.3215	0.3215 (001)	0	0.3194 (110)
3	Mg (101)	0.2527		0	0.2511 (101)
4	Pd (111)	0.2267		0.93	0.2258 (200)
5	O_m-MgH_2 (201)	0.1961	0.1949 (201)	0.61	0.2020 (210)
6	O_m-MgH_2 (211)	0.1729	0.1733 (211)	-0.25	0.1679 (211)

5.4 Hydrogen desorption enhancement in Mg-based thin films

5.4.1 Experimental study of hydrogen sorption in Mg-based thin films

The hydrogen sorption properties of selected films were investigated experimentally and described in this part. The X-ray diffraction (XRD) patterns shown in Fig. 5.3 explain the structure transformation at before and after hydriding processes. The absorption/desorption temperatures of those films are labeled in those figures. Fig. 5.3(a) shows the transformation of the as-deposited Mg (1.6 mm on Si substrate) to an orthorhombic (110) textured O_s-MgH_2, after hydrogen loading (373 K/24 h). After hydrogen desorption at 433 K, the Mg was recovered. During hydrogenation at the same condition, (110) textured Nb was entirely transformed to orthorhombic NbH (O-NbH) with (111) texture (Fig. 5.3(b). As-deposited Mg 100 nm/Nb 100 nm multilayer (referred to as Mg/Nb 100 nm thereafter) has texture of Mg (0002) and Nb (110) (Fig. 5.3(c)). After hydrogen absorption a single peak was observed due to the overlap of O-NbH (111) and (200) textured O_m-MgH_2. Mg and Nb peaks nearly completely recovered after H_2 desorption. Similar phenomenon

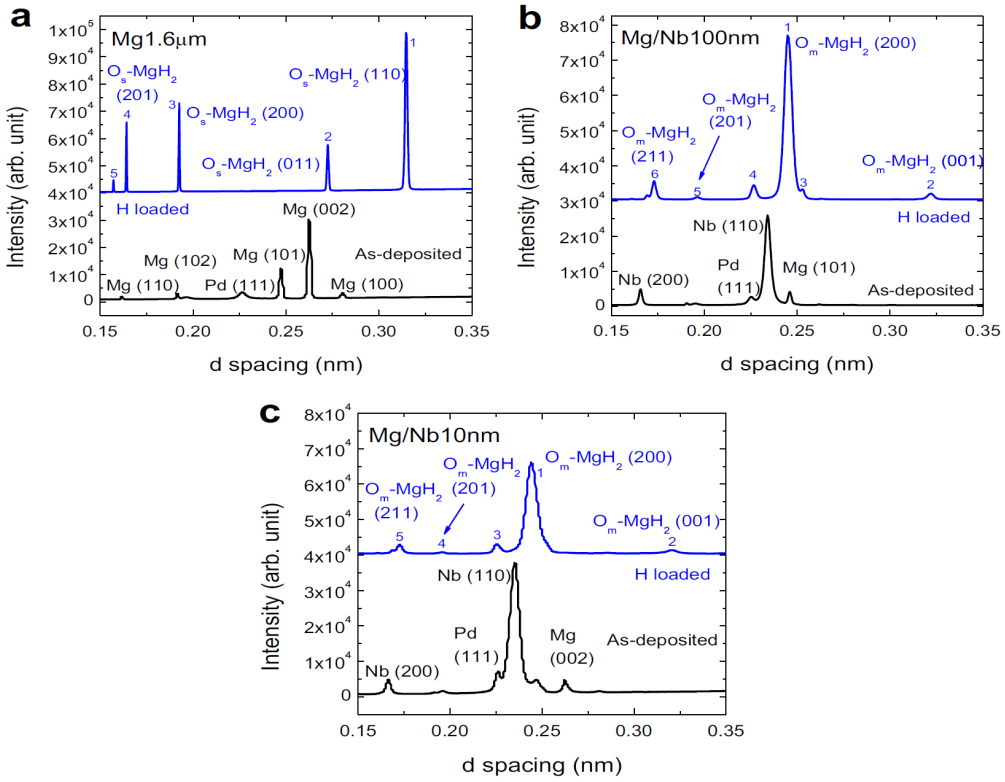

Figure 5.2: Synchrotron X-ray diffraction profiles of as-deposited and hydrogen loaded (a) Mg, (b) Mg/Nb 100 nm and (c) Mg/Nb 10 nm multilayers. After hydrogen loading (373 K/24 h), the single layer Mg films completely transformed to O_s-MgH_2 with strong (110) texture, whereas the multilayer films transformed to O_m-MgH_2 with (200) texture and O-NbH phase with (111) texture.

was observed during hydrogenation of Mg/Nb 10 nm multilayers (Fig. 5.3(d)). As reported in previous section, the orthorhombic-MgH_2 phases in both single layer and multilayer films have the same $CaCl_2$-type of structure, but their lattice parameters and texture were quite different. Fig. 5.3(e) compares the evolution of H pressure with temperature for all the hydrided films (on oxidized Si substrate) during TDS studies. In samples containing MgH_2, TDS spectra consist of intense peaks at 400 K or less, and much weaker peaks at ~523 K. In single layer MgH_2, H pressure reaches

a peak at ∼400 K. NbH films show a desorption peak at 373 K, close to that in bulk NbH (∼361 K) [196]. Multilayers loaded at 373 K/24 h start H_2 desorption at lower temperatures. When multilayers were loaded at lower temperatures (353 K/12 h), H_2 desorption takes place at room temperatures. To understand the effect of stress on H_2 sorption, three sets of specimens were studied (Fig. 5.3(f)). 30-μm thick Mg film on substrate shows a desorption peak at ∼393 K, similar to that of 1.6-μm thick MgH_2 films on substrate, whereas the free-standing 30-μm thick Mg film shows negligible H_2 desorption. Meanwhile the 10-μm thick, free-standing Mg/Nb 100 nm multilayers show a much stronger desorption peak at ∼373 K.

From experimental measurement, the significance of layer interface on kinetics is revealed by rapid desorption of H at room temperature in multilayers. Most of multilayers investigated in this work have shown H_2 sorption at ∼373 K. Some of them such as Mg/Nb 10 nm multilayers showed a desorption peak at 325 K. Layer interfaces act as high diffusivity pathways for rapid transport of hydrogen. Meanwhile, the interface may also play certain roles on destabilization of MgH_2 since a lower H_2 desorption temperature can be achieved in Mg/Nb multilayers with smaller individual layer thickness. This phenomenon might be related to the energetic contributions from interface and the diffusion of hydrogen in close proximity to layer interfaces.

5.4.2 Stress-induced formation of metastable orthorhombic-MgH_2 and its significant destabilization

Experimental measurements suggest the formation orthorhombic MgH_2 was induced by stress. The drastic difference in H_2 desorption between free-standing Mg films and those on substrate highlights the significance of stress. During H loading of bulk Mg, the lattice uniformly and linearly expands with hydrogen concentra-

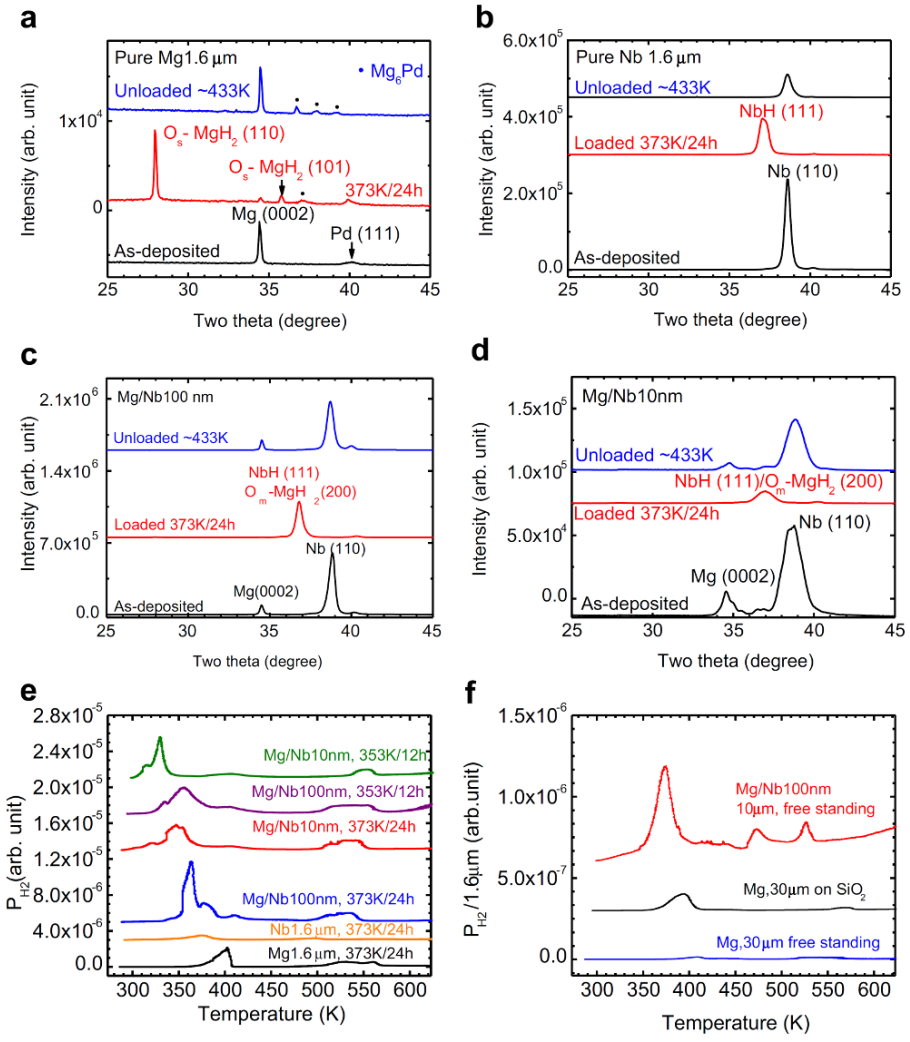

Figure 5.3: (a) XRD profile shows that hydrogen loading of Mg film (at 373 K/24 h) and unloading at 433 K. (b) Nb has undergone reversible phase transformation when hydrided at similar condition. Hydrogenation of (c) Mg/Nb 100 nm and (d) Mg/Nb 10 nm multilayers at the same condition. (e) TDS profiles of H_2 in various films shows multilayers had lower hydrogen desorption temperature than single layer films. Multilayers loaded at 353 K/12h had lower desorption temperature than those loaded at 373 K/24h. (f) Comparisons of TDS profiles show poor H_2 sorption in 30 μm thick, free-standing Mg films; whereas 30 mm thick Mg films on substrate had performance similar to those of 1.6 μm Mg film on substrate. The 10 μm thick free-standing Mg/Nb 100 nm films exhibit the best performance among three specimens.

tion [197]. However, the rigid substrate induced in-plane expansion of Mg films in an anisotropic way. XRD, neutron reflectivity and microscopy (not include here) show that during H_2 sorption, Mg lattice expands by ∼25% out-of-plane. It was postulated before that there will be 6% expansion along each in-plane direction [198, 199, 200]. Our analysis shows however that the formation of T-MgH_2 with <110> texture will involve significant anisotropic in-plane distortion (Fig. 5.4(a)), ∼15% in-plane expansion from Mg <01$\bar{1}$0> to T-MgH_2 <$\bar{1}$10>, and 6% contraction from Mg <2$\bar{1}\bar{1}$0> to T-MgH_2 <001>. Such significant in-plane distortions make it less likely to form T-MgH_2 especially when Mg films are attached to rigid substrates. The formation of O_s-MgH_2 is preferred because the magnitude of in-plane lattice distortion is much less, ∼13% expansion and 2% contraction in each corresponding direction (Fig. 5.4).

Stress also exists in free-standing Mg/Nb multilayers without the use of a rigid substrate. The rationale is as follows: hydrogenation leads to a 32.8% volume expansion in Mg (from 0.0233 nm^3 for a Mg atom to 0.0308 nm^3 for MgH_2), but only 13.8% volume expansion in Nb (from 0.0180 nm^3 for Nb to 0.0205 nm^3 for NbH). As Mg and Nb remain rigidly bonded through layer interfaces (as evidenced by retention of layer integrity), such a large difference in volume expansion (∼19%) must be accounted for by introducing significant compressive stress in MgH_2, and thus lead to the formation of O_m-MgH_2. There were speculations that stress at the Mg–Pd interface might assist H_2 sorption [201, 199, 200]. However Mg and Pd form several intermetallics, making it difficult to interpret the influence of stress on H_2 sorption, and the interface is thermodynamically unstable and significantly degrades during cyclic studies. Also the usage of Pd as a major constituent in Mg/Pd multilayers is economically prohibitive for H storage applications.

In this section, the DFT calculations were performed to investigate the thermodynamic stabilities of the observed orthorhombic MgH phases in thin-films. The

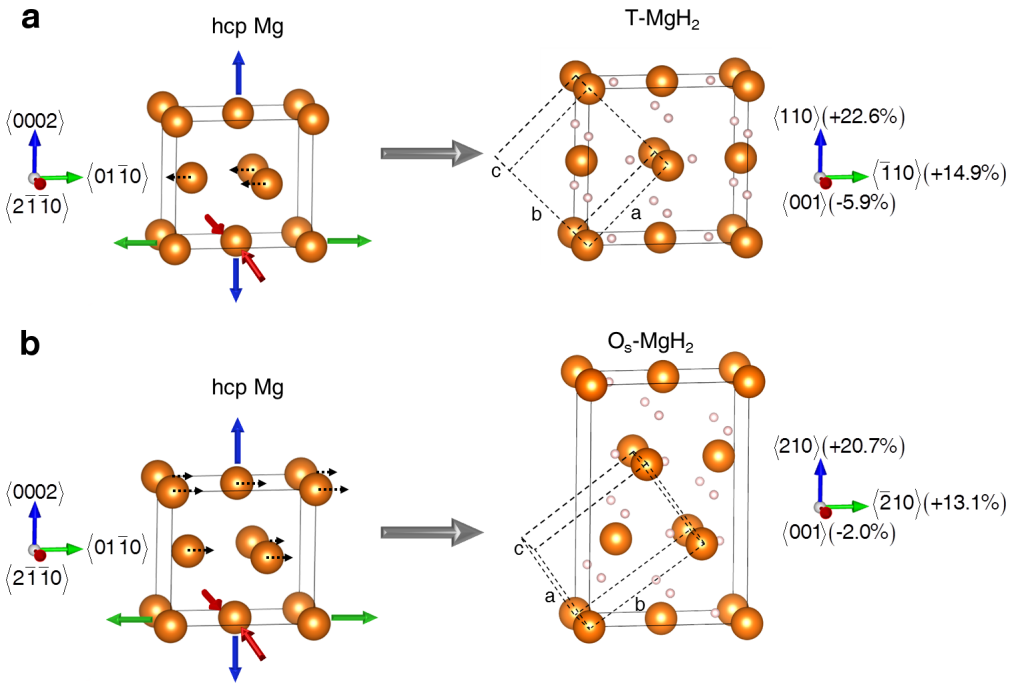

Figure 5.4: The transformation schematics of (a) hcp Mg to T-MgH_2 and (b) hcp Mg to O_s-MgH_2. The orientation relationships between hcp Mg and magnesium hydrides and the magnitude of lattice distortion are also shown. The conventional unit cells with a, b and c parameters of T-MgH_2 and O_s-MgH_2 are shown as transparent boxes connected by dash lines.

ΔH_f as a function of the crystal volume change were calculated for O_s-MgH_2, O_m-MgH_2, $CaCl_2$-type MgH_2 and T-MgH_2 structures. Their desorption temperatures were predicted by deriving Van't Hoff's equation (Eq. 1.3). In Fig. 5.5, the ΔH_f and estimated T_d as a function of volume change in both O_s-MgH_2 and O_m-MgH_2 structures, which are constrained along the in-plane direction reported in Table 5.2 and 5.4), are compared to those in the isotropic expansion/contraction of the (bulk) rutile-type MgH_2 and the $CaCl_2$-type MgH_2 structures. The calculated results are reported in Table 5.4.2. Volume variation (either expansion or contraction) can lead

to significant reduction of the desorption temperature which is observed in Fig. 5.5.

Calculated ΔH_f of the T-MgH_2 and the unconstrained $CaCl_2$-type MgH_2 are kJ/mol·H_2 and -57.4 kJ/mol·H_2, respectively. Therefore, the $CaCl_2$-type MgH_2 structure is indeed the metastable phase of MgH_2 being a bit higher in its energy compared to that in T-MgH_2. Under isotropic volume change, T-MgH_2 and $CaCl_2$-type MgH_2 have nearly identical temperature dependent variations of ΔH_f and T_d. Vajeeston *et al.* [195] showed theoretically that high pressure can induce phase transformation from stable T-MgH_2 to O-MgH_2 with $CaCl_2$ prototype. Though metastable in nature, it is energetically feasible that the $CaCl_2$-type structure can be stabilized in thin films by stresses.

Due to the significant distortion induced by substrate in single layer Mg case, ΔH_f increases by ∼26 kJ/mol·H_2 and T_d reduce by ∼200 K compared to those in T-MgH_2. The desorption temperature of O_s-MgH_2 (the open triangle point in Fig. 5.5) is in good agreement with the experimental observations (the partial filled triangle point in Fig. 5.5). For O_m-MgH_2, the structure is about 3% volume contraction form the T-MgH_2. Its calculated ΔH_f is enhanced by 15.5 kJ/mol·H_2 and corresponding T_d value is ∼458 K as shown in Fig. 5.5 and Table 5.4.2. The calculation overestimates the desorption temperature in multilayer case as the role of interfacial energy on the thermodynamic stability of MgH_2 and other effects (i.e. the catalytic effect from Nb and etc.) have not been considered.

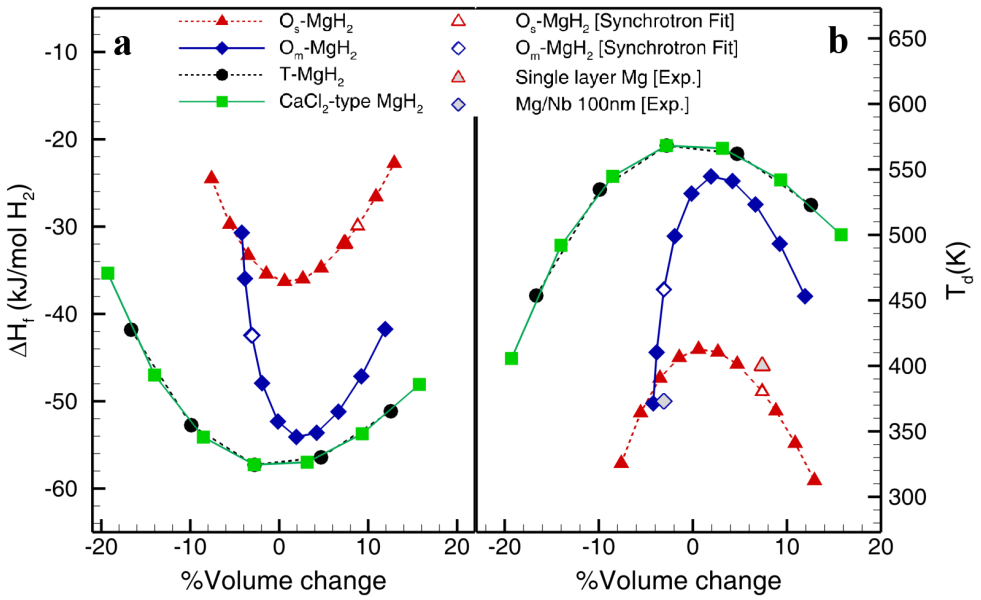

Figure 5.5: Comparison of (a) calculated ΔH_f and (b) estimated T_d as a function of volume change in O_s-MgH_2, O_m-MgH_2, T-MgH_2 and $CaCl_2$-type of O-MgH_2 (all systems were subjected to isotropic volume change). Experimental values of T_d are shown as partially filled open symbols. Open symbols represent the calculated results based on experimentally measured lattice parameters. Volume changes lead to significant destabilization of MgH_2.

Table 5.5: The structural parameters (a, b and c) in nm, volume (V) of unit cell in nm^3/f.u., volume change compared to T-MgH_2 (ΔV) in % , the formation enthalpy (ΔH_f) in kJ/mol·H_2, the formation enthalpy difference ($\Delta H_f^{dif} = \Delta H_{f(O-MgH_2)} - \Delta H_{f(T-MgH_2)}$) in kJ/mol·$H_2$ and estimated desorption temperature (T_d) in ^{o}C for the T-MgH_2 , the CaCl2-type MgH_2, the Os-MgH_2, and the Om-MgH_2 models.

	Lattice Parameters (nm)			V	ΔV	ΔH_f	ΔH_f^{dif}	T_d
	a	b	c	(nm^3/f.u.)	(%)	(kJ/mol·H_2)	(kJ/mol·H_2)	(K)
T-MgH_2								
Cal.	0.4475	0.4475	0.2998	0.0300		-58.0		
Exp.	0.4517	0.4517	0.3020	0.0308				
$CaCl_2$-type MgH_2								
Cal.	0.4480	0.4465	0.2999	0.0300		-57.4		
Cal. [195]	0.4481	0.4466	0.3006	0.0301				
Single layer case:O_s-MgH_2 (a and b are fixed, only c is varied.)								
c change (%)								
-10	0.3851	0.5464	0.2706	0.0285	-7.6	-24.5	33.434	325
-8	0.3851	0.5464	0.2766	0.0291	-5.55	-29.7	28.214	364
-6	0.3851	0.5464	0.2826	0.0297	-3.5	-33.3	24.645	390
-4	0.3851	0.5464	0.2886	0.0304	-1.44	-35.4	22.512	406
-2	0.3851	0.5464	0.2946	0.0310	0.61	-36.3	21.671	412
0	0.3851	0.5464	0.3006	0.0316	2.66	-36	21.955	410
2	0.3851	0.5464	0.3067	0.0323	4.72	-34.7	23.2	401
4.59	0.3851	0.5464	0.3144	0.0331	7.37	-31.9	26.006	380
6	0.3851	0.5464	0.3187	0.0335	8.82	-29.9	28.018	366
8	0.3851	0.5464	0.3247	0.0342	10.88	-26.6	31.361	341
10	0.3851	0.5464	0.3307	0.0348	12.93	-22.8	35.197	312

Continued on next page...

Table 5.5 – *Continued*

	Lattice Parameters (nm)			V	ΔV	ΔH_f	ΔH_f^{dif}	T_d
	a	b	c	(nm^3/f.u.)	(%)	(kJ/mol·H_2)	(kJ/mol·H_2)	(K)
Multilayer case: O_m-MgH_2 (a is fixed, while b and c are varied)								
b change (%)								
-20	0.49028	0.35726	0.33699	0.0295	-4.21	-30.7	27.242	371
-18	0.49028	0.36619	0.32999	0.0296	-3.85	-36	21.987	410
-15.16	0.49028	0.37889	0.3215	0.0299	-3.08	-42.4	15.5	458
-12	0.49028	0.39298	0.31364	0.0302	-1.93	-47.9	10.008	499
-8	0.49028	0.41084	0.30548	0.0308	-0.14	-52.3	5.623	532
-4	0.49028	0.42871	0.29881	0.0314	1.93	-54.1	3.854	545
0	0.49028	0.44657	0.29328	0.0321	4.21	-53.6	4.327	541
4	0.49028	0.46443	0.28862	0.0329	6.66	-51.2	6.743	523
8	0.49028	0.4823	0.28465	0.0337	9.24	-47.2	10.797	493
12	0.49028	0.50016	0.28124	0.0345	11.92	-41.7	16.204	453

In summary, DFT simulations indicate that either volume expansion or contraction will lead to destabilization of MgH_2. But volume expansion and contraction may have asymmetrical impact on destabilization of MgH_2. For instance, contraction appears more effective to reduce desorption temperature of O_m-MgH_2. Volume change can presumably change the local bonding strength between Mg and H ions and thus affect the stability of MgH_2. Second, to destabilize MgH_2, stress can be introduced by selection of a second phase which has large volume expansion incompatibility compared to Mg. The magnitude of stress shall scale with the degree of mismatch between volume expansion of Mg and the second phase. A large number of candidates are available to tailor the sign and magnitude of stress in MgH_2. Third, immiscibility between Mg and the second phase may be critical to achieve structural integrity of the multilayers. Interfaces in miscible systems are typically unstable during hydrogen sorption at elevated temperatures. Immiscible interfaces are preferred to achieve high temperature thermal stability and mechanical stability against multiple cyclic loadings.

5.5 Conclusion

In conclusion, stress-induced metastable orthorhombic-MgH_2 (O-MgH_2) phases were observed in this work. The drastic destabilization of Mg hydride induced by the formation of a mestastable variant with orthorhombic symmetry opens up abundant opportunity for the selection of appropriate second phases to design and manufacturing Mg nanocomposite with advanced H storage performance. The destabilization was triggered by the formation of distorted metastable O-MgH_2 phases induced by stresses. Stresses arise from either substrate constraint or volume expansion incompatibility. Under thin film environment, O-MgH_2 is preferred over T-MgH2 as it induces less lattice distortion crystallographically during phase transformation. DFT

calculations agree qualitatively well with experimental observations. Size effect and layer interface also play an important role to expedite the H_2 sorption kinetics in MgH_2. These studies provide important design criteria for selection of appropriate second phase to destabilize Mg hydride. The concept of stress-assisted H_2-sorption developed here also has general implications for the design of other metal hydrides and chemical hydrides.

6. THERMODYNAMIC AND MECHANICAL PROPERTIES OF MG AND NB HYDRIDES

6.1 Introduction

According to the discussions in the previous chapter, the stress induced metastable orthorhombic-MgH_2 (O_m-MgH_2) was observed in hydrided Mg/Nb multilayers. The formation of this phase leads to a drastic destabilization of Mg hydride in Mg/Nb multilayers. In this chapter, the hydride structures observed in Mg/Nb multilayers, O-NbH, O_m-MgH_2 and T-MgH_2, were additionally investigated. Selected properties such as the elastic, thermodynamic and energetic properties of those hydrides were elucidated by computational methods.

6.1.1 Mechanical and ground state properties calculated by DFT calculations

Hydrogen has a huge effect on mechanical properties of metals and their alloys. For example, their ductilities are degraded by hydrogen. Most metals become more brittle when they form metal hydrides [202]. From those reasons, the mechanical properties of metal hydrides are difficult to measure experimentally, but can be estimated using computational methods. In this study, the elastic stiffness constants (C_{ij}) were calculated based on the stress-strain method [150]. A set of strains are applied to a lattice resulting in a set of distorted structures. Using DFT calculations, the set of stresses can be obtained from the change of energies due to the lattice deformations. Then the C_{ij} values can be evaluated by using the generalized Hook's law. Many elastic properties corresponding to a random polycrystalline arrangement, such as the bulk modulus (B) and the shear modulus (G), can be evaluated from C_{ij} values by using the Voigt-Reuss-Hill (VRH) approach [203, 204].

The bulk and shear moduli of the hcp Mg lattice are calculated by the following

equations:

$$B = \frac{1}{9}[2(C_{11} + C_{12}) + 4C_{13} + C_{33}], \tag{6.1}$$

$$G = \frac{1}{30}[C_{11} + C_{12} + 2C_{33} - 4C_{13} + 12C_{44} + 12C_{66}]. \tag{6.2}$$

The mechanical criteria for stability in hexagonal structures are given by

$$C_{44} > 0,\ C_{11} > |C_{12}|,\ (C_{11} + 2C_{12})C_{33} > 2C_{13}^2. \tag{6.3}$$

For the bcc Nb, its bulk and shear moduli can be estimated by the following equations:

$$B = \frac{(C_{11} + 2C_{12})}{3}, \tag{6.4}$$

$$G = \frac{(C_{11} - C_{12} + 3C_{44})}{5}. \tag{6.5}$$

The mechanical criteria of the cubic phase are given by

$$C_{11} > 0,\ C_{44} > 0,\ C_{11} > |C_{12}|,\ (C_{11} + 2C_{12}) > 0. \tag{6.6}$$

For the tetragonal MgH_2 structure, the bulk and shear moduli are estimated by:

$$B = \frac{1}{9}[2(C_{11} + C_{12}) + C_{33} + 4C_{13}], \tag{6.7}$$

$$G = \frac{1}{30}(M + 3C_{11} - 3C_{12} + 12C_{44} + 6C_{66}),$$
$$M = C_{11} + C_{12} + 2C_{33} - 4C_{13}, \tag{6.8}$$

For the tetragonal lattices, the mechanical criteria are given by

$$\begin{aligned} C_{11} > 0,\, C_{33} > 0,\, C_{44} > 0,\; C_{66} > 0, \\ C_{11} - C_{12} > 0,\, C_{11} + C_{33} - 2C_{13} > 0, \\ 2(C_{11} + C_{12}) + C_{33} + 4C_{13} > 0. \end{aligned} \tag{6.9}$$

The bulk and shear moduli of the orthorhombic NbH lattice are estimated by the following equations:

$$B = \frac{1}{9}[C_{11} + C_{22} + C_{33} + 2(C_{12} + C_{13} + C_{23})], \tag{6.10}$$

$$G = \frac{1}{15}[C_{11} + C_{22} + C_{33} + 3(C_{44} + C_{55} + C_{66}) - (C_{12} + C_{13} + C_{23})]. \tag{6.11}$$

For the orthorhombic lattices, the mechanical criteria are given by

$$\begin{aligned} C_{11} > 0,\, C_{22} > 0,\, C_{33} > 0,\, C_{44} > 0,\, C_{55} > 0,\; C_{66} > 0, \\ C_{11} + C_{22} + C_{33} + 2(C_{12} + C_{13} + C_{23}) > 0, \\ C_{11} + C_{22} - 2C_{12} > 0,\, C_{11} + C_{33} - 2C_{13} > 0, \\ C_{22} + C_{33} - 2C_{23} > 0. \end{aligned} \tag{6.12}$$

The Youngs modulus (Y) and Poissons ratio (ν) can be calculated by the following equations:

$$\begin{aligned} Y = 9BG/(3B + G), \\ \nu = (3B - 2G)/[2(3B + G)] \end{aligned} \tag{6.13}$$

In addition, the formation energy of each hydride $\Delta E_f(MH_n)$ were investigated

in this work. The $\Delta E_f(MH_n)$ is given by the following equation:

$$\Delta E_f(MH_n) = E(MH_n) - E(M) - nE(H) \tag{6.14}$$

where $E(MH_n)$, $E(M)$ and $E(H)$ are total energies of a hydride structure and metal and hydrogen atoms, respectively. n denote the number of hydrogen atoms.

6.1.2 Finite temperature thermodynamics

From basic statistical mechanics, the Helmholtz free energy (F) relates to the partition function (Z) as expressed in the following form:

$$F = -k_B T ln Z \tag{6.15}$$

where k_B and T are the Boltzmann constant and temperature, respectively. From this equation, finite temperature thermodynamic quantities (i.e. the internal energy (U), the entropy (S) and the heat capacity at constant pressure can be calculated by differentiating F with respect to T. For a non-magnetic perfect structure with an average atomic volume (V), its total free energy at temperature T is:

$$F(V,T) = E_0(V) + F_{vib}(V,T) + F_{el}(V,T) \tag{6.16}$$

where $E_0(V)$ is the ground state energy at 0K. $F_{vib}(V,T)$ the vibrational free energy and $F_{el}(V,T)$ is the electronic free energy [205, 206]. The first energy term can be calculated by using the DFT method.

The vibrational contributions, expressed in the second term, can be obtained from the harmonic approximation is given by [207]:

$$F_{vib}(T) = k_B T \int_0^\infty ln[2sinh(\frac{h\nu}{2k_B T}d\nu)] \tag{6.17}$$

where the frequencies of the phonon modes and the phonon density of states (DOSs) are denoted by ν and $g(\nu)$, respectively. h is Plancks constant. Practically, the phonon DOSs can be obtained by the lattice dynamic calculations (e. g. the linear response and the supercell methods) introduced in Chapter 2.

However, thermal expansion affects the vibrational properties of materials at higher temperature. The harmonic approximation does not include this effect. The quasi-harmonic correction is the extension of the harmonic approximation which includes that effect. In this method, the volume dependence of phonon DOSs are resulted from the forces-constant tensors become volume dependent properties. The quasi-harmonic calculation can be performed by calculating the simple harmonic calculations at several volumes. As a result, $F_{vib}(V,T)$ can be obtained. The thermodynamic Grüneisen parameter (γ) indicates the lattice anharmonicity due to volume expansion of the system. Moreover, some intrinsic anharmonic effects can be included in F_{vib} at elevated temperatures [208, 209].

The temperature dependence of the free energy term per atom can be calculated from [207]:

$$\frac{F(T)}{N} = \frac{F(T,V_0)}{N} - \frac{3k_B T\bar{\gamma})^2}{2B(V_0/N)} \tag{6.18}$$

B denotes the isothermal bulk modulus and V_0 is the equilibrium volume.

Lastly, the electronic contribution of the total free energy, $F_{el}(V,T)$, is given by

$$F_{el}(V,T) = E_{el}(V,T) - TS_{el}(V,T) \tag{6.19}$$

$$E_{el}(V,T) = \int n(\epsilon,V) f\epsilon d\epsilon - \int^{\epsilon} n(\epsilon,V)\epsilon d\epsilon \tag{6.20}$$

$$S_{el}(V,T) = -k_B \int n(\epsilon,V)[flnf + (1-f)ln(1-f)]d\epsilon \tag{6.21}$$

where E_{el} and Sel are the energy of the electrons and the electronic entropy, respectively. $n(\epsilon, V)$ is the electronic DOSs at a individual quasi-harmonic volume. the Fermi function is signified by f [206].

Then, the full free energy can be obtain by including all above contributions and thermodynamic properties can be calculated as mentioned previously.

6.2 Computational procedure

DFT calculations were used in this study. The generalized gradient approximation (GGA) refined by Perdew, Burke and Ernzerhof (PBE) [210] with projector augmented-wave(PAW) pseudo-potentials [82] was employed. The plan wave cutoff is 325 eV and 350 eV for NbH and O_m-MgH_2, respectively. A Monkhorst-Pack mesh with at least 5000 k-points per reciprocal atom was used for k-point sampling in the Brillouin zone. The Alloy Theoretic Automated Toolkit (ATAT) package [211] was used for calculating thermodynamics properties of these hydrides. The lattice dynamical properties were obtained from the supercell approach. Elastic and finite-temperature thermodynamic properties of those hydrides were calculated by using the quasiharmonic approximation approach with the anharmonic- and electronic contributions. For the quasi-harmonic approximation, harmonic calculations of each individual seven volumes were performed. These seven volumes are in range of -2% to 4% of the equilibrium volume of the hydride structure.

6.3 Results and discussion

6.3.1 Ground-state properties

The NbH structure has the Pnnn (#48) space group. This O-NbH phase is a face centered orthorhombic filled with H atoms at four tetragonal interstitial sites. O_m-MgH_2 has the $CaCl_2$ type structure, which is the Pnnm space group. T-MgH_2 crystal is the P42/mnm (#136) space group. Three dimensional structures of these three structures are presented in Fig. 6.1. Lattice parameters, calculated from the 0K calculations, are provided in Table 6.3.1. The calculated lattice parameters of O-NbH and T-MgH_2 provide similar values with the experimental data [212, 213]. Moreover, ΔE_f of those hydrides were calculated by changing molar volume, isotropically. The O-NbH phase is more stable than both of MgH_2 phases. The orthorhombic MgH_2 is less stable than the tetragonal MgH_2 phase.

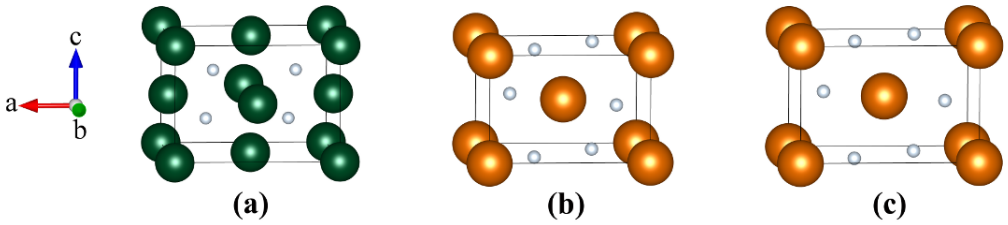

Figure 6.1: Three dimensional structures of (a) O-NbH, (b) T-MgH_2 and (c) O_m-MgH_2

6.3.2 Elastic properties of NbH and MgH_2

The mechanical properties of Nb- and Mg-hydrides were determined in this part. The calculated C_{ij} values can be achieved and used for estimating other mechanical properties. The calculated elastic properties are reported in Table 6.2. All hydride

Table 6.1: Structural properties of O-NbH, T-MgH_2 and O_m-MgH_2 calculated by using PAW-PBE method

			a(Å)	b(Å)	c(Å)	V(Å^3/f.u.)
O-NbH	(Pnnn)	Cal.	4.939	4.859	3.496	20.97
		Exp.[a]	4.84	4.90	3.45	20.46
T-MgH_2	(P4_2/mnm)	Cal.	4.471	4.471	2.997	29.95
		Exp.[b]	4.517	4.517	3.020	30.81
O_m-MgH_2	(Pnnm)	Cal.	4.903	3.779	3.215	29.86

[a][212], [b][213]

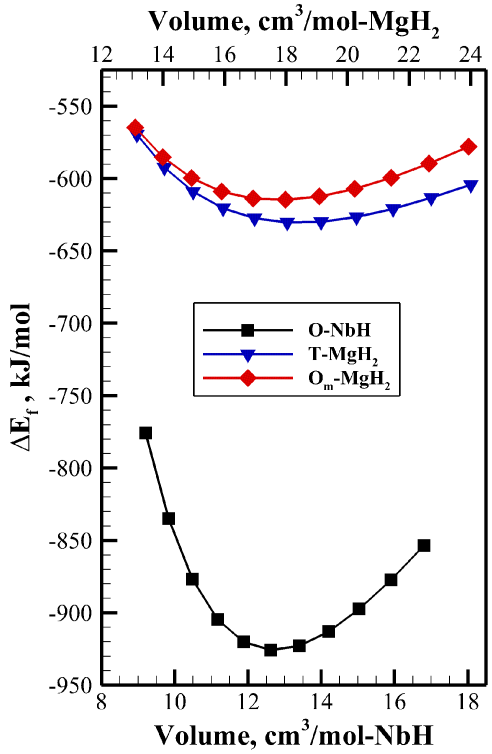

Figure 6.2: Calculated ΔE_f as a function of volume of O-NbH, T-MgH_2 and O_m-MgH_2

structures are mechanical stable based on the the mechanical stability criteria. As a result, Nb is more strength than Mg in both pure and hydrided phases. In Mg and Nb lattices, the calculated values are similar to the values measured by experiments[214, 215, 151]. These results ensure that the predicted mechanical properties of hydride phases are reliable. All three hydrides are stronger than their pure phases. The mechanical properties (B, G and Y) of O_m-MgH_2 are in range of 5%-10% lower than those of T-MgH_2. Therefore, the difference in mechanical strength between O-NbH and O_m-MgH_2 is larger than that of the O-NbH and T-MgH_2 case. This may be one of the sources of stress that induces destabilization of Mg hydride in Mg/Nb multilayers. In contrast, the mechanical values of Pd hydride (PdH_x) decreases when hydrogen content increases [216, 217]. The Y of pure Pd is 112.4 GPa [218] and it decreases to 95.9 GPa after forming PdH(x=1) [216].

Table 6.2: Elastic Properties of bulk bcc Nb, bulk hcp Mg, O-NbH, T-MgH_2 and O_m-MgH_2. Calculations were performed under the PAW-PBE calculations.

		C_{11}	C_{12}	C_{13}	C_{22}	C_{23}	C_{33}	C_{44}	C_{55}	C_{66}	B	G	Y	ν
bcc Nb	Cal.	252.6	140.0					15.5			177.6	31.8	90.1	0.42
	Exp.(4.2K)[a]	252.7	133.2					30.97			173.0	42.5	117.8	0.39
	Exp.(300K)[b]	246.5	134.5					28.73			171.8	39.6	110.4	0.39
hcp Mg	Cal.	68.6	23.6	17.8			73.4	17.1		22.5	36.6	21.4	53.8	0.25
	Exp.(0K)[c]	63.48	25.94	21.70			66.45	18.42		18.75	36.89	19.39	49.49	0.28
	Exp.(300K)[c]	69.40	25.61	21.44			61.60	16.40		16.90	35.24	17.40	44.83	0.29
O-NbH	Cal.	295.4	189.4	116.1	284.2	129.0	251.3	62.0	56.1	76.3	188.9	65.3	175.7	0.34
T-MgH_2	Cal.	74.4	38.8	31.4			136.0	37.6		53.0	54.2	37.8	92.1	0.22
	GGA[d]	73.1	33.9	20.4			131.9	38.5		52.3	50.2	36.1	87.3	
	LDA[d]	77.3	39.2	32.6			138.9	40.2		56.3	54.5	37.4	91.2	
O_m-MgH_2	Cal.	91.4	32.0	33.1	55.5	34.2	95.4	46.8	33.0	51.3	49.0	35.8	86.3	0.21

[a][214] The experimental data was obtained by an ultrasonic pulse technique.
[b][215]The elastic constants were measured by a high-frequency ultrasonic cw resonance technique.
[c][151] The adiabatic elastic constants of single cystal Mg measured by an ultrasonic pulse technique. The values at 0K are extrapolated values.
[d] [219] DFT calculations

6.3.3 Finite-temperature properties

The finite temperature calculations were done by using the quasiharmonic approximation approach with the anharmonic- and electronic contributions. Properties of simulated hydrides calculated at 0 K and 298 K are compared in Table 6.3.3. At 298 K, the calculated B values of bcc Nb (170.8 GPa) has a good agreement with the 171.8 GPa of experimental value (measured at 300K) [215]. In case of hcp mg, the calculated B is comparable to the experimental value (35.24 GPa) [151].

Next, selected properties at finite temperature of Nb- and Mg-hydrides were determined up to 1000 K. The calculated C_p, TEC, B and V as a function of temperature of O-NbH, T-MgH_2 and O_m-Mg_2 are compared and displayed in Fig. 6.3(a) to 6.3(d), respectively. In Fig. 6.3(a), C_p values of both MgH_2 structures are similar, while O-NbH has lower C_p value compared to those of Mg hydrides. The different in C_p between O-NbH and MgH_2 increases when temperature increases. Comparison of TEC values is shown in Fig. 6.3(b). Similarly, TEC values expose the similar trend observed in C_p. When temperature is higher than $\sim$ 100K, the TEC of MgH_2 structures change gradually. TEC values of O_m-Mg_2 are higher than those in T-MgH_2. In Fig 6.3(c), the calculated bulk moduli indicate that O-NbH is about three times stronger than both of MgH_2 phases. In all cases, B values is decreased when temperature increases. In Fig. 6.4(d), the atomic volumes of both MgH_2 phases expand as temperature increases. For NbH, the change in V is smaller than that in MgH_2. Thermodynamic properties, which are enthalpy (H), free energy (F) and entropy (S), as a function of temperature of O-NbH, T-MgH_2 and O_m-Mg_2 are shown in Fig. 6.4(a) to 6.4(c).

Table 6.3: Properties at 0 K and 298 K of bcc Nb, hcp Mg, O-NbH, T-MgH_2 and O-MgH_2 by using the quasi-harmonic approximation approach with the anharmonic- and electronic-contributions. V and E are the equilibrium atomic volume and the total energy per atom, respectively. B and B' are the isothermal bulk modulus and the pressure derivative of bulk modulus, respectively. γ is the Grüneisen parameter. S is the entropy. C_p is the constant pressure specific heat capacity. TEC is the thermal expansion coefficient.

T	Properties	Nb	Mg	O-NbH	T-MgH_2	O_m-MgH_2
0 K	V (Å^3)	18.36	23.18	10.71	10.60	10.19
	E ($\times 10^2 kJ/mol$·atom)	-9.70	-1.50	-6.58	-2.72	-2.67
	B (GPa)	170.80	36.02	172.51	43.90	47.79
		(173.0) [a]	(36.89[c])		(50.2[c])	
	B'	3.98	4.67	4.206	3.661	3.706
	γ	2.00	1.53	1.32	0.76	0.80
298 K	V (Å$^3/atom$)	18.48	23.56	10.74	10.64	10.23
	B (GPa)	166.10	32.91	167.26	41.50	45.94
		(171.8 [b])	(35.24[c])			
	B'	4.01	4.54	4.31	3.99	3.62
	γ	2.03	1.57	1.32	0.77	0.81
	S (J/mol/K)	37.07	33.36	17.06	11.66	12.54
	C_p(J/K/mol)	25.46	24.86	26.63	36.86	38.32
	TEC ($\times 10^{-6} 1/K$)	9.42	26.96	6.11	8.25	10.18

[a] [214] The experimental data was obtained by an ultrasonic pulse technique.
[b] [215]The elastic constants were measured by a high-frequency ultrasonic cw resonance technique.
[c] [151] The adiabatic elastic constants of single cystal Mg measured by an ultrasonic pulse technique. The values at 0K are extrapolated values.
[d] [219] DFT(PAW-GGA) calculations

6.4 Conclusion

The mechanical and finite temperature properties of O-NbH, T-MgH_2, O_m-MgH_2 and their non-hydrided phases were compared. From the calculated elastic proper-

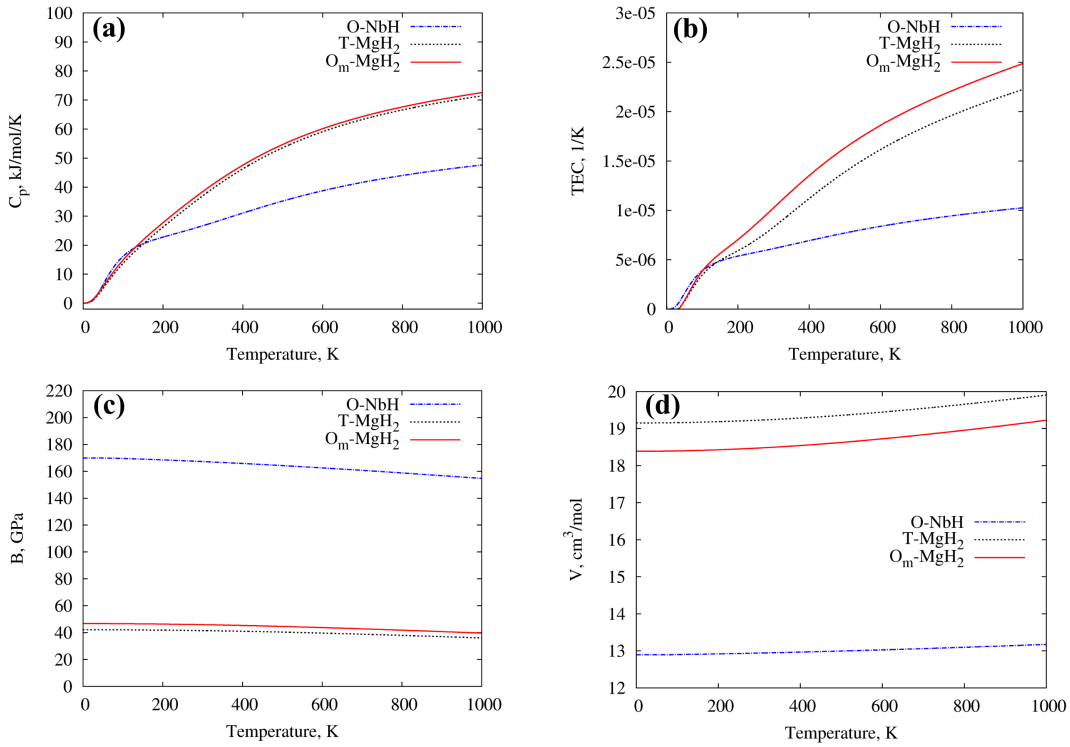

Figure 6.3: (a) The constant pressure specific heat capacity C_p, (b) the thermal expansion coefficient (TEC), (c) the bulk modulus (B) and (d) the molar volume (V) as a function of temperature of O-NbH, T-MgH_2 and O_m-MgH_2

ties, Nb and O-NbH are much stronger than Mg and MgH_2. Both mechanical properties and difference in volume expansion of Mg and Nb hydrides support the concepts of stress effect and large volume expansion incompatibility in Mg/Nb multilayers discussed in the previous chapter.

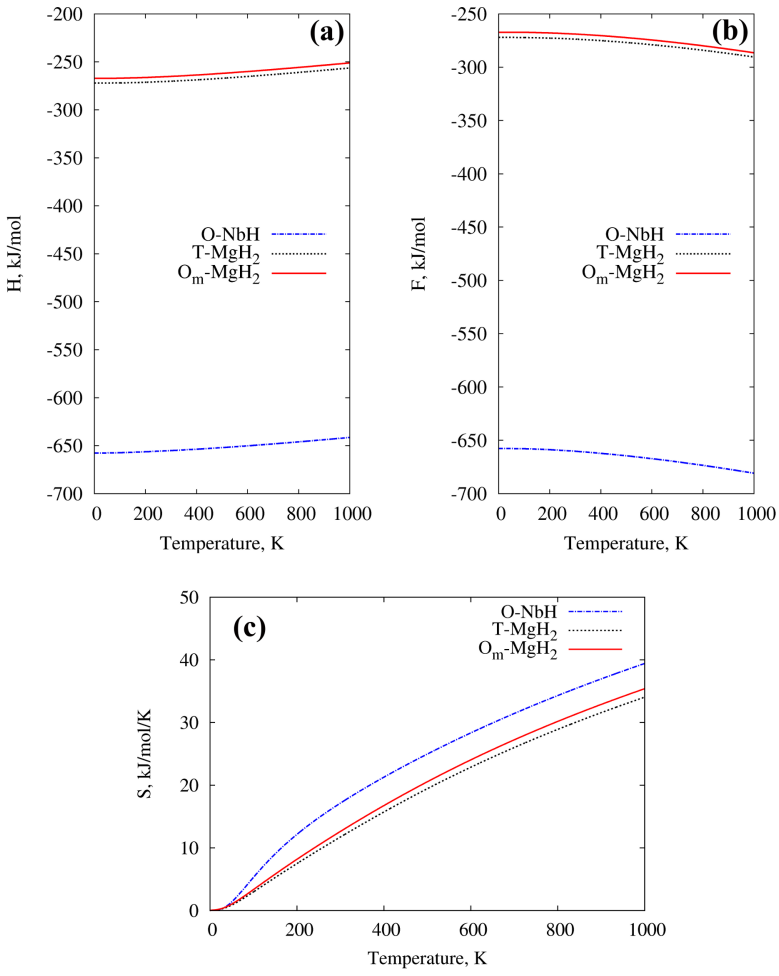

Figure 6.4: Finite-temperature thermodynamic properties (a) enthalpy (H), (b) free energy (F) and (c) entropy (S) as a function of temperature of O-NbH, T-MgH_2 and O_m-MgH_2

7. HYDROGEN DIFFUSION IN MG/NB MULTILAYERS

7.1 Introduction

In the past decade, hydrogen diffusion in metals has been limitedly examined by experimental measurements. On the other hand, computational tools have been widely used in this field of study [220, 221, 222]. Hydrogen adsorption on metal surfaces and hydrogen diffusion inside the metallic matrix have been studied theoretically [71, 223, 224]. In the Mg case, the dissociation of H_2 on a Mg(0001) surface was studied [71, 225, 226, 227]. In hcp Mg, there are four different adsorption sites called the top-, bridge-, fcc- and hcp-sites. The bridge site is reported as the favored position for splitting H_2 on a Mg(0001) surface. This H_2 dissociation process requires to overcoming an activation barrier (ΔE_a) of $\sim$0.4 eV-0.5 eV [71, 225, 226]. Diffusion of H atoms from the fcc site through the fcc-channel was studied [71]. Diffusion of H atoms in the group five metals, including bcc Nb, was investigated by Abound *et al.*

In general, a potential energy surface (PES) describes the energy of the systems as a function of their conformations. An example of three dimensional PES and its projected two dimensional PES are schematically represented in Fig. 7.1(a). The reaction path is shown in this figure. A transition state (TS) locates along the minimum energy path (MEP) connecting two local minima. From the past, several methods such as the Drag method, the Nudged Elastic Band (NEB) method, the Conjugated Peak Refinement (CPR) method, the Ridge method and the Dimer method have been proposed for finding the TS along the reaction paths [228]. The NEB method [229, 230] has been widely used in plane-wave DFT calulations. The Climbing Image NEB (CI-NEB) method was developed later for improving the typical NEB method [231]. Fig. 7.1(b) shows three movable images located between fixed

starting (R) and fixed ending (P) points. Those images are connected by springs. At the beginning, a straight is interpolated between R and P. During the relaxation of those images, the component of the spring force is kept parallel to the path and the component of true force is kept perpendicular to the path. The CI-NEB method was used in this work for determining the H diffusion mechanism in Mg-thin films.

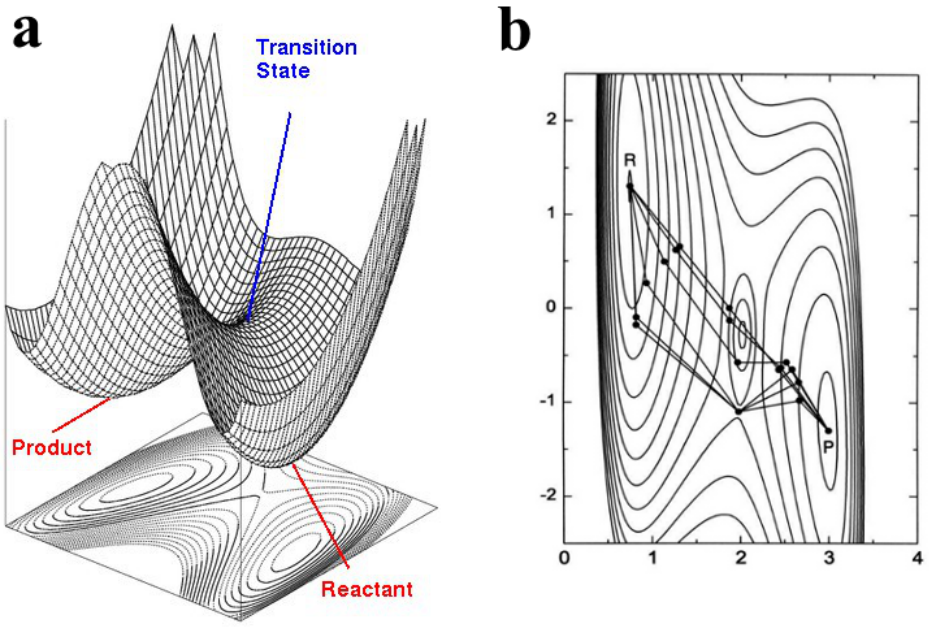

Figure 7.1: The schematics represent (a) the PES and (b) CI-NEB method [228]

7.2 Experimental observation

According the investigation of H sorption properties in Mg-based thin films discussed in chapter 5, the sequence of forming and releasing hydrogen in Mg/Nb multilayers was further investigated. The experimental procedures are given in chapter 5. Fig 7.2 shows XRD diffractions of Mg/Nb 100 nm after loading and unloading pro-

cesses. Apparently, d(111) peak of NbH presents first after loading H_2 about 10 minutes. After 12 hours, both O-NbH and O_m-MgH_2 are formed. When processed backwards, MgH_2 releases hydrogen first and d(0002) of Mg can be detected. Eventually, both Mg and Nb are fully recovered.

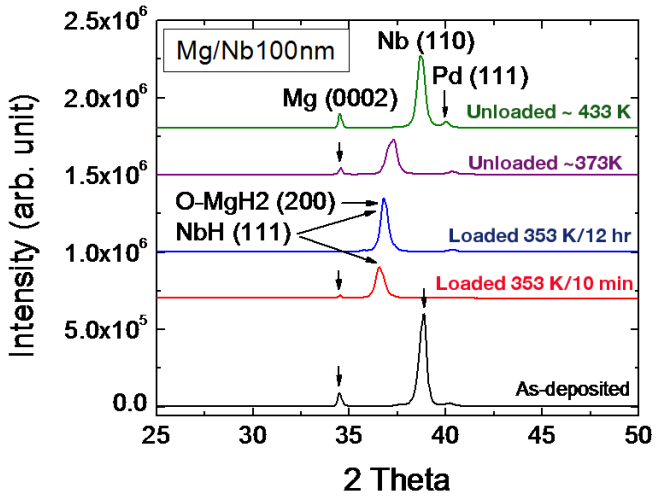

Figure 7.2: XRD profiles of Mg/Nb 100nm after 10 minutes of H_2 loading at 353 K (a red line), after 12 hours loading at 353 K (a blue line), after unloading at 373 K (a purple line) and after unloading at 473 K (a green line).

Furthermore, the origins of two desorption peaks (362 K and 378 K) in TDS spectrum of hydrided Mg/Nb 100 nm shown in Fig. 5.3(e) were also explored. XRD profiles were collected by interrupting desorption in between the two peaks. Fig. 7.3 shows that unloading at 373 K leads to the recovery of Mg, but NbH remains. Thus, the first desorption peak of Mg/Nb 100 nm (373 K/24 h) in Fig. 5.3(e) relates to H_2 desorption of O_m-MgH_2. Desorption at 433 K led to complete recovery of

as-deposited states. Similarly, in hydrided Mg/Nb 10 nm multilayers, desorption occurred first from O_m-MgH_2 at 348 K, followed by recovery of Nb phase. Clearly, both of them exhibit the same aspect that H is released from Mg layer first.

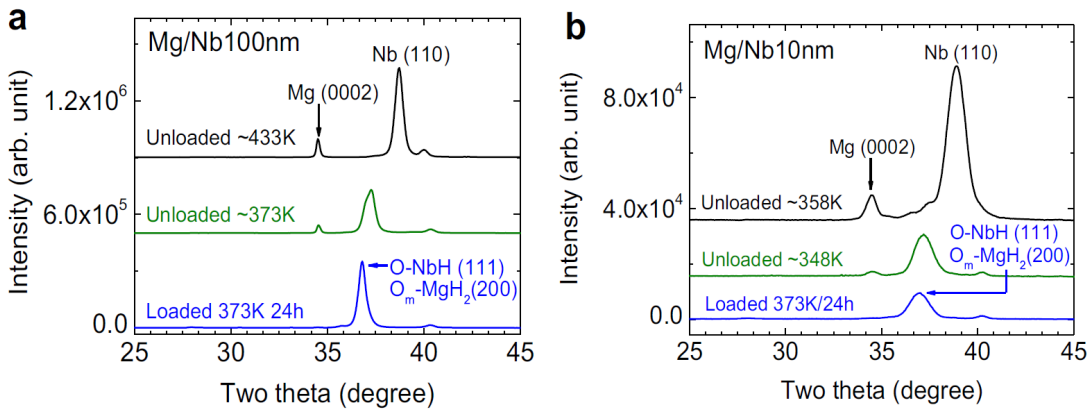

Figure 7.3: XRD experiments to probe phase transformations revealed from TDS experiments in Fig. 5.3(e). (a) After H_2 desorption of hydrided Mg/Nb 100 nm at 373 K. (b) After H_2 desorption of hydrided Mg/Nb 10 nm at 373 K. [119]

In summary, the experiment evidence suggests that the hydrogen is absorbed and forms hydride phase at the Nb layer first, and vice versa. DFT calculations were performed for understanding those observed phenomena.

7.3 Computational procedure

The hydrogen diffusion in Mg and Nb systems were determined by using DFT calculations. The PAW-LDA method was used in this work. For a H atom in bulk Mg and Nb systems, one H atom was placed at interstitial sites of hcp Mg supercell (48 Mg atoms) and bcc Nb supercell (54 Nb atoms). Monkhorst-Pack grids of 9×5×3 and 6×6×6 were applied for hcp Mg and bcc supercells, accordingly. The planewave cut-off of 520 eV and a self-consistency convergence criterion of 10^{-5} eV were used.

For the thin film calculations, the thickness of the simulated film is represented by the number of monolayer (ML). The surface coverage (Θ) represents a ratio of the number of adsorbed atoms to the number of atoms in a filled monolayer on the surface. In this study, Θ is 0.5. In free standing films, the slab is separated by a 20 Å vacuum space in the direction normal to the surface. This vacuum prevents interaction between the images of periodic slabs. The (110) stacking and (0001) stacking are used in the 13ML-bcc Nb and the 13ML- hcp Mg slabs, respectively. The k-mesh of 19×11×1 and 11×19×1 were used for 13ML-hcp Mg and 13ML-bcc Nb, respectively. In Mg/Nb multilayers, the structure of 5 ML-pseudo-hcp Mg(0001)/5ML-bcc Nb(110) was used. The k-mesh of 9×7×3 was used for this structure. Energy barriers of hydrogen diffusion among interstices were obtained by using the CI-NEB method. A self consistency convergence criterion of 10^{-4} eV for the total energy per simulation cell was applied.

7.4 Hydrogen diffusion in bulk Mg and bulk Nb

First of all, the stabilities of interstitial hydrogen at low concentrations in bulk hcp Mg and bulk bcc Nb were studied. In this study, two types of interstitial sites are considered. Fig. 7.4 presents interstitial hydrogen at the tetrahedral interstitial site (T-site) and the octahedral interstitial site (O-site) in hcp Mg and bcc Nb lattices.

The optimization of a supercell, consisting of one H atom at an interstitial site (T-site or O-site), was performed. In Table 7.1, the energy difference for H atom in the T-site and the O-site of Mg- and Nb supercells. Hydrogen prefers the T-site than the O-site in both hcp Mg and bcc Nb as ΔE_{TO} are negative. Calculated ΔE_{TO} are similar to the values from the references.

Next, H diffusion mechanism between the T-site and the O-site in those bulk structures were investigated by using the CI-NEB approach. The energy barriers of

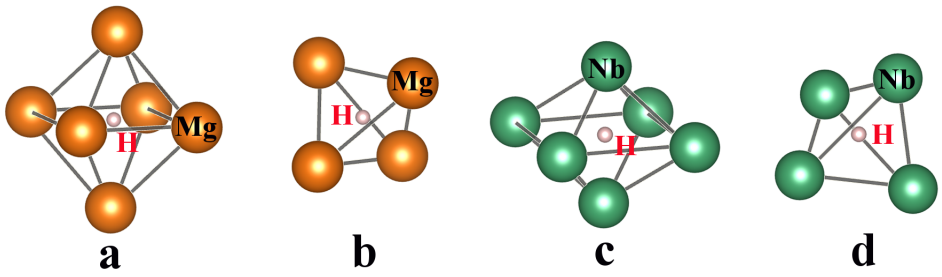

Figure 7.4: Interstitial sites (a) a O-site in hcp Mg, (b) a T-site in hcp Mg, (c) a O-site in bcc Nb and (d) a T-site in bcc Nb. H, Mg and Mg atoms are represented by pink, orange and green balls, respectively.

Table 7.1: The energy difference for isolated H in the T-site and the O-site of Mg- and Nb supercells, $\Delta E_{TO} = E_T - E_O$ calculated by PAW-LDA method

Metal	C = H/M[a]	ΔE_{TO} (eV/H atom)	Ref.
hcp Mg	0.0208	-0.081	-0.049 (c=0.0208[b])
bcc Nb	0.0185	-0.284	-0.328 (c=0.0625[c])

[a]C is an atomic fraction of hydrogen and metal in a supercell, [b][223]PAW-GGA method, [c][232]PAW-GGA method

hydrogen hoping along selected paths in Mg- and Nb supercells were examined. The results are given in Table 7.2. In Mg, the activation energy (ΔE_a) of H diffusion from T-site to O-site is about 0.23 eV. H is required less energy to diffuse between two T-sites compared to the hoping between two O-sites. In bcc Nb, H atom is required ΔE ~0.29 eV to move between two adjacent T-sites. Along the O-to-O path, H atom is repelled by the neighboring host atoms, then the energy barrier is higher than diffusions in other paths. When H moves from one T-site to the nearest O-site, there is no obstacle host atom along the path. Therefore, 0.28 eV of E_a is the energy difference of E_T and E_O. This value agrees well with ΔE_{TO} value reported in

Table 7.1. In summary, ΔE_a values of H diffusion in Mg are lower than those of H diffusion in Nb.

Table 7.2: The activation energy (ΔE_a) of H diffusion in Mg and Nb supercells

Path	ΔE_a (eV/)	
	hcp Mg	bcc Nb
T-site to O-site	0.23	0.28
T-site to T-site	0.05	0.29
O-site to O-site	0.23	1.00

7.5 Hydrogen diffusion in free standing films

In this part, the H diffusion in Mg(0001) films were investigated by moving H atom vertically above the Mg surface downward to the matrix. Fig 7.5(a) and 7.5(b) display the two dimensional views of fcc-site and hcp-site, respectively. The dark orange balls represent Mg atoms in surface layer (the first Mg layer) and the light orange balls are Mg atoms in sublayer (the second Mg layer). An energy profile of each diffusion path represents in relative energies compared with the lowest energy of that path.

In the first case, energy profiles of H diffusion through the fcc-channel is revealed in Fig 7.6. The calculated ΔE_a at selected positions are given in Table 7.4. The first peak of energy profile indicates ΔE_a ($\sim$0.50 eV) for H diffusion through the surface layer. This value agrees well with other studies (ΔE $\sim$0.5 eV) [71, 70]. ΔE_a decreases from $\sim$0.3 eV to $\sim$0.2 eV, when the H atom further diffuses through the second Mg layer to below the sixth Mg layer. These values are converged to ΔE_a

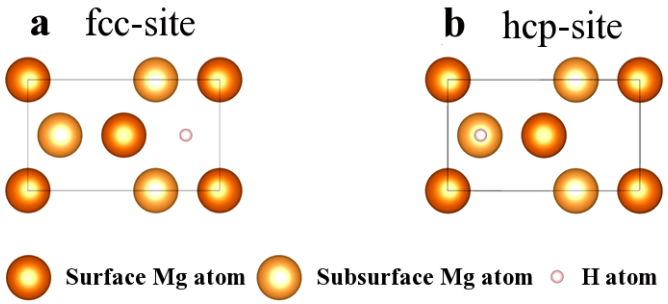

Figure 7.5: The atomic positions are projected on the out-of-plane direction of 13ML hcp Mg(0001) films. H atom is located (a) at the fcc-site and (b) at the hcp-site.

values observed in bulk Mg. In addition, the vibrational frequencies (ω) of H were calculated and reported in Table 7.4. The imaginary frequency (Im) indicates that the H atom locates at the transition state (TS) or the saddle point of the diffusion path. The results from this work agree well with the results calculated by Vegge *et al.* [71].

Next, the energy profile of hydrogen diffusion through the hcp-channel is shown in Fig 7.5. The energy barrier of the first peak cannot be observed clearly. After passing through the surface Mg layer (coordinate 5 in Fig. 7.5), the energy increases rapidly when the H atom moves further to the next Mg layer. The reason for this is that the H atom is repelled by Mg atoms in the sub-surface layer. In this work, the additional path was determined. After passing the surface layer, the path that H diffuses to the closest T-site (FS1) near sub-surface layer was investigated. TS1 represents H at the O-site-like environment located between two Mg layers. The diffusion between T-sites located above and below sub-surface layer requires the 0.20 eV of ΔE_2. TS3 reveals another O-site between the sub-surface Mg layer and the next Mg layer. As a result, the diffusion in the T-to-T path has lower ΔE_a than

Table 7.3: H diffusion trough the fcc-channel in 13ML hcp Mg(0001) freestanding films. The activation energy in the inward direction from surface to the matrix (ΔE_i) and in the opposite direction ($\Delta E_i'$) are given in eV. The imaginary frequency is denoted by Im. The calculated vibrational frequencies for the H atom (ω_i) in cm^{-1} and the corresponding zero point energy (ZPE=$\frac{1}{2}\sum_i \omega_i$) are reported.

Position	ΔE_a (eV)		ω_x (cm^{-1})	ω_y (cm^{-1})	ω_z (cm^{-1})	ZPE (eV)
IS			843	736	731	0.143
Ref.[a]			(745)	(752)	(706)	(0.137)
TS1	ΔE_1	0.50	854	647	Im	0.093
Ref.[a]		(0.53)	(745)	(733)	(Im)	(0.092)
	$\Delta E_1'$	0.18				
Ref.[a]		(0.17)				
FS1			560	471	435	0.091
Ref.[a]			(471)	(435)	(404))	(0.081)
TS2	ΔE_2	0.27	1201	991	Im	0.136
Ref.[a]		(0.18)	(1085)	(1050)	(Im)	(0.132)
	$\Delta E_2'$	0.27				
Ref.[a]		(0.19)				
FS2			487	410	390	0.056
Ref.[a]			(417)	(344)	(328)	(0.068)
TS3	ΔE_3	0.26	1085	1050	Im	0.136
Ref.[a]						
	$\Delta E_3'$	0.25				
Ref.[a]						
TS4	ΔE_4	0.25	1199	1016	Im	0.137
	$\Delta E_4'$	0.24				
TS5	ΔE_5	0.22				
	$\Delta E_5'$	0.22				
TS6	ΔE_6	0.22				

[a] [71] DFT calculations by using RPBE functional

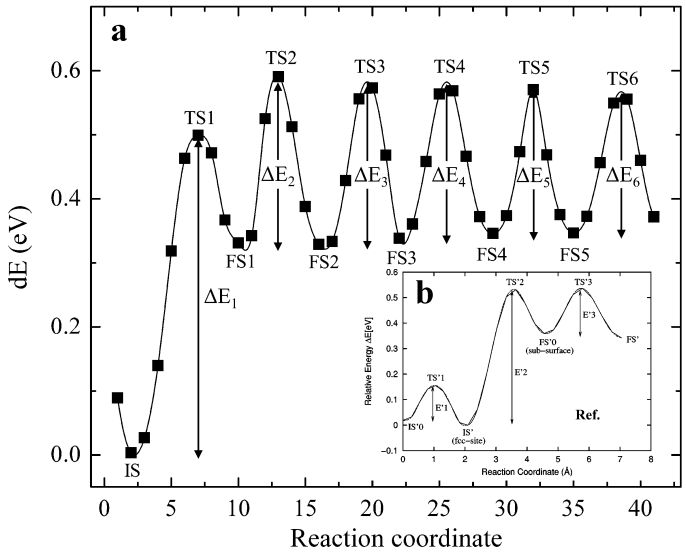

Figure 7.6: H diffusion trough fcc-channel in 13ML hcp Mg(0001) freestanding films (a) from this work and (b) from [71]

hoping from the T-to-O path.

Additionally, H atom located at the fcc-site has lower in energy than the H atom located at the hcp-site. The energy difference between fcc and hcp sites is ∼38 meV, which is comparable with the 20-25 meV obtained from literatures [71, 70].

Next, H diffusion in Nb(110) films was explored by using the same method. In this case, three possible initial sites on a surface were selected, which are the a-site, the b-site and the c-site, as shown in Fig. 7.8(a) to 7.8(c). The dark green balls represent Nb atoms in a surface layer (the first Nb layer) and the light green balls are Nb atoms in a sublayer (the second Nb layer). For Nb slabs, the H atom was initially located above the Nb surface. The H atom was moved downward into the Nb matrix. Calculated ΔE_a and ZPE values of all three cases are given in Table 7.5.

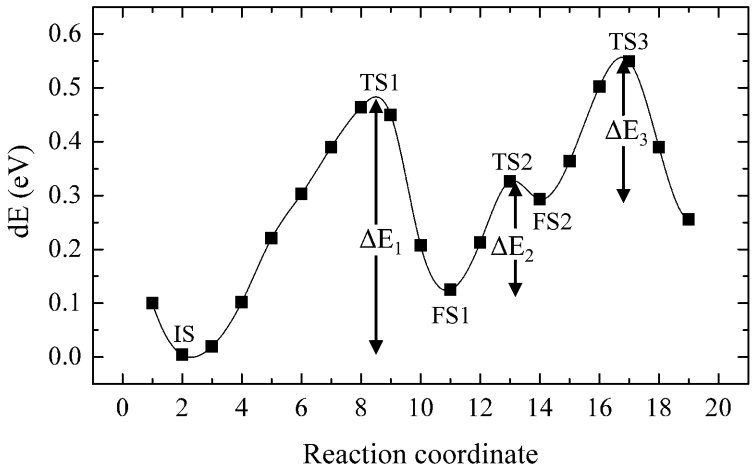

Figure 7.7: H diffusion trough hcp-channel and hop between two T-sites in zigzag direction in 13ML hcp Mg(0001) freestanding films

Fig. 7.9 to 7.11 demonstrate the energy profiles of H diffusion through the a-channel, the b-channel and the c-channel, respectively.

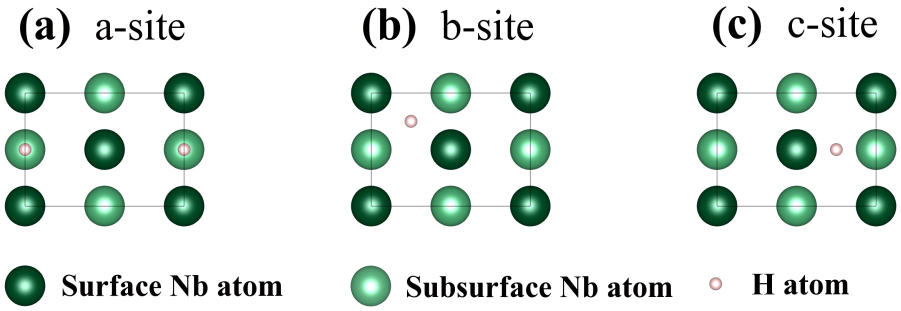

Figure 7.8: The atomic positions are projected on the out-of-plane direction of 13ML hcp Mg(0001) films. The H atom is located (a) at the fcc-site and (b) at the hcp-site.

In Fig. 7.9, ΔE_a of moving the H atom through the surface layer is ∼1.2 eV.

Table 7.4: H diffusion trough the hcp-channel in 13ML hcp Mg(0001) freestanding films. The activation energy in the inward direction from the surface to the matrix (ΔE_i) and in the opposite direction ($\Delta E_i'$) are given in eV. The imaginary frequency is denoted by Im. The calculated vibrational frequencies for the H atom (ω_i) in cm^{-1} and the corresponding zero point energy (ZPE=$\frac{1}{2}\sum_i \omega_i$) are reported.

Position	ΔE_a (eV)		ω_x (cm^{-1})	ω_y (cm^{-1})	ω_z (cm^{-1})	ZPE (eV)
IS			809	701	675	0.135
TS1	ΔE_1	0.48	936	204	Im	0.071
	$\Delta E_1'$	0.36				
FS1			916	872	813	0.161
TS2	ΔE_2	0.20	1200	1059	Im	0.140
	$\Delta E_2'$	0.03				
FS2			928	846	742	0.156
TS3	ΔE_3	0.26	1157	Im	Im	0.072
	$\Delta E_3'$	0.30				

When the H atom moves closer to the second Nb layer, the energy increases rapidly owing to a repulsive interaction between H and Nb atoms. The minima can be observed when the H atom is located at T-site-like environment. The result reveals similar feature presented in the hcp-case of Mg films. In the b-case, the ΔE values of H diffusion along this path are in range of 1.7 eV to 1.9 eV. The b-path reveals the higher ΔE_1 than other two cases. On the other hand, the lowest in ΔE_1 of the c-case suggests that the H diffusion through this path is the most favorable. In the c-case, the energy is converged when the H atom diffuses further to the middle of Nb films. The O-site-like environment is located along this path and results the small energy barriers (i.e. TS2, TS4 and TS6) shown in Fig. 7.11.

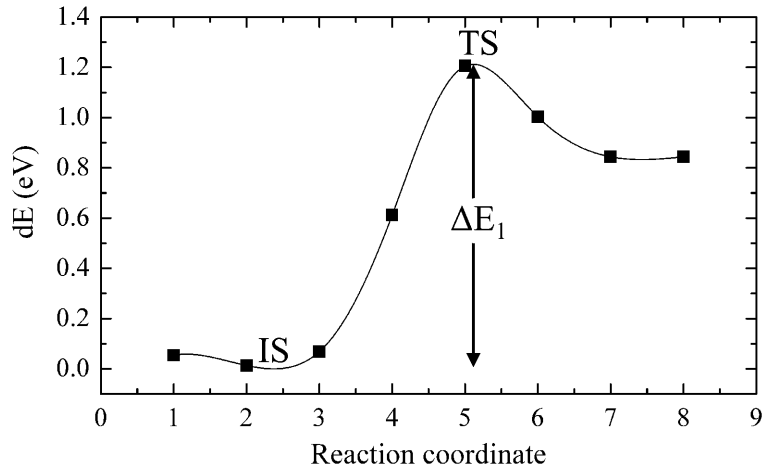

Figure 7.9: H diffusion trough the a-channel in 13ML bcc Nb(110) freestanding films

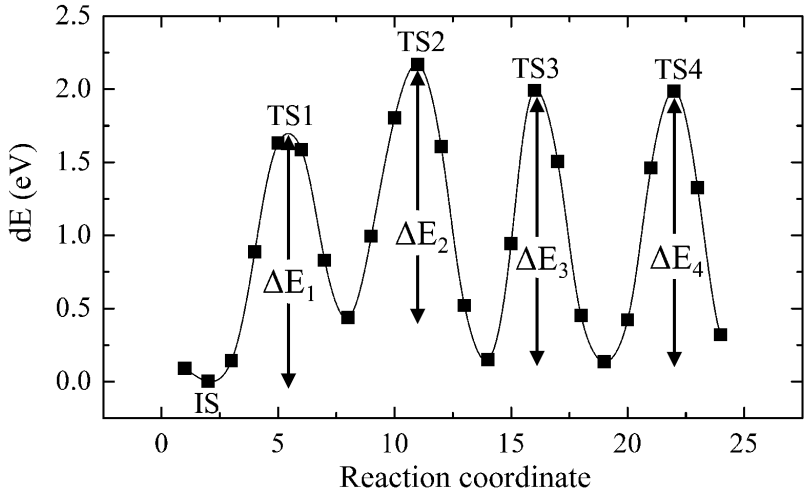

Figure 7.10: H diffusion trough the b-channel in 13ML bcc Nb(110) freestanding films

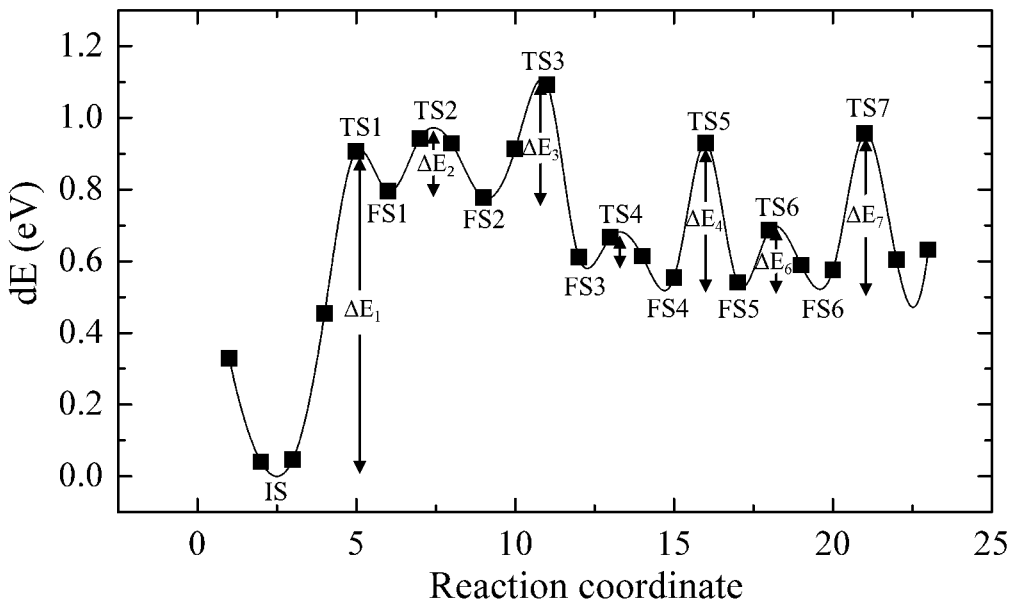

Figure 7.11: H diffusion trough the c-channel in 13ML bcc Nb(110) freestanding films

7.6 Hydrogen diffusion in Mg/Nb multilayers

In this section, H diffusion in Mg/Nb multilayers was determined. The three dimensional structure of pseudo-hcp Mg/bcc Nb multilayers displayed in Fig. 7.12 was used in this study. The Mg- and Nb-layers are labelled as the order shown in that figure. H diffusion was investigated in both in-plane and out-of-plane directions. Firstly, H diffusion was examine along the direction normal to the interface represented in Fig. 7.12. H atoms penetrate from the Nb region to the interface and Mg regions. The energy profile of this route is presented in Fig. 7.13. The corresponding ΔE_i values are given in Table 7.6. TS1 to FS5 positions represent the energies of H diffusion in the Nb region. H diffusion across the interface region is presented by

Table 7.5: H diffusion trough a-, b- and c-channels in 13ML bcc Nb(110) freestanding films. The activation energy in the inward direction from surface to the matrix (ΔE_i and in the opposite direction ($\Delta E_i'$) are given in eV. The zero point energy (ZPE=$\frac{1}{2}\sum_i \omega_i$) are reported.

Position	ΔE_a (eV)		ZPE
	ΔE	$\Delta E'$	(eV)
A-channel			
IS			0.144
TS1	1.21	0.38	0.198
FS1			0.208
B-channel			
IS			0.157
TS1	1.70	1.26	0.180
FS1			0.240
TS2	1.74	2.03	0.202
FS2			0.244
TS3	1.85	1.86	0.198
FS3			0.244
TS4	1.85		0.198
C-channel			
IS			0.179
TS1	0.91	0.12	0.232
FS1			0.240
TS2	0.18	0.20	0.158
FS2			0.245
TS3	0.33	0.53	0.243
FS3			0.237
TS4	0.10	0.16	
FS4			0.253
TS5	0.41	0.40	0.242
FS5			
TS6	0.17	0.18	0.131
FS6			0.254
TS7	0.44		0.241

FS5 to TS6. The rest of the coordinates represent H diffusion from the Mg(5) layer trough the Mg(3) layer. The energy profile indicates that the H atom located in the Nb region has lower energy than another region. H hopping to the Nb region

requires lower energy than hopping to the Mg region. This result supports the experiment evidence. The experiment shows that NbH is formed before MgH_2 phase in the hydrogenation process. On the other hand, H is released from Mg first in the de-hydrogenation process.

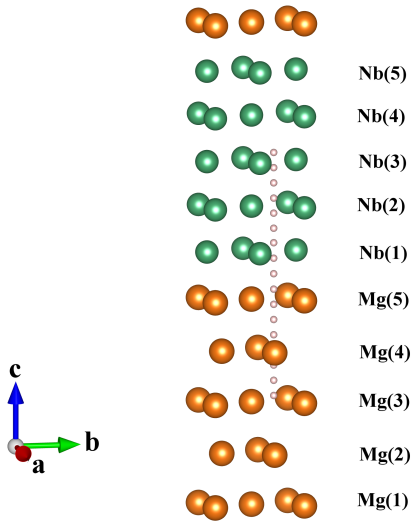

Figure 7.12: The schematic of H diffusion path along the out-of-plane direction in pseudo-hcp Mg/bcc Nb multilayers.

In the second route, the H atom is placed at the middle of two successive layers. According the labeled sequence in Fig. 7.12, five different paths were chosen, which are Nb(3)-Nb(2), Nb(2)-Nb(1), interface, Mg(5)-Mg(4) and Mg(4)-Mg(3). In this case, all metal atoms were fixed for simplifying the calculations. As the result, all five paths expose the same shape of energy profile, but the magnitudes of ΔE_a values are different. For instance, the energy profile of H diffusion along the interface is shown in Fig. 7.14. There are two saddle points (ΔE_1 and ΔE_2) presented along this path. For the interface case, when H migrates close to the Nb(1) layer, the

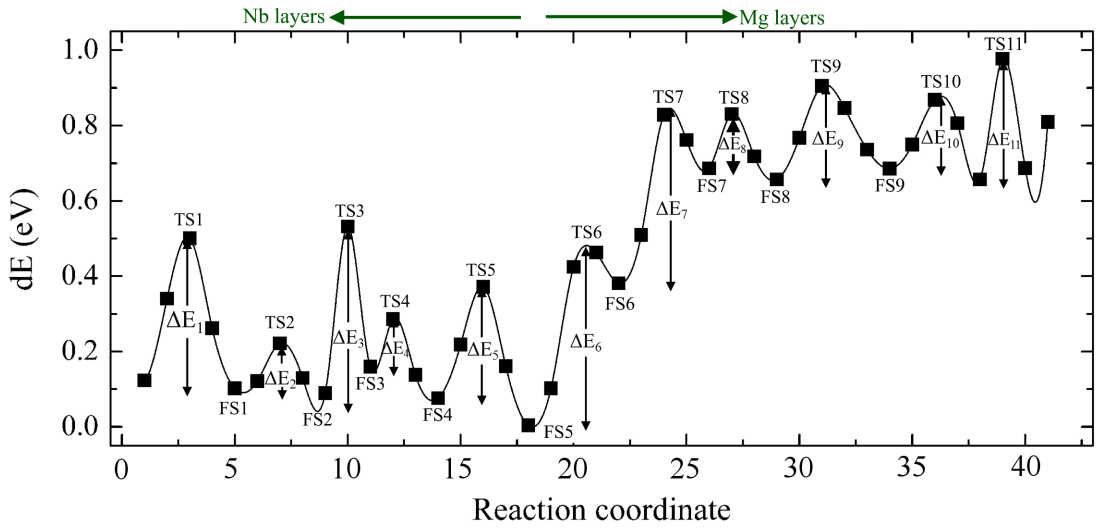

Figure 7.13: H diffusion through the out-of-plane direction of pseudo-hcp Mg/bcc Nb multilayers. All atoms are allowed to move.

energy is lower than moving to the Mg side. Calculated ΔE_a values of five cases are reported in Table 7.7. In Fig. 7.15, ΔE_1 and ΔE_2 are compared as a function of the position. In the Mg region, ΔE_1 increases when the distance from the interface is longer, but the opposite trend can be observed from H diffusion in the Nb region. ΔE_2 shows less deviation than ΔE_1. In contrary, ΔE_2 values of H diffusion in the Mg region is lower than those of diffusion in the Nb region. However, ΔE_2 in both regions are comparable.

7.7 Conclusions

In summary, H diffusion in Mg/Nb multilayers and their bulk phase were studied by using DFT calculations. More understanding of H sorption behavior in Mg/Nb multilayers could be attained. In free-standing cases, penetration of H trough the surface layer in Nb films is more difficult than that in Mg films. In contrary, the H atom prefers migrating through the Nb region in Mg/Nb multilayers. This result

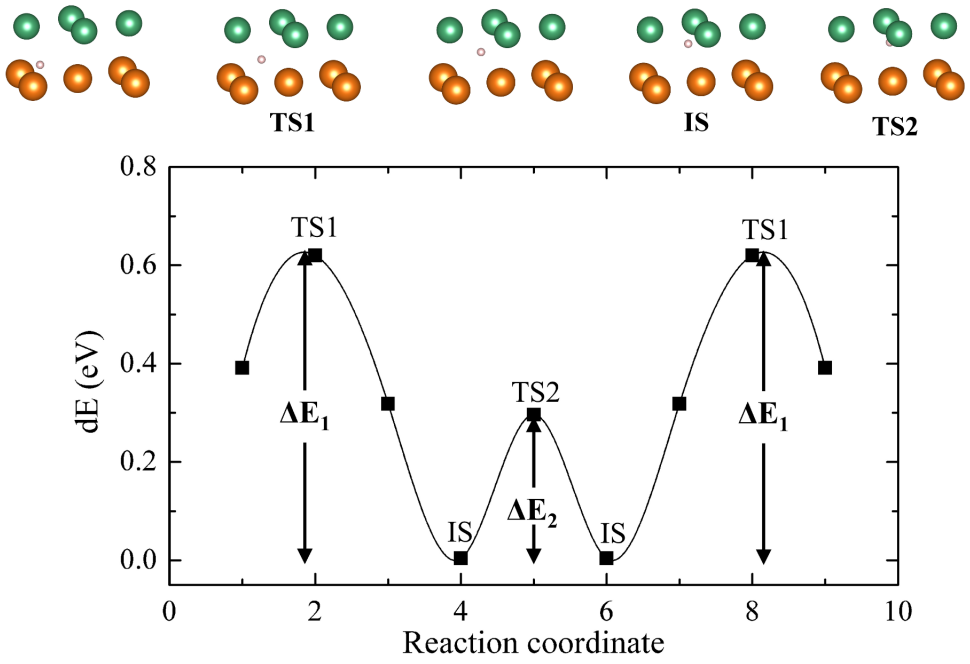

Figure 7.14: The energy profile of H diffusion along the in-plane direction at the interface of pseudo-hcp Mg/bcc Nb multilayers. The corresponding figures are provided on top of the figure. Only the H atom is allowed to move.

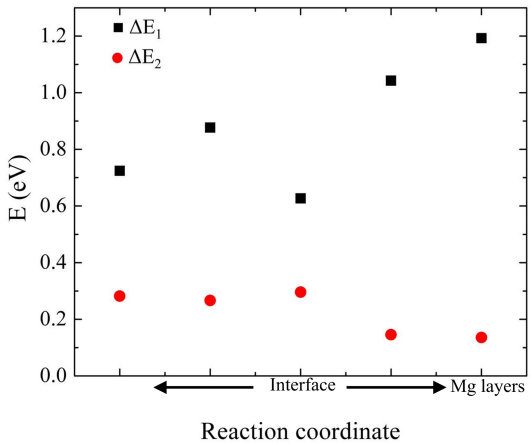

Figure 7.15: Comparison ΔE_1 and ΔE_2 of H diffusion along the in-plane direction as a function of the distance from interface.

Table 7.6: H diffusion along the out-of-plane direction in 5ML-pseudohcp Mg and 5ML-bcc Nb multilayers. The activation energy along the direction of the Nb layer to the Mg layer (ΔE_i) and the activation energy along the opposite direction ($\Delta E_i'$) are given in eV.

Position	ΔE_a (eV)	
	ΔE	$\Delta E'$
TS1		0.41
TS2	0.13	0.18
TS3	0.49	0.39
TS4	0.14	0.22
TS5	0.30	0.37
TS6	0.48	0.10
TS7	0.47	0.17
TS8	0.15	0.18
TS9	0.25	0.22
TS10	0.19	0.23
TS11	0.33	

coincides with the experimental observation. The NbH phase is detected first in the hydrogenation process, while MgH_2 releases H first in the de-hydrogenation process.

Table 7.7: H diffusion along the in-plane direction in 5ML-pseudohcp Mg and 5ML-bcc Nb multilayers.

Position	ΔE_1	ΔE_2
between Nb(3) and Nb(2)	0.72	0.28
between Nb(2) and Nb(1)	0.88	0.27
Interface	0.63	0.30
between Mg(5) and Mg(4)	1.04	0.15
between Mg(4) and Mg(3)	1.19	0.14

8. SUMMARY AND CONCLUSIONS

In summary, this work has been done for investigating the hydrogen sorption properties in Mg/Nb multilayers. The ultimate goal of the study is to improve the kinetic and thermodynamic properties of Mg hydrides for hydrogen storage applications. The theoretical methods have been employed for understanding the experimental observation. Several properties such as the structural, energetic, electronic charge, thermodynamic and mechanical properties have been determined in Mg/Nb multilayers, Mg freestanding films and bulk phases and their hydrided phases.

First, the properties of Mg/Nb multilayers were investigated. The metastable Mg bcc phase was first observed in Mg/Nb multilayers at ambient conditions. The theoretical approaches were used for understanding this phenomenon. The bi-phase diagram of Mg/Nb multilayers was predicted by using the classical thermodynamic approach. The result shows that the metastable bcc Mg phase can be stabilized in specific range of bilayer thickness and volume fraction of constituent elements. The predicted bi-phase diagram also proposes that the metastable hcp Nb can be stabilized under the thin films conditions also. This result was successfully verified by the experiments. In addition, DFT calculations were performed and show that the metastable bcc Mg is stabilized when it is constrained with the Nb lattice parameter. This constrained bcc Mg phase is mechanical stable. The interface calculations also support the energetic preference of forming bcc Mg and hcp Nb phases under the thin film environment. This study provides a basis for the design of Mg- based nano materials with properties not observed in bulk.

Next, the sorption properties of Mg/Nb multilayers were examined. The computational method is useful for assisting the experimental study. The improvement

of hydrogen sorption properties in Mg/Nb multilayers was observed experimentally. Stress-induced metastable orthorhombic-Mg_2 (O-MgH_2) phases are formed in the thin films. The oxidized Si(110) substrate plays an important role in the single layer Mg case, while Nb exhibits as the substrate in the Mg/Nb multilayers case. Destabilization of these O-MgH_2 phases can be explained from the formation enthalpy calculated by using DFT calculations. Experimental evidence suggested that stresses arise from either substrate constraint or volume expansion incompatibility. The calculations also confirm these reasons. These studies provide important design criteria for selection of appropriate second phase to destabilize Mg hydride.

Furthermore, hydrogen diffusion in Mg/Nb multilayers were investigated by CI-NEB method. The results agree well with the experimental observation. Owing to the energetic reason, NbH is formed first during the hydriding process, while Mg is recovered first during the dehydriding process.

Finally, the improvement in thermodynamic properties of Mg hydrides was achieved in this work. The concepts of stress-assisted H_2-sorption and stabilizing metastable phases under thin films conditions are valuable and they can be applied in further studies.

REFERENCES

[1] A. Züttel. *Hydrogen as a future energy carrier*. Wiley-VCH Verlag GmbH Co. KGaAc, Germany, 2008.

[2] A. Züttel, A. Remhof, A. Borgschulte, and O. Friedrichs. Hydrogen: the future energy carrier. *Philosophical Transactions of the Royal Society A: Mathematical, Physical and Engineering Sciences*, 368(1923):3329–3342, 2010.

[3] J. R. Fanchi. *Energy in the 21st century /John R. Fanchi.* World Scientific, Singapore, 2005.

[4] C.L. Muhich, B.W. Evanko, K.C. Weston, P. Lichty, X. Liang, J. Martinek, C.B. Musgrave, and A.W. Weimer. Efficient generation of H_2 by splitting water with an isothermal redox cycle. *Science*, 341(6145):540–542, 2013.

[5] L. Schlapbach. Technology: hydrogen-fuelled vehicles. *Nature*, 460:809–811, 2009.

[6] J. Zheng, X. Liu, P. Xu, P. Liu, Y. Zhao, and J. Yang. Development of high pressure gaseous hydrogen storage technologies. *International Journal of Hydrogen Energy*, 37(1):1048–1057, 2012.

[7] A. Züttel. Materials for hydrogen storage. *Materials Today*, 6(9):24–33, 2003.

[8] L. Schlapbach and A. Züttel. Hydrogen-storage materials for mobile applications. *Nature*, 414:353, 2001.

[9] Z.X. Guo, C. Shang, and K.F. Aguey-Zinsou. Materials challenges for hydrogen storage. *Journal of the European Ceramic Society*, 28(7):1467–1473, 2008.

[10] Targets for onboard hydrogen storage systems for light-duty vehicles, US Department of Energy Office of Energy Efficiency and Renewable Energy and The FreedomCAR and Fuel Partnership, 2009.

[11] F. Barbir. *PEM Fuel Cells-Theory and Practice*. Academic Press, Waltham, MA, 2nd edition, 2013.

[12] A. Léon. *Hydrogen Technology: Mobile and Portable Applications (Green Energy and Technology)*. Springer, Germany, 2008.

[13] R. Ströbel, J. Garche, P.T. Moseley, L. Jörissen, and G. Wolf. Hydrogen storage by carbon materials. *Journal of Power Sources*, 159(2):781–801, 2006.

[14] K.S.W. Sing, D.H. Everett, R.A.W. Haul, L. Moscou, R.A. Pierotti, J. Rouquérol, and T. Siemieniewska. Reporting physisorption data for gas/solid systems with special reference to the determination of surface area and porosity. *Pure and Applied Chemistry*, 57(4):603619, 1985.

[15] M.P. Suh, H.J. Park, T.K. Prasad, and D. Lim. Hydrogen storage in metal-organic frameworks. *Chemical Reviews*, 112:782–835, 2011.

[16] S.K. Bhatia and A.L. Myers. Optimum conditions for adsorptive storage. *Langmuir*, 22(22):1688–1700, 2006.

[17] M. Hirscher. *Handbook of hydrogen storage: New Materials for Future Energy Storage*. Wiley-VCH Verlag GmbH Co. KGaA, Germany, 2010.

[18] S.J. Yang, H. Jung, T. Kim, and C.R. Park. Recent advances in hydrogen storage technologies based on nanoporous carbon materials. *Progress in Natural Science: Materials International*, 22(6):631 – 638, 2012.

[19] S.B. Kayiran, F.D. Lamari, and D. Levesque. Adsorption properties and structural characterization of activated carbons and nanocarbons. *The Journal of Physical Chemistry B*, 108(39):15211–15215, 2004.

[20] Y. Xia, Z. Yang, and Y. Zhu. Porous carbon-based materials for hydrogen storage: advancement and challenges. *Journal of Materials Chemistry A*, 1:9365–9381, 2013.

[21] K.M. Thomas. Hydrogen adsorption and storage on porous materials. *Catalysis*

Today, 120(34):389 – 398, 2007.

[22] A.C. Dillon, K.M. Jones, T.A. Bekkedahl, C.H. Kiang, D.S. Bethune, and M.J. Heben. Storage of hydrogen in single-walled carbon nanotubes. *Nature*, 386(6623):377–379, 1997.

[23] F.L. Darkrim, P. Malbrunot, and G.P. Tartaglia. Review of hydrogen storage by adsorption in carbon nanotubes. *International Journal of Hydrogen Energy*, 27(2):193 – 202, 2002.

[24] C. Liu and H.-M. Cheng. Carbon nanotubes for clean energy applications. *Journal of Physics D: Applied Physics*, 38(14):R231, 2005.

[25] H. Kabbour, T.F. Baumann, J.H. Satcher, A. Saulnier, and C.C. Ahn. Toward new candidates for hydrogen storage: High-surface-area carbon aerogels. *Chemistry of Materials*, 18(26):6085–6087, 2006.

[26] T.F. Baumann, M.A. Worsley, T.Y-J. Han, and J.H. Satcher Jr. High surface area carbon aerogel monoliths with hierarchical porosity. *Journal of Non-Crystalline Solids*, 354(29):3513 – 3515, 2008.

[27] T.A. Strobel, K.C. Hester, C.A. Koh, A.K. Sum, and E.D. Sloan Jr. Properties of the clathrates of hydrogen and developments in their applicability for hydrogen storage. *Chemical Physics Letters*, 478(46):97 – 109, 2009.

[28] D. Pukazhselvan, V. Kumar, and S.K. Singh. High capacity hydrogen storage: Basic aspects, new developments and milestones. *Nano Energy*, 1(4):566 – 589, 2012.

[29] A. Chambers, C. Park, R.T.K. Baker, and N.M. Rodriguez. Hydrogen storage in graphite nanofibers. *The Journal of Physical Chemistry B*, 102(22):4253–4256, 1998.

[30] M. Dincă and J.R. Long. Hydrogen storage in microporous metalorganic frameworks with exposed metal sites. *Angewandte Chemie International Edition*,

47(36):6766–6779, 2008.

[31] A. Bocarsly and D.M.P. Mingos. *Fuel Cells and Hydrogen Storage*. Springer Berlin Heidelberg, New York, 2011.

[32] L.J. Murray, M. Dinca, and J.R. Long. Hydrogen storage in metal-organic frameworks. *Chemical Society Reviews*, 38:1294–1314, 2009.

[33] N.L. Rosi, J. Eckert, M. Eddaoudi, D.T. Vodak, J. Kim, M O'Keeffe, and O.M. Yaghi. Hydrogen storage in microporous metal-organic frameworks. *Science*, 300(5622):1127–1129, 2003.

[34] S. Ma, J. Eckert, P.M. Forster, J.W. Yoon, Y.K. Hwang, J.-S. Chang, C.D. Collier, J.B. Parise, and H.-C. Zhou. Further investigation of the effect of framework catenation on hydrogen uptake in metal-organic frameworks. *Journal of the American Chemical Society*, 130:15896–15902, 2008.

[35] D.P. Broom. *Hydrogen Storage Materials: The Characterisation of Their Storage Properties*. Springer-Verlag, London, 2011.

[36] M. Dornheim. Thermodynamics - interaction studies - solids, liquids and gases. *InTech*, 2011.

[37] T. Graham. On the absorption and dialytic separation of gases by colloid septa. *Philosophical Transactions of the Royal Society of London*, 156:399–439, 1866.

[38] I.P. Jain, C. Lal, and A. Jain. Hydrogen storage in Mg: A most promising material. *International journal of hydrogen energy*, 35:5133–5144, 2010.

[39] J. Graetz and J.J. Reilly. Thermodynamics of the and polymorphs of AlH_3. *Journal of Alloys and Compounds*, 424(12):262 – 265, 2006.

[40] B. Bogdanović and M. Schwickardi. Ti-doped alkali metal aluminium hydrides as potential novel reversible hydrogen storage materials. *Journal of Alloys and Compounds*, 253254(0):1 – 9, 1997.

[41] X. Fan, X. Xiao, L. Chen, S. Li, H. Ge, and Q. Wang. Enhanced hydrid-

ingdehydriding performance of $CeAl_2$-doped $NaAlH_4$ and the evolvement of Ce-containing species in the cycling. *The Journal of Physical Chemistry C*, 115(5):2537–2543, 2011.

[42] X. Fan, X. Xiao, L. Chen, L. Zhang, J. Shao, S. Li, H. Ge, and Q. Wang. Signicantly improved hydrogen storage properties of $NaAlH_4$ catalyzed by Ce-based nanoparticles. *Journal of Materials Chemistry A*, 1:9752 – 9759, 2013.

[43] B. Bogdanović, M. Felderhoff, A. Pommerin, F. Schüth, and N. Spielkamp. Advanced Hydrogen-Storage Materials Based on Sc-, Ce-, and Pr-Doped $NaAlH_4$. *Advanced Materials*, 18(9):1198–1201, 2006.

[44] L. Li, C. Xu, C. Chen, Y. Wang, L. Jiao, and H. Yuan. Sodium alanate system for efficient hydrogen storage. *International Journal of Hydrogen Energy*, 38(21):8798 – 8812, 2013.

[45] Y.A. Dyadin, É.G. Larionov, E.Y. Aladko, A.Y. Manakov, F.V. Zhurko, T.V. Mikina, V.Y. Komarov, and E.V. Grachev. Clathrate formation in water-noble gas (hydrogen) systems at high pressures. *Journal of Structural Chemistry*, 40(5):790–795, 1999.

[46] L.J. Florusse, C.J. Peters, J. Schoonman, K.C. Hester, C.A. Koh, S.F. Dec, K.N. Marsh, and E.D. Sloan. Stable low-pressure hydrogen clusters stored in a binary clathrate hydrate. *Science*, 306(5695):469–471, 2004.

[47] B. Vigeholm, J. Kjøller, B. Larsen, and A.S. Pedersen. Formation and decomposition of magnesium hydride. *Journal of the Less Common Metals*, 89(1):135 – 144, 1983.

[48] S. Boily A. Van Neste J. Huot, G. Liang and R. Schulz. Structural study and hydrogen sorption kinetics of ball-milled magnesium hydride. *Journal of Alloys and Compounds*, 293-295(0):495 – 500, 1999.

[49] H. Shao, G. Xin, J. Zheng, X. Li, and E. Akiba. Nanotechnology in Mg-based

materials for hydrogen storage. *Nano Energy*, 1(4):590 – 601, 2012.

[50] A. Miotello C. Sada P. Mazzoldi N. Bazzanella, R. Checchetto and P. Mengucci. Hydrogen kinetics in magnesium hydride: On different catalytic effects of niobium. *Applied Physics Letters*, 89(1):014101, 2006.

[51] S. Boily A. Van Neste G. Liang, J. Huot and R. Schulz. Hydrogen storage properties of the mechanically milled MgH_2-nanocomposite. *Journal of Alloys and Compounds*, 291(1-2):295 – 299, 1999.

[52] S. Boily A. Van Neste G. Liang, J. Huot and R. Schulz. Catalytic effect of transition metals on hydrogen sorption in nanocrystalline ball milled MgH_2-Tm (Tm=Ti, V, Mn, Fe and Ni) systems. *Journal of Alloys and Compounds*, 292(1-2):247 – 252, 1999.

[53] T. Klassen G. Barkhordarian and R. Bormann. Fast hydrogen sorption kinetics of nanocrystalline Mg using Nb_2O_5 as catalyst. *Scripta Materialia*, 49(3):213 – 217, 2003.

[54] A.L.M. Costa A.R Yavari W.J Botta F J.F.R. de Castro, S.F. Santos and T.T. Ishikawa. Structural characterization and dehydrogenation behavior of Mg5-at.%Nb nano-composite processed by reactive milling. *Journal of Alloys and Compounds*, 376(1-2):251 – 256, 2004.

[55] N. Hanada, T. Ichikawa, and H. Fujii. Catalytic effect of nanoparticle 3d-transition metals on hydrogen storage properties in magnesium hydride MgH_2 prepared by mechanical milling. *The Journal of Physical Chemistry B*, 109(15):7188–7194, 2005.

[56] J.J. Reilly and R.H. Wiswall. Reaction of hydrogen with alloys of magnesium and nickel and the formation of Mg_2NiH_4. *Inorganic Chemistry*, 7(11):2254–2256, 1968.

[57] H. Ren, Y. Zhang, B. Li, D. Zhao, S. Guo, and X. Wang. Influence of the

substitution of La for Mg on the microstructure and hydrogen storage characteristics of $Mg_{20x}La_xNi_10$ (x=06) alloys. *International Journal of Hydrogen Energy*, 34(3):1429 – 1436, 2009.

[58] C. Broedersz B. Dam, R. Gremaud and R. Griessen. Combinatorial thin film methods for the search of new lightweight metal hydrides. *Scripta Materialia*, 56(10):853 – 858, 2007.

[59] A. Baldi and B. Dam. Thin film metal hydrides for hydrogen storage applications. *Journal of Materials Chemistry*, 21:4021–4026, 2011.

[60] S.T. Kelly R. Kelekar, H. Giffard and B.M. Clemens. Formation and dissociation of MgH_2 in epitaxial Mg thin films. *Journal of Applied Physics*, 101(11):114311, 2007.

[61] K. Higuchi, K. Yamamoto, H. Kajioka, M. Honda K. Toiyama, S. Orimo, and H. Fujii. Remarkable hydrogen storage properties in three-layered Pd/Mg/Pd thin films. *Journal of Alloys and Compounds*, 330-332(0):526 – 530, 2002.

[62] K.-J. Jeon, H.R. Moon, A.M. Ruminski, B. Jiang, C. Kisielowski, R. Bardhan, and J.J. Urban. Air-stable magnesium nanocomposites provide rapid and high-capacity hydrogen storage without using heavy-metal catalysts. *Nature Materials*, 10(4):286 – 290, 2011.

[63] C. Jacoboni and L. Reggiani. The Monte Carlo method for the solution of charge transport in semiconductors with applications to covalent materials. *Review of Modern Physics*, 55:645–705, Jul 1983.

[64] I. Steinbach. Phase-field models in materials science. *Modelling and Simulation in Materials Science and Engineering*, 17(7):073001, 2009.

[65] A.K. Singh, J. Lu, R.S. Aga, and B.I. Yakobson. Hydrogen Storage Capacity of Carbon-Foams: Grand Canonical Monte Carlo Simulations. *The Journal of Physical Chemistry C*, 115(5):2476–2482, 2011.

[66] T. Heine, L. Zhechkov, and G. Seifert. Hydrogen storage by physisorption on nanostructured graphite platelets. *Physical Chemistry Chemical Physics*, 6:980–984, 2004.

[67] T. Sagara, J. Klassen, and E. Ganz. Computational study of hydrogen binding by metal-organic framework-5. *The Journal of Chemical Physics*, 121(24):12543–12547, 2004.

[68] C. Wolverton, D.J. Siegel, A.R. Akbarzadeh, and V. Ozoliņš. Discovery of novel hydrogen storage materials: an atomic scale computational approach. *Journal of Physics: Condensed Matter*, 20(6):064228, 2008.

[69] J. Li, T. Furuta, H. Goto, T. Ohashi, Y. Fujiwara, and S. Yip. Theoretical evaluation of hydrogen storage capacity in pure carbon nanostructures. *The Journal of Chemical Physics*, 119(4):2376–2385, 2003.

[70] N. Jacobson, B. Tegner, E. Schroder, P. Hyldgaard, and B.I. Lundqvist. Hydrogen dynamics in magnesium and graphite. *Computational Materials Science*, 24(1):273–277, 2002.

[71] T. Vegge. Locating the rate-limiting step for the interaction of hydrogen with Mg(0001) using density-functional theory calculations and rate theory. *Physical Review B*, 70:035412, Jul 2004.

[72] R.M. Martin. *Electronic structure: basic theory and practical methods*. University Press, Cambridge, 2004.

[73] P. Hohenberg and W. Kohn. Inhomogeneous electron gas. *Physical Review*, 136:B864–B871, Nov 1964.

[74] J. P. Perdew and A. Zunger. Self-interaction correction to density-functional approximations for many-electron systems. *Physical Review B*, 23:5048–5079, May 1981.

[75] J. P. Perdew, K. Burke, and Y. Wang. Generalized gradient approximation for

the exchange-correlation hole of a many-electron system. *Physical Review B*, 54:16533–16539, 1996.

[76] C. Lee, W. Yang, and R. G. Parr. Development of the colle-salvetti correlation-energy formula into a functional of the electron density. *Physical Review B*, 37:785–789, Jan 1988.

[77] A.D. Becke. Density-functional thermochemistry. iii. the role of exact exchange. *The Journal of Chemical Physics*, 98(7):5648–5652, 1993.

[78] J. Hafner. Atomic-scale computational materials science. *Acta Materialia*, 48(1):71 – 92, 2000.

[79] P. Pulay. Ab initio calculation of force constants and equilibrium geometries in polyatomic molecules. *Molecular Physics*, 17(2):197–204, 1969.

[80] R.P. Feynman. Forces in molecules. *Phys. Rev.*, 56:340–343, Aug 1939.

[81] The Vienna Ab initio Simulation Package (VASP) (http://www.vasp.at/). [Online; created 16-April-2012].

[82] P.E. Blöchl. Projector augmented-wave method. *Physical Review B*, 50:17953–17979, 1994.

[83] H.J. Monkhorst and J.D. Pack. Special points for Brillouin-zone integrations. *Physical Review B*, 13:5188–5192, Jun 1976.

[84] D.J. Chadi and M.L. Cohen. Special points in the brillouin zone. *Physical Review B*, 8:5747–5753, Dec 1973.

[85] P.E. Blöchl, O. Jepsen, and O.K. Andersen. Improved tetrahedron method for brillouin-zone integrations. *Physical Review B*, 49:16223–16233, Jun 1994.

[86] D.S. Sholl and J.A. Steckel. *Density functional theory: A practical introduction*. John Wiley Sons., New Jersey, 2009.

[87] A. D. Becke and K. E. Edgecombe. A simple measure of electron localization in atomic and molecular systems. *The Journal of Chemical Physics*, 92(9):5397–

5403, 1990.

[88] P. Ravindran, P. Vajeeston, R. Vidya, H. Fjellvåg, and A. Kjekshus. Modeling of hydrogen storage materials by density-functional calculations. *Journal of Power Sources*, 159(1):88 – 99, 2006.

[89] A. Savin. The electron localization function (elf) and its relatives: interpretations and difficulties. *Journal of Molecular Structure: THEOCHEM*, 727(1-3):127 – 131, 2005.

[90] L. De Santis and R. Resta. Electron localization at metal surfaces. *Surface Science*, 450(1-2):126 – 132, 2000.

[91] S. Wei and M.Y. Chou. *Ab initio* calculation of force constants and full phonon dispersions. *Physical Review Letters*, 69:2799–2802, Nov 1992.

[92] A. van de Walle and G. Ceder. The effect of lattice vibrations on substitutional alloy thermodynamics. *Reviews of Modern Physics*, 74:11–45, Jan 2002.

[93] K. Parlinski, Z.Q. Li, and Y. Kawazoe. First-principles determination of the soft mode in cubic zro_2. *Physical Review Letters*, 78:4063–4066, 1997.

[94] K. Parlinski. Phonon software (http://wolf.ifj.edu.pl/phonon/), 2007. [Online; accessed 21-October-2012].

[95] S.A. Dregia, R. Banerjee, and H.L. Fraser. Polymorphic phase stability in thin multilayers. *Scripta Materialia*, 39(2):217–223, 1998.

[96] J.C. Li, W. Liu, and Q. Jiang. Bi-phase transition diagrams of metallic thin multilayers. *Acta Materialia*, 53(4):1067–1071, 2005.

[97] J.Q. Zheng, J.B. Ketterson, and G.P. Felcher. Synthesis of layered crystals of titanium silver. *Journal of Applied Physics*, 53(5):3624–3628, 1982.

[98] R. Ahuja and H.L. Fraser. Microstructural transitions in Titanium-Aluminum thin film multilayers. *Journal of Electronic Materials*, 23(10):1027–1034, 1994.

[99] R. Banerjee, R. Ahuja, and H.L. Fraser. Dimensionally Induced Structural

transformations in Titanium-Aluminum Multilayers. *Physical Review Letters*, 76:3778–3781, May 1996.

[100] J. Chakraborty, K. Kumar, R. Ranjan, S.G. Chowdhury, and S.R. Singh. Thickness-dependent fcc–hcp phase transformation in polycrystalline titanium thin films. *Acta Materialia*, 59(7):2615–2623, 2011.

[101] R. Hoogeveen, M. Moske, H. Geisler, and K. Samwer. Texture and phase transformation of sputter-deposited metastable Ta films and TaCu multilayers. *Thin Solid Films*, 275(1-2):203–206, 1996.

[102] F. Pan, M. Zhang, M. Ding, B.X. Liu, Y.M. Zhou, and D.S. Wang. Metastable rhombohedral Fe phase formed in Fe/Sb multilayers and its magnetic properties. *Physical Review B*, 59:11458–11464, May 1999.

[103] W.P. Lowe and T.H. Geballe. NbZr multilayers. I. Structure and superconductivity. *Physical Review B*, 29:4961–4968, May 1984.

[104] G.B. Thompson, R. Banerjee, S.A. Dregia, and H.L. Fraser. Phase stability of bcc Zr in Nb/Zr thin film multilayers. *Acta Materialia*, 51(18):5285–5294, 2003.

[105] O. Dubos, W. Petry, J. Neuhaus, and B. Hennion. Anharmonic dynamical behaviour in bcc zirconium. *European Physical Journal B*, 3(4):447–454, 1998.

[106] J.Y. Zhang, P. Zhang, X. Zhang, R.H. Wang, G. Liu, G.J. Zhang, and J. Sun. Mechanical properties of fcc/fcc Cu/Nb nanostructured multilayers. *Materials Science and Engineering A*, 545(0):118–122, 2012.

[107] P. Boher, F. Giron, Ph. Houdy, P. Beauvillain, C. Chappert, and P. Veillet. Structural and magnetic properties of diode radio-frequency sputtered Cr/Co multilayers. *Journal of Applied Physics*, 70(10):5507–5511, 1991.

[108] W. Vavra, D. Barlett, S. Elagoz, C. Uher, and R. Clarke. Structural transition in epitaxial Co-Cr superlattices. *Physical Review B*, 47:5500–5503, Mar 1993.

[109] Y.H. Liou, W.F. Pong, M.-H. Tsai, K.H. Chang, H.H. Hseih, Y.K. Chang, F.Z. Chien, P.K. Tseng, J.F. Lee, Y. Liou, and J.C.A. Huang. Structural characterization of the Co/Cr multilayers by x-ray-absorption spectroscopy. *Physical Review B*, 62:9616–9620, Oct 2000.

[110] B.L. Mordike and T. Ebert. Magnesium: Properties applications potential. *Materials Science and Engineering: A*, 302(1):37 – 45, 2001.

[111] R.H. Taylor, S. Curtarolo, and G.L.W. Hart. Ordered magnesium-lithium alloys: First-principles predictions. *Physical Review B*, 81:024112, Jan 2010.

[112] T. Al-Samman. Comparative study of the deformation behavior of hexagonal magnesiumlithium alloys and a conventional magnesium AZ31 alloy. *Acta Materialia*, 57(7):2229 – 2242, 2009.

[113] J.Z. Liu and A. Zunger. Thermodynamic states and phase diagrams for bulk-incoherent, bulk-coherent, and epitaxially-coherent semiconductor alloys: Application to cubic (Ga,In)N. *Physical Review B*, 77:205201, May 2008.

[114] X. Tan, L. Wang, C.M.B. Holt, B. Zahiri, M.H. Eikerling, and D. Mitlin. Body centered cubic magnesium niobium hydride with facile room temperature absorption and four weight percent reversible capacity. *Physical Chemistry Chemical Physics*, 14:10904–10909, 2012.

[115] H. Olijnyk and W.B. Holzapfel. High-pressure structural phase transition in Mg. *Physical Review B*, 31:4682–4683, 1985.

[116] D. Errandonea, R. Boehler, and M. Ross. Melting of the alkaline-earth metals to 80 GPa. *Physical Review B*, 65:012108, 2001.

[117] D. Errandonea, Y. Meng, D. Häusermann, and T. Uchida. Study of the phase transformations and equation of state of magnesium by synchrotron x-ray diffraction. *Journal of Physics: Condensed Matter*, 15(8):1277, 2003.

[118] B. Ham and X. Zhang. High strength Mg/Nb nanolayer composites. *Materials*

Science and Engineering A, 528(4-5):2028–2033, 2011.

[119] B. Ham, A. Junkaew, R. Arróyave, J. Chen, H. Wang, P. Wang, J. Majewski, J. Park, H.-C. Zhou, R.K. Arvapally, U. Kaipa, M.A. Omary, X.Y. Zhang, Y. Ren, and X. Zhang. Hydrogen sorption in orthorhombic Mg hydride at ultra-low temperature. *International Journal of Hydrogen Energy*, 38(20):8328 – 8341, 2013.

[120] A. Junkaew, B. Ham, X. Zhang, A. Talapatra, and R. Arróyave. Stabilization of bcc Mg in Thin Films at Ambient Pressure: Experimental Evidence and *ab initio* Calculations. *Materials Research Letters*, 1:161–167, 2013.

[121] D.M. Wood and A. Zunger. Epitaxial effects on coherent phase diagrams of alloys. *Physical Review B*, 40(6):4062, 1989.

[122] J.Z. Liu and A. Zunger. Thermodynamic states and phase diagrams for bulk-incoherent, bulk-coherent, and epitaxially-coherent semiconductor alloys: Application to cubic (Ga, In)N. *Physical Review B*, 77(20):205201, 2008.

[123] J.Z. Liu and A. Zunger. Thermodynamic theory of epitaxial alloys: first-principles mixed-basis cluster expansion of (In, Ga) N alloy film. *Journal of Physics: Condensed Matter*, 21(29):295402, 2009.

[124] G. Kaptay. Nano-Calphad: extension of the Calphad method to systems with nano-phases and complexions. *Journal of Materials Science*, 47(24):8320–8335, 2012.

[125] R. Banerjee, X.-D. Zhang, S.A. Dregia, and H.L. Fraser. Phase stability in Al/Ti multilayers. *Acta Materialia*, 47(4):1153–1161, 1999.

[126] D.A. Smith and R.C. Pond. Bollmann's O-lattice theory; a geometrical approach to interface structure. *International Materials Reviews*, 21(1):61–74, 1976.

[127] I.A. Kotzé and D. Kuhlmann-Wilsdorf. A theory of the interfacial energy

between a crystal and the melt. *Applied Physics Letters*, 9(2):96–98, 1966.

[128] Q. Jiang and H.M. Lu. Size dependent interface energy and its applications. *Surface Science Reports*, 63(10):427 – 464, 2008.

[129] J.P. Hirth and J. Lothe. *Theory of dislocations*. Wiley, New York, 1982.

[130] A.T. Dinsdale. SGTE data for pure elements. *Chalphad*, 15(4):317–425, 1991.

[131] L. Kaufman and H. Bernstein. *Computer calculation of phase diagram*. Academic Press Inc., New York, 1970.

[132] N. Saunders and A.P. Miodownik. *CALPHAD (Calculation of Phase Diagrams): A comprehensive guide*. New York, Pergamon, Oxford, 1998.

[133] V.M. Goldschmidt. *Berichte der Deutschen Chemischen Gesellschaft*, 60:1270, 1927.

[134] B. M. Caruta. *Focus on nanomaterials research*. Nova Science Publishers, Inc., New York, 2006.

[135] G. Simmons and H. Wang. *Single crystal elastic constants and calculated aggregate properties: a handbook*. M.I.T. Press, Cambridge, 2nd edition edition, 1971.

[136] J.P. Perdew, J.A. Chevary, S.H. Vosko, K.A. Jackson, M.R. Pederson, D.J. Singh, and C. Fiolhais. Atoms, molecules, solids, and surfaces: Applications of the generalized gradient approximation for exchange and correlation. *Physical Review B*, 46:6671–6687, Sep 1992.

[137] G. Kresse and J. Hafner. *Ab initio* molecular dynamics for liquid metals. *Physical Review B*, 47:558–561, 1993.

[138] W. Kraus and G. Nolze. *POWDER CELL* – a program for the representation and manipulation of crystal structures and calculation of the resulting X-ray powder patterns. *Journal of Applied Crystallography*, 29(3):301–303, 1996.

[139] G. Kresse and D. Joubert. From ultrasoft pseudopotentials to the projector

augmented-wave method. *Physical Review B*, 59:1758–1775, Jan 1999.

[140] E. Wachowicz and A. Kiejna. Bulk and surface properties of hexagonal-close-packed Be and Mg. *Journal of Physics: Condensed Matter*, 13(48):10767, 2001.

[141] L.V. Gurvich, I.V. Veyts, and C.B. Alcock. *Thermodynamic properties of individual substances*. Begell House, New York, 1996.

[142] A.W. Hull. A new method of x-ray crystal analysis. *Physical Review*, 10:661–696, 1917.

[143] Y. Wang, S. Curtarolo, C. Jiang, R. Arróyave, T. Wang, G. Ceder, L.-Q. Chen, and Z.-K. Liu. Ab initio lattice stability in comparison with CALPHAD lattice stability. *Calphad*, 28(1):79 – 90, 2004.

[144] W.F. Gale and T.C. Totemeier. *Smithells metals reference book*. Elsevier/Butterworth-Heinemann, Amsterdam, 8th ed./edited by W.F. Gale, T.C. Totemeier. edition, 2004.

[145] S. Mehta, G.D. Price, and D. Alfè. Ab initio thermodynamics and phase diagram of solid magnesium: A comparison of the LDA and GGA. *Journal of Chemical Physics*, 125(19):194507, 2006.

[146] K. Persson, M. Ekman, and Vidvuds Ozoliņš. Phonon instabilities in bcc Sc, Ti, La, and Hf. *Physical Review B*, 61:11221–11224, May 2000.

[147] W. Luo, B. Johansson, O. Eriksson, S. Arapan, P. Souvatzis, M.I. Katsnelson, and R. Ahuja. Dynamical stability of body center cubic iron at the earths core conditions. *Proceedings of the National Academy of Sciences*, 107(22):9962–9964, 2010.

[148] M. Born. On the stability of crystal lattices. I. *Math Proc Cambridge*, 36:160 – 172, 1940.

[149] J. Wang, J. Li, S. Yip, S. Phillpot, and D. Wolf. Mechanical instabilities of homogeneous crystals. *Physical Review B*, 52:12627–12635, Nov 1995.

[150] O.H. Nielsen and R.M. Martin. First-principles calculation of stress. *Physical Review Letters*, 50:697–700, Feb 1983.

[151] L.J. Slutsky and C.W. Garland. Elastic constants of magnesium from 4.2°K to 300°K. *Physical Review*, 107:972–976, Aug 1957.

[152] N. Novaković, L. Matović, J.G. Novaković, M. Manasijević, and N. Ivanović. Ab initio study of MgH_2 formation. *Materials Science and Engineering B*, 165(3):235 – 238, 2009.

[153] K. Chen and K. Boyle. Elastic properties, thermal expansion coefficients, and electronic structures of Mg and Mg-based alloys. *Metallurgical and Materials Transactions A*, 40:2751–2760, 2009.

[154] J.A. Moriarty and A.K. McMahan. High-pressure structural phase transitions in Na, Mg, and Al. *Physical Review Letters*, 48:809–812, 1982.

[155] W.G. Burgers. On the process of transition of the cubic-body-centered modification into the hexagonal-close-packed modification of zirconium. *Physica*, 1(7-12):561 – 586, 1934.

[156] Y. Chen, K.M. Ho, and B.N. Harmon. First-principles study of the pressure-induced bcc-hcp transition in Ba. *Physical Review B*, 37:283–288, 1988.

[157] S.R. Nishitani, H. Kawabe, and M. Aoki. First-principles calculations on bc-chcp transition of titanium. *Materials Science and Engineering A*, 312(1-2):77 – 83, 2001.

[158] K.J. Caspersen, A. Lew, M. Ortiz, and E.A. Carter. Importance of shear in the bcc-to-hcp transformation in Iron. *Physical Review Letters*, 93:115501, 2004.

[159] E. Weinan, W. Ren, and E. Vanden-Eijnden. Simplified and improved string method for computing the minimum energy paths in barrier-crossing events. *Journal of Chemical Physics*, 126:164103, 2007.

[160] W. E, W. Ren, and E. Vanden-Eijnden. String method for the study of rare

events. *Physical Review B*, 66:052301, 2002.

[161] D.F. Johnson, D.E. Jiang, and E.A. Carter. Structure, magnetism, and adhesion at Cr/Fe interfaces from density functional theory. *Surface Science*, 601(3):699 – 705, 2007.

[162] H.R. Gong, Y. Nishi, and K. Cho. Effects of strain and interface on work function of a Nb–W metal gate system. *Applied Physics Letters*, 91(24):242105, 2007.

[163] W. Liu, J.C. Li, W. . Zheng, and Q. Jiang. NiAl(110)/Cr(110) interface: A density functional theory study. *Physical Review B*, 73:205421, May 2006.

[164] A. Arya and E.A. Carter. Structure, bonding, and adhesion at the ZrC (1 0 0)/Fe(1 1 0) interface from first principles. *Surface Science*, 560:103–120, 2004.

[165] B.D. Yu and J.-S. Kim. *Ab initio* study of ultrathin MgO films on Fe(001): influence of interfacial structures. *Physical Review B*, 73:125408, Mar 2006.

[166] J.P. Perdew, K. Burke, and M. Ernzerhof. Generalized gradient approximation made simple. *Physical Review Letters*, 77:3865–3868, Oct 1996.

[167] K. Momma and F. Izumi. *VESTA*: a three-dimensional visualization system for electronic and structural analysis. *Journal of Applied Crystallography*, 41(3):653–658, Jun 2008.

[168] J.L. Han, L.Z. Sun, X.D. Qu, Y.P. Chen, and J.X. Zhong. Electronic properties of the Au impurity in Hg0.75Cd0.25Te: First-principles study. *Physica B*, 404(1):131 – 137, 2009.

[169] M. Kohout, F.R. Wagner, and Y. Grin. Electron localization function for transition-metal compounds. *Theoretical Chemistry Accounts*, 108:150–156, 2002.

[170] A.K. McMahan and John A. Moriarty. Structural phase stability in third-period simple metals. *Physical Review B*, 27:3235–3251, Mar 1983.

[171] A.R. Jani, N.E. Brener, and J. Callaway. Band structure and related properties of bcc niobium. *Physical Review B*, 38:9425–9433, Nov 1988.

[172] H. van Leuken, A. Lodder, and R.A. de Groot. Ab initio electron-structure calculations on the Nb/Ta multilayer system. *Journal of Physics: Condensed Matter*, 3(22):3945, 1991.

[173] K. Shein, I. Shein, N. Medvedeva, E. Shalaeva, M. Kuznetsov, and A. Ivanovskii. Effects of atomic relaxation and the electronic structure of niobium (100) and (110) surfaces. *Physics of Metals and Metallography*, 102(6):604–610, 2006.

[174] H.R. Gong and K. Cho. First principles study of Nb-W bilayer metal gate electrode. *Microelectronic Engineering*, 86(3):240 – 243, 2009.

[175] B.-Q. Fu, W. Liu, and Z.-L. Li. Calculation of the surface energy of bcc-metals with the empirical electron theory. *Applied Surface Science*, 255(20):8511 – 8519, 2009.

[176] M. Methfessel, D. Hennig, and M. Scheffler. Trends of the surface relaxations, surface energies, and work functions of the $4d$ transition metals. *Physical Review B*, 46:4816–4829, Aug 1992.

[177] M. Weinert, R.E. Watson, J.W. Davenport, and G.W. Fernando. Adsorbed layer and multilayer materials: The energetics and bonding of Pd and Ag on Nb(001) and Nb(110). *Physical Review B*, 39:12585–12597, Jun 1989.

[178] L. Vitos, A.V. Ruban, H.L. Skriver, and J. Kollár. The surface energy of metals. *Surface Science*, 411(1-2):186 – 202, 1998.

[179] J.-M. Zhang, D.-D. Wang, and K.-W. Xu. Calculation of the surface energy of bcc transition metals by using the second nearest-neighbor modified embedded atom method. *Applied Surface Science*, 252(23):8217 – 8222, 2006.

[180] W.R. Tyson and W.A. Miller. Surface free energies of solid metals: Estimation

from liquid surface tension measurements. *Surface Science*, 62(1):267–276, 1977.

[181] P.T. Sprunger, K. Pohl, H.L. Davis, and E.W. Plummer. Multilayer relaxation of the Mg(0001) surface. *Surface Science*, 297(1):L48 – L54, 1993.

[182] H.P. Ismail, A.P. Baddorf, and E.W. Plummer. Thermal expansion at a metal surface: A study of Mg(0001) and Be($10\bar{1}0$). $PhysicalReviewB, 66 : 245414, Dec2002$.

[183] J.L.F. Da Silva, C. Stampfl, and M. Scheffler. Converged properties of clean metal surfaces by all-electron first-principles calculations. *Surface Science*, 600(3):703 – 715, 2006.

[184] J.S. Luo and B. Legrand. Multilayer relaxation at surfaces of body-centered-cubic transition metals. *Physical Review B*, 38:1728–1733, Jul 1988.

[185] R.M. Wentzcovitch and M.L. Cohen. Theoretical model for the hcp-bcc transition in Mg. *Physical Review B*, 37:5571–5576, Apr 1988.

[186] A.F. Wright, P.J. Feibelman, and S.R. Atlas. First-principles calculation of the Mg(0001) surface relaxation. *Surface Science*, 302(1-2):215 – 222, 1994.

[187] P. Staikov and T.S. Rahman. Multilayer relaxations and stresses on Mg surfaces. *Physical Review B*, 60:15613–15616, Dec 1999.

[188] X.-G. Li, P. Zhang, and C.K. Chan. First-principles calculation of Mg(0001) thin films: Quantum size effect and adsorption of atomic hydrogen. *Physica B*, 390(1-2):225 – 230, 2007.

[189] W.K. Liu and M.B. Santos. *Thin Films: Heteroepitaxial Systems*. Series on Directions in Condensed Matter Physics, Vol 15. World Scientific Publ., Singapore ; River Edge, NJ, 1999.

[190] C.L. Fu, S. Ohnishi, E. Wimmer, and A.J. Freeman. Energetics of surface multilayer relaxation on W(001): Evidence for short-range screening. *Physical*

Review Letters, 53:675–678, Aug 1984.

[191] B. Bogdanović, K. Bohmhammel, B. Christ, A. Reiser, K. Schlichte, R. Vehlen, and U. Wolf. Thermodynamic investigation of the magnesiumhydrogen system. *Journal of Alloys and Compounds*, 282(12):84 – 92, 1999.

[192] J.A. Kennelley, J.W. Varwig, and H.W. Myers. Magnesium-hydrogen relationships. *Journal of Physical Chemistry*, 64(5):703–704, 1960.

[193] W. Klose and V. Stuke. Investigation of the thermodynamic equilibrium in the hydrogen-magnesium-magnesium hydride system. *International Journal of Hydrogen Energy*, 20(4):309 – 316, 1995.

[194] J.F. Stampfer Jr., C.E. Holley Jr., and J.F. Suttle. The magnesium-hydrogen system. *Journal of the American Chemical Society*, 82(14):3504–3508, 1960.

[195] P. Vajeeston, P. Ravindran, A. Kjekshus, and H. Fjellvåg. Pressure-induced structural transitions in mgh_2. *Physical Review Letter*, 89:175506, Oct 2002.

[196] T. Schober. The niobium-hydrogen system–an electron microscope study. I. Room temperature results. *physica status solidi (a)*, 29(2):395–406, 1975.

[197] H. Peisl. *Topics in Applied Physics: Hydrogen in Metals I.* Springer Berlin Heidelberg, New York, 1978.

[198] H. Fujii, K. Higuchi, K. Yamamoto, H. Kajioka, S. Orimo, and K. Toiyama. Remarkable hydrogen storage, structural and optical properties in multi-layered Pd/Mg thin films. *Materials Transactions*, 43(11):2721–2727, 2002.

[199] Structure modification of MgNb films under hydrogen sorption cycles. *Journal of Alloys and Compounds*, 509, Supplement 2(0):S572 – S575, 2011.

[200] L. Schlapbach. *Hydrogen in intermetallic compounds-I.* Springer-Verlag, New York, 1988.

[201] A. Baldi, M. Gonzalez-Silveira, V. Palmisano, B. Dam, and R. Griessen. Destabilization of the mg-h system through elastic constraints. *Physical Review*

Letters, 102:226102, Jun 2009.

[202] H. Wipf. *Topics in Applied Physics: Hydrogen in Metall III properties and applications*. Springer, New York, 1997.

[203] J.P. Watt. Hashin-shtrikman bounds on the effective elastic moduli of polycrystals with orthorhombic symmetry. *Journal of Applied Physics*, 50(10):6290–6295, 1979.

[204] J.P. Watt and L. Peselnick. Clarification of the hashin-shtrikman bounds on the effective elastic moduli of polycrystals with hexagonal, trigonal, and tetragonal symmetries. *Journal of Applied Physics*, 51(3):1525–1531, 1980.

[205] Y. Wang, Z.-K. Liu, and L.-Q. Chen. Thermodynamic properties of Al, Ni, NiAl, and Ni_3Al from rst-principles calculations. *Acta Materialia*, 52:2665–2671, 2004.

[206] R. Arróyave and Z.-K. Liu. Intermetallics in the Mg-Ca-Sn ternary system: Structural, vibrational, and thermodynamic properties from first principles. *Physical Review B*, 74(17):174118, 2006.

[207] A. van de Walle and G. Ceder. The effect of lattice vibrations on substitutional alloy thermodynamics. *Review of Modern Physics*, 74:11–45, Jan 2002.

[208] D.C. Wallace. *Thermodynamics of Crystals*. Willey, New York, 1972.

[209] A.R. Oganov and P.I. Dorogokupets. Intrinsic anharmonicity in equations of state and thermodynamics of solids. *Journal of Physics: Condensed Matter*, 16(8):1351, 2004.

[210] J. Paier, R. Hirschl, M. Marsman, and G. Kresse. The Perdew–Burke–Ernzerhof exchange-correlation functional applied to the G2-1 test set using a plane-wave basis set. *The Journal of Chemical Physics*, 122(23):234102, 2005.

[211] M. Asta A. van de Walle and G. Ceder. The alloy theoretic automated toolkit: A user guide. *Calphad*, 26(4):539–553, 2002.

[212] V.A. Somenkov, A.V. Gurskaya, M.G. Zemlyanov, M.E. Kost, N.A. Chernoplekov, and A.A. Chertkov. Neutron scattering study of structure and phase transitions in niobium hydrides and deuterides. *Soviet Physics Solid State*, 10:1355, 1968.

[213] F.H. Ellinger, C.E. Holley, Jr. B.B. McInteer, D. Pavone, R.M. Potter, E. Staritzky, and W.H. Zachariasen. The preparation and some properties of magnesium hydride. *Journal of the American Chemical Society*, 77:2647, 1955.

[214] K.J. Carroll. Elastic constants of Niobium from 4.2^o to 300^oK. *Journal of Applied Physics*, 36(11):3689–3690, 1965.

[215] D.I. Bolef. Elastic constants of single crystals of the bcc transition elements V, Nb, and Ta. *Journal of Applied Physics*, 32(1):100–105, 1961.

[216] H.A. Rafizadeh. Lattice dynamics of metal hydrides. *Physical Review B*, 23:1628–1632, Feb 1981.

[217] A. Fabre, E. Finot, J. Demoment, and S. Contreras. In situ measurement of elastic properties of PdH_x , PdD_x , and PdT_x. *Journal of Alloys and Compounds*, 356357:372–376, 2003.

[218] T. Lyman. *Metals Handbook*, volume 1. American Society for Metals, Melno Park, Ohio, 8th edition, 1961.

[219] L.G. Hector, J.F. Herbst, W. Wolf, P. Saxe, and G. Kresse. *Ab Initio* thermodynamic and elastic properties of alkaline-earth metals and their hydrides. *Physical Review B*, 76:014121, Jul 2007.

[220] G.L. Holleck. Diffusion and solubility of hydrogen in palladium and palladium–silver alloys. *The Journal of Physical Chemistry*, 74(3):503–511, 1970.

[221] J. Völkl and H. Wipf. *'Diffusion of hydrogen in metals' in Hydrogen in Metals I.* Springer Berlin Heidelberg, New York, 1978.

[222] D.E. Jiang and E.A. Carter. Diffusion of interstitial hydrogen into and through

bcc Fe from first principles. *Physical Review B*, 70:064102, Aug 2004.

[223] D.S. Sholl. Using density functional theory to study hydrogen diffusion in metals: A brief overview. *Journal of Alloys and Compounds*, 446447(0):462 – 468, 2007.

[224] C. Duan, Y.-L. Liu, H.-B. Zhou, Y.Z., S. Jin, G.-H. Lu, and G.-N. Luo. First-principles study on dissolution and diffusion properties of hydrogen in molybdenum. *Journal of Nuclear Materials*, 404(2):109 – 115, 2010.

[225] D.M. Bird, L.J. Clarke, M.C. Payne, and I. Stich. Dissociation of h_2 on Mg(0001). *Chemical Physics Letters*, 212(5):518–524, 1993.

[226] J.K. Nørskov, A. Houmøller, P.K. Johansson, and B.I. Lundqvist. Adsorption and dissociation of H_2 on Mg surfaces. *Physical Review Letters*, 46(4):257–260, 1981.

[227] P.T. Sprunger and E.W. Plummer. The interaction of hydrogen with simple metal surfaces. *Surface Science*, 307309, Part A(0):118 – 123, 1994.

[228] G. Henkelman, G. Jóhannesson, and H. Jónsson. *'Methods for finding saddle points and minimum energy paths' in Theoretical Methods in Condensed Phase Chemistry edited by S.D. Schwartz.* Kluwer Academic Publishers, Netherlands, 2002.

[229] H. Jónsson, G. Mills, and K. W. Jacobsen. *'Nudged Elastic Band Method for Finding Minimum Energy Paths of Transitions', in 'Classical and Quantum Dynamics in Condensed Phase Simulations' edited by B.J. Berne, G. Ciccotti and D.F. Coker.* World Scientific, Singapore, 1980.

[230] G. Mills, H. Jónsson, and G.K. Schenter. Reversible work transition state theory: application to dissociative adsorption of hydrogen. *Surface Science*, 324(23):305–337, 1995.

[231] G. Henkelman, B.P. Uberuaga, and H. Jonsson. A climbing image nudged

elastic band method for finding saddle points and minimum energy paths. *The Journal of Chemical Physics*, 113(22):9901–9904, 2000.

[232] S. Aboud and J. Wilcox. A density functional theory study of the charge state of hydrogen in metal hydrides. *The Journal of Physical Chemistry C*, 114(24):10978–10985, 2010.

APPENDIX A

1. Gibbs free energy from Calphad method [130]

Table A.1: The equations of Gibbs energies (G) at temperature (T) of each phase of Mg and Nb

Structure	G
hcp Mg (298.15K $<T<$923.00K)	-8367.34 + 143.675547T - 26.1849782 $Tln(T)$ + 0.4858E-3 T^2 - 1.393669E-6 T^3 + 78950 T^{-1}
bcc Mg (298.15K $<T<$923.00K)	-5267.34+141.575547 T - 26.1849782$Tln(T)$ + 0.4858E-3 T^2 - 1.393669E-6 T^3 + 78950 T^{-1}
bcc Nb (298.15K $<T<$2750.00K)	-8519.353+142.045475 T - 26.4711 $Tln(T)$ + 0.203475E-3 T^2 - 0.350119E-6 T^3 + 93399 T^{-1}
hcp Nb (298.15K $<T<$2750.00K)	-1480.647 + 144.445475 T - 26.4711 $Tln(T)$ + 0.203475E-3 T^2 - 0.350119E-6 T^3 + 93399 T^{-1}

2. Slopes (m) and constant (c) of three boundaries of bi-phase diagram shown in Fig. 3.2

From Eq. 3.3, it can be rewritten as the following equation:

$$0 = 2\Delta\gamma + [\Delta G_{Mg}(1 - f_{Nb}) + \Delta G_{Nb} f_{Nb}]\lambda \tag{A.1}$$

2.1 Equation of line 1: hcp Mg/bcc Nb $\rightarrow$ bcc Mg/bcc Nb transformation (ΔG_{Nb}=0)

$$\frac{1}{\lambda} = -\frac{\Delta G_{Mg}}{2\Delta\gamma_1}(1 - f_{Nb}) = -\frac{G^{bcc}_{Mg} - G^{hcp}_{Mg}}{2(\gamma_{bcc/bcc} - \gamma_{hcp/bcc})}(1 - f_{Nb}) \tag{A.2}$$

2.2 Equation of line 2: hcp Mg/hcp Nb $\rightarrow$ bcc Mg/bcc Nb transformation

$$\frac{1}{\lambda} = -\frac{\Delta G_{Mg}}{2\Delta\gamma_2} - \frac{(\Delta G_{Nb} - \Delta G_{Mg})}{2\Delta\gamma_2} f_{Nb} \tag{A.3}$$

where $\Delta G_{Mg} = G^{bcc}_{Mg} - G^{hcp}_{Mg}$, $\Delta G_{Nb} = G^{bcc}_{Nb} - G^{hcp}_{Nb}$, and $\Delta\gamma_2 = \gamma_{bcc/bcc} - \gamma_{hcp/hcp}$.

2.3 Equation of line 3: hcp Mg/bcc Nb $\rightarrow$ hcp Mg/hcp Nb transformation (ΔG_{Mg}=0)

$$\frac{1}{\lambda} = -\frac{\Delta G_{Nb}}{2\Delta\gamma_3} f_{Nb} = -\frac{(G^{hcp}_{Nb} - G^{bcc}_{Nb})}{2(\gamma_{hcp/hcp} - \gamma_{hcp/bcc})} f_{Nb} \tag{A.4}$$

From those three equations, the data set of bi-phase diagram of Mg/Nb multilayers can be evaluated from $1/\lambda = m f_{Nb} + c$. Calculated m and c values are given in Table A.2.

Table A.2: Calculated slopes (m) and constants (c) of three boundaries

Line	m (nm^{-1})	c (nm^{-1})
1	-0.3397	0.3397
2	-557.4600	84.6034
3	1.9060	0.0000